PÁZMÁNY PÉTER CATHOLIC UNIVERSITY

ROSKA TAMÁS DOCTORAL SCHOOL OF SCIENCES AND TECHNOLOGY

Structural and functional investigation of non-globular regions in the postsynaptic Drebrin protein

PhD Dissertation

Soma Varga

Supervisor:Bálint Ferenc Péterfia, PhD

Budapest • 2025

„Be curious, not judgmental”

Walt Whitman

Table of contents

Abbreviations

ABD	Actin-Binding Domain
ADFH	Actin Depolymerizing Factor Homology
ATP	Adenosine Triphosphate
BMRB	Biological Magnetic Resonance Data Bank
BPTI	Bovine Pancreatic Trypsin Inhibitor
BSA	Bovine Serum Albumin
CD	Circular Dichroism
CEST	Chemical Exchange Saturation Transfer
CPMG	Carr–Purcell–Meiboom–Gill
CSP	Chemical Shift Perturbation
DSS	2,2-Dimethyl-2-silapentane-5-sulfonate
ECD	Electronic Circular Dichroism
EVH1	Ena/VASP Homology 1 Domain
HBM	Homer-Binding Motif
HSQC	Heteronuclear Single Quantum Coherence
IDP	Intrinsically Disordered Protein
IEC	Ion Exchange Chromatography
IMAC	Immobilized Metal Affinity Chromatography
IPTG	Isopropyl β-D-1-thiogalactopyranoside
MALLS	Multi-Angle Laser Light Scattering
MD	Molecular Dynamics
MFU	McFarland Unit
MS	Mass Spectrometry
MW	Molecular Weight
MWCO	Molecular Weight Cut-Off
NMR	Nuclear Magnetic Resonance
NOE	Nuclear Overhauser Effect
NPT	Constant Number of Particles, Pressure, and Temperature
NVT	Constant Number of Particles, Volume, and Temperature

PCA	Principal Component Analysis
PDB	Protein Data Bank
PED	Protein Ensemble Database
PRE	Paramagnetic Relaxation Enhancement
PSD	Postsynaptic Density
Q-TOF	Quadrupole Time-of-Flight
RCCS	Random Coil Chemical Shift
RI	Refractive Index
SAH	Single Alpha-Helix
SAXS	Small-Angle X-ray Scattering
SDS-PAGE	Sodium Dodecyl Sulfate–Polyacrylamide Gel Electrophoresis
SEC	Size-Exclusion Chromatography
TCEP	Tris(2-carboxyethyl)phosphine
TEV	Tobacco Etch Virus
TROSY	Transverse Relaxation Optimized Spectroscopy

List of figures

1. Introduction

During my PhD work, I participated in a comprehensive research project aimed at better understanding the neuronal Drebrin (Developmentally Regulated Brain Protein) protein, which had remained largely uncharacterized until recently. To achieve this, I got acquainted with various molecular biology techniques and gained first-hand experience in obtaining atomic-level structural and functional information from a protein previously unstudied in our laboratory.

From the outset of my PhD, I had the opportunity to independently decide which protein segments to investigate. This allowed me to initiate my project with designing constructs, including primer design and molecular cloning. Once the required plasmid DNAs were prepared, I focused on optimizing protein expression and purification protocols. Since non-globular proteins had been limitedly studied in our research group before, I had the unique opportunity to develop and establish new methods for producing high-quality samples.

The core of my PhD research consisted of NMR spectroscopy. I successfully completed my first two resonance assignments on challenging protein segments that had not been previously characterized. These successes demonstrate how carefully selected NMR techniques can provide solutions to complex problems. In addition, I performed SAXS experiments on one of my target proteins, which not only yielded structural insights previously inaccessible, but also broadened my understanding of complementary biophysical methods.

With high-quality experimental data in hand, I further deepened my knowledge in bioinformatics. I employed molecular dynamics simulations to support data-driven structural modeling, showcasing once again the effectiveness of integrating multiple techniques.

Reflecting on the past four years, I set out with a single goal: to become a versatile scientist capable of formulating biologically relevant questions and selecting the appropriate tools to answer them in detail. Given the diverse methods I employed, and my involvement in all stages of the research — from conceptualization through execution to interpretation and communication — I am confident that I have achieved this goal.

2. Literature overview

2.1 The postsynaptic density

The synapsis is a close connection between two nerve cells, or as written by Sherrington already in the 19th century in „A textbook of physiology", simply a contact without the continuity of substance (1). Subsequently, in the 20th century, synapses were described as polarized neuronal cell junctions with a distinguished transmitter-releasing presynaptic, and an accepting postsynaptic part (2). The PSD (Postsynaptic Density) is a dense and complex network of proteins with a great variety of their biological roles and structural attributes. Members of this huge macromolecular signaling complex can be classified as cell-adhesion proteins, cytoskeletal proteins, scaffolding and adaptor proteins, membrane-bound receptors and channels, G-proteins and modulators and signaling molecules including kinases/phosphatases (3–7). Overexpression or underexpression of these proteins, and other deviations such as mutations are often reporters of neuronal diseases such as Alzheimer's disease, Aging, Autism spectrum disorder, Dementia, Asperger syndrome, Schizophrenia and many other mental disorders (8–10). Even though there is an emerging number of studies identifying these symptoms in patients, the exact molecular understanding of the functional divergence caused by structural alterations is yet to be revealed in many cases. To decipher these connections and comprehend their consequences, we have to keep in mind the complexity of PSD, and that each novel result derived from years of work can be only considered one piece of the large macromolecular puzzle (Figure 1).

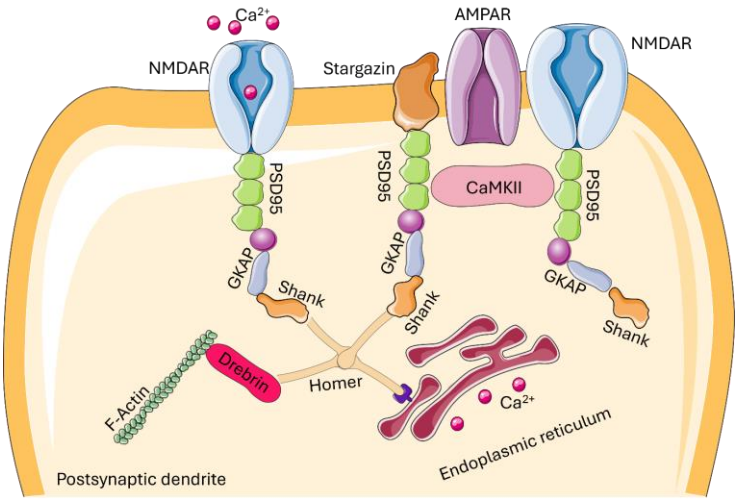

Figure 1: Drebrin interactions in the context of several major postsynaptic proteins. Drebrin is believed to play a key role in anchoring the postsynaptic protein network to the actin cytoskeleton. Figure is taken from (11).

2.1.1. The role of Drebrin in the PSD

Drebrin is an actin cytoskeleton-organizing protein (12) that is crucial for dendritic spine morphogenesis and organization (13). Previous studies have described its actin-bundling (14), actin-binding (15) and actin-depolymerizing (16) properties, showcasing its complex role in the organization of postsynaptic density (PSD). Drebrin can only interact with filamentous (F) actin and not with the monomeric (G) form (17). Drebrin binding to F-actin causes structural changes in the F-actin filament, slows down the treadmilling rate and influences the activity of motor proteins such as myosin II on F-actin. A model of the role of Drebrin in the response of dendritic spines to synaptic activity has been described in detail (18). In this, Drebrin's role is to form a pool of stable actin filaments that help stabilize dendritic spine sizes via a dynamic equilibrium between the Drebrin-bound and unbound filaments. Upon Ca2+-influx caused by synaptic activation, Drebrin and the bound actin filaments exit the synaptic spine, a process termed Drebrin exodus. This, in turn, allows G-actin to fill the spine and polymerize, contributing to spine size enlargement. At the end of the stimulus, Drebrin re-enters the spine and re-establishes the pool of stable actin filaments, stabilizing the enlargement by restoring the equilibrium between different actin forms.

Decrease in the availability of Drebrin has been linked to various neurological conditions, primarily Alzheimer's disease (AD), but also to Down syndrome and ageing. The above described model is consistent with the role of Drebrin in maintaining synaptic plasticity and the decline of cognitive functions under certain conditions.

Drebrin has two main isoforms, Drebrin E and Drebrin A, the latter containing an isoform-specific insertion, but both share the same actin-binding sequences (19). Drebrin has been shown to alter the helical pitch of actin, possibly contributing to the altered dynamics of actin assembly resulting in the slower treadmilling rate. The actin-binding activity of Drebrin has been established to be localized in its N-terminal region, and the role of the segment 233-317 has been emphasized. Drebrin contains a number of unique non-globular structural motifs and to date, there is no consensus on the overall structural organization of the protein and the biological role of its different segments (Figure 2).

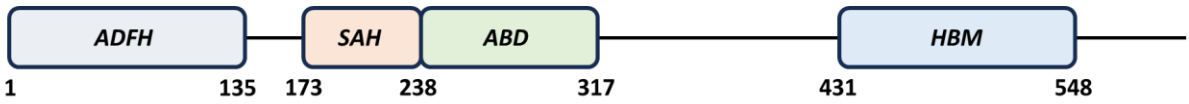

Figure 2: Domain organization of Drebrin.
ADFH: Actin-Depolymerizing Factor Homology, SAH: Single Alpha-Helix, ABD: Actin-Binding Domain, HBM: Homer-Binding Motifs. Sequence positions in Drebrin harboring the domains are shown with amino acid numbers of the full length protein.

2.1.2. The role of ADFH domain in Drebrin

Actin-Depolymerizing Factor Homology (ADFH) domains are conserved elements with well-understood globular structures, identified in 39 proteins by Lappalainen and colleagues (17). This high level of structural and sequential analogy is a common indicator of similar function and biological role. However, even minor alterations such as a couple of point mutations can lead to functional loss, but also new functionalities can arise this way. In the case of Drebrin-ADFH, the strong actin-binding and actin-depolymerizing properties, most commonly associated with ADFH domains have been disappeared (20). On the contrary, Yao and colleagues came up with the suggestion of this domain being responsible for a cytoplasmic sequestering mechanism of ZMYND8 histone marker reader (21). In their work, they compared the amino acid sequences of αC helix segments in several ADFH domains from human proteins and concluded that residues crucial for actin-binding are missing. The four key residues identified were the hydrophobic amino acids at position 1, the methionine at position 5 and two positively-charged amino acids at positions 2 and 11 (Figure 3). Compared to its orthologs, Drebrin-ADFH is different in all these sequential positions, and it turned out that cysteine at position 5 not just prevents binding to F-actin but also plays key role in the binding of ZMYND8. This was an important recognition which also raised further questions about how Drebrin can bind to the actin filaments, if not through its ADFH domain.

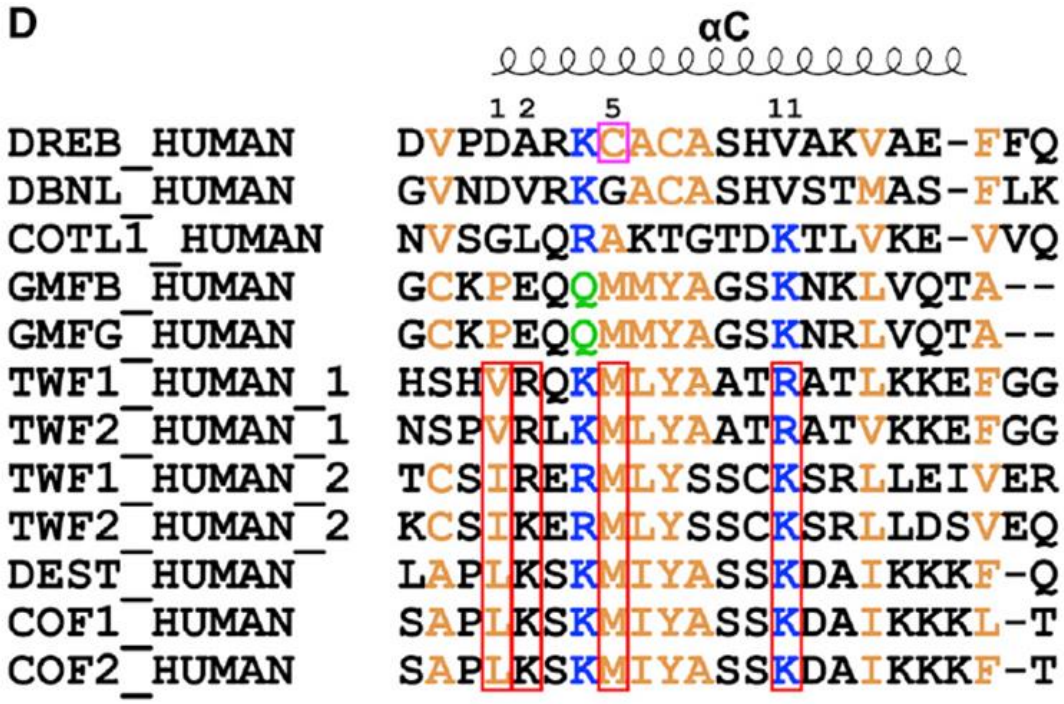

Figure 3: Sequential alignment of the αC helix in several ADFH domains from human proteins. Crucial residues for actin-binding are highlighted in red frame. Figure is taken from (21).

2.1.3. The intrinsically disordered Actin-binding core in Drebrin

The observation that Drebrin contains an ADFH domain, which does not appear to be its primary actin-binding site prompted researchers to investigate other truncated segments of the protein to attempt to determine the region responsible for the binding. The Actin-Binding Domain (ABD) of Drebrin has been first delineated in several in vivo studies (15,22,23), then it has been further investigated via low-resolution analytical methods such as cosedimentation assays (Figure 4). Results from these studies do not concur and suggest the location of Drebrin ABD in different sequential positions, including the primary binding site between residues 233-300 or 233-317, with K_D values between 6.2 and 8.2 μM (24). Worth et al. further suggested the possibility of cooperative binding involving N-terminal parts of Drebrin as well (25). Secondary structure analysis from circular dichroism data by Grintsevich et al. suggests the ABD to be highly disordered.

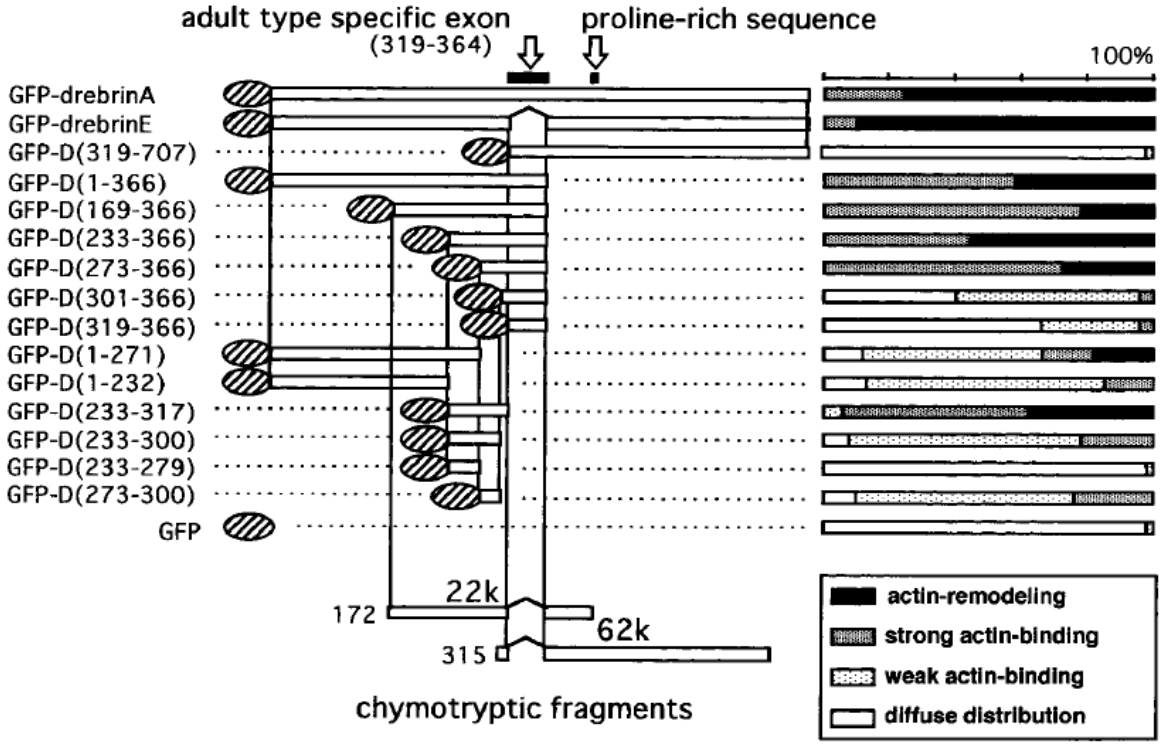

Figure 4: Schematic representation of truncated GFP fusion Drebrin constructs and their actin-binding and actin-remodeling activities.
The amino acid residues of Drebrin are shown in parentheses. Note that the central 85-amino-acidsequence, namely, GFP-D (233–317), exhibited strong actin-binding activity and actin-remodeling activity. Chymotryptic fragments that bound to F-actin (22 kDa) or did not (62 kDa) are also shown at the bottom. Figure is taken from (15).

To conclude the information available in literature, it can be declared that there is a primary actin-binding site in Drebrin between amino acids 233-317, which is highly flexible. The *in vivo* studies confirm

the binding, however, do not shed light on exact molecular mechanisms on atomic level. The accuracy of stochiometric parameters such as equilibrium dissociation constant (K_D) derived by low-resolution methods should be considered carefully, as other biophysical techniques have been proved to be more reliable to this application (26). It has been proved that the ADFH domain in Drebrin can not individually bind F-actin, although considering its evolutional development, it can not be excluded, that it contributes to the actin-binding in other ways. The fact that full length Drebrin protein proved to have higher affinity to actin filaments then the isolated ABD domain raises the idea of a more complex binding mechanism with potential secondary binding site(s) in the N-terminal region of Drebrin.

2.1.4. The Single Alpha-Helix in Drebrin

Single alpha-helical (SAH) domains form stable helices in solution and are proposed to possess unique mechanical properties like acting as constant force springs, lever arms and spacers between protein regions with different functions. The first SAH domains were found in Caldesmon (27) and in Myosin 10 (28), prompting the introduction of the term SAH itself. To date, very few atomic-level structural studies are available on SAH domains, and most of these focus on the SAH in myosin VI, one of the first SAH regions discovered. Structures available in the PDB (Protein Data Bank) include the X-ray structure of myosin VIIa (5WST (29)) SAH and the recently described DNA-binding 'KER' region of the chromatin assembly factor Cac1 (8DEI (30)), as well as the solution NMR structure of the myosin VI SAH (6OBI (31)). All three are straight helical structures with no direct representation of the actual dynamic internal motions characteristic to SAH regions.

In contrast, a number of dynamic features have been proposed to contribute to SAH stability and its mechanical properties, including the constant reorganization of ionic interactions (32). Using the NMR chemical shift and residual dipolar coupling data available from myosin VI, my colleagues have previously generated a structural ensemble to explore the nature and extent of the internal motions in the myosin VI SAH region, as part of the demonstration of the ensemble-generation pipeline DIPEND (33), developed in our research group. This ensemble suggests the presence of kinking motions with largely retained overall helicity. The exact extent of helix breaks has been proposed to represent a major difference between SAHs and less stable helical peptides, with SAHs exhibiting generally more stable straight conformations with higher end-to-end distances (34,35).

Drebrin contains a number of unique non-globular structural motifs and to date, there is no consensus on the overall structural organization of the protein and the biological role of its different segments. A primary example is the region between residues 173-238, initially predicted to form a coiled coil (25), then

recognized as a likely Single Alpha Helix (SAH) (Figure 5) (36,37), more consistent with the observed monomeric nature of the protein (14).

Q16643 (DBN1)	173.238	KRINREQFWEQAKKEEELRKEEERKKALDERLRFEQERMEQERQEQEERERRYRE REQQIEEHRRK

$$R(n) = \sum_{i=1}^{m-n} c(i)c(i+n)$$

n: the sequential distance
m: the length of the sequence
c: the charge assigned to the ith residue of the sequence

Figure 5: The predicted SAH sequence in the Drebrin protein by CSAH server.
Positively charged residues are highlighted with blue and negatively charged residues with red. The formula defining the charge correlation function R is described below. Figure is taken from (36).

The putative SAH region of Drebrin is practically fully conserved in a number of orthologs (Table A6), and Drebrin exhibits several characteristic differences relative to the most well-studied myosin SAHs, most notably the presence of a neighboring Phe-Trp residue pair near its N-terminus, a Phe in the central as well as Tyr and a His in the C-terminal region of the SAH. The myosin VI SAH contains no aromatic residues, whereas the myosin VIIa SAH construct has a single Tyr in the N-terminal and two His residues in the central region and near the C-terminus. In addition, the distribution of Arg and Lys residues is characteristically different. The Drebrin-SAH exhibits a biased distribution with practically no lysines in its C-terminal half except the last residue of the predicted region, again in contrast with the myosin SAHs where no such marked bias can be observed, although the N-terminal segment of the myosin VIIa SAH (32), bearing the Tyr residue, is also devoid of Lys residues (Figure 6). It has been proposed that the Lys and Arg amino acids have slightly different contributions to SAH helicity and stability (38), thus, sequence variation in different natural SAH regions might contribute to their biological versatility.

From the few published works on SAH motifs, it is apparent that the functional role of these unique rod-like protein segments is associated with their remarkable stability. In the SAH examples from myosins, their mechanical properties are exploited as they behave as lever arms. Interestingly, SAH domains are often predicted to be located in between two functionally distinct domains. Hence this is exactly the situation in Drebrin as well, it is tempting to hypothesize that the SAH domain acts as a spacer between the ADFH and ABD domains, to provide their proper distance and spatial orientation.

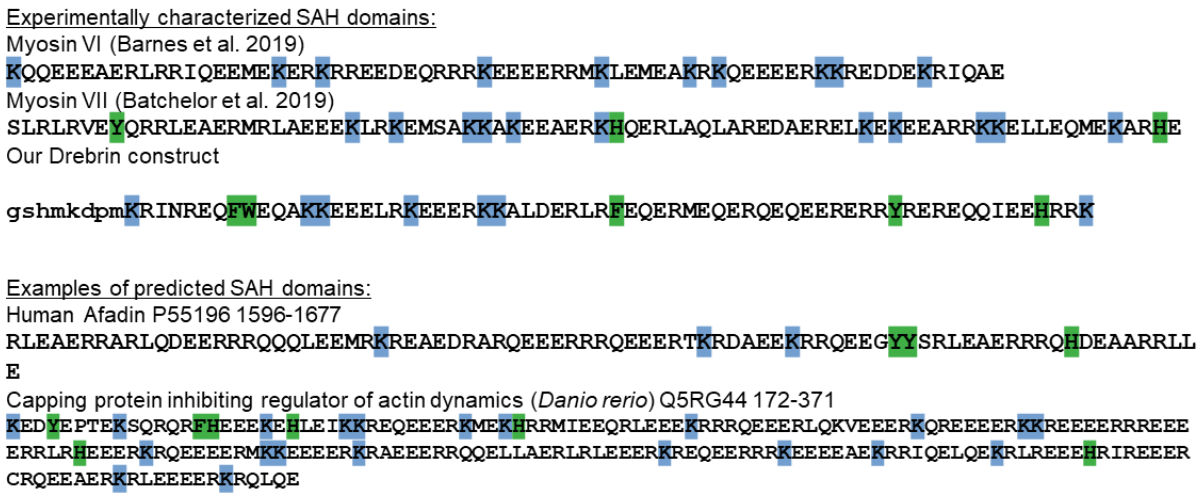

Figure 6: Comparison of the Drebrin-SAH region with SAH segments that have been extensively characterized by NMR so far.
Lysine residues are highlighted with blue background and aromatic residues with green background. Additional examples of two predicted SAH domains in two actin-interacting proteins are shown below. Both contain consecutive aromatic residues and exhibit a different distribution of lysines along the sequence.

2.1.5. The Homer-binding motifs in Drebrin

Besides the bundling and binding of actin filaments, Drebrin performs another important biological role through binding the other postsynaptic protein, Homer. The scaffold protein family Homer has 3 members (Homer 1, Homer2, Homer3), all of them contains an EVH1 (Ena/VASP Homology 1) domain which can recognize various PPXXF motif-containing proteins (14). The first consensus was that these PPXXF motifs are the only requirements of Homer-binding (39). However, Li and others rightfully pointed out that more than 10% of the total number of proteins in the human proteome includes at least one PPXXF region. It is doubtful that all of these proteins would be capable of Homer-binding, therefore the authors turned into the investigation of the flanking regions of these linear motifs (Figure 7). Drebrin has 2 PPXXF motifs, denoted as HBM (Homer Binding Motif). They have been found by investigation of different truncated Drebrin constructs, that the first (HBM1) motif can bind the Homer EVH1 domain, but the second one (HBM2) was insufficient. Interestingly, the construct containing both HBM1 and HBM2 showed a weaker binding (K_D=8.4±0.68 μM) compared to the one with only HBM1 (K_D=7.52±0.60 μM), strengthening their hypothesis, that Drebrin's primary Homer-binding site is centered around HBM1.

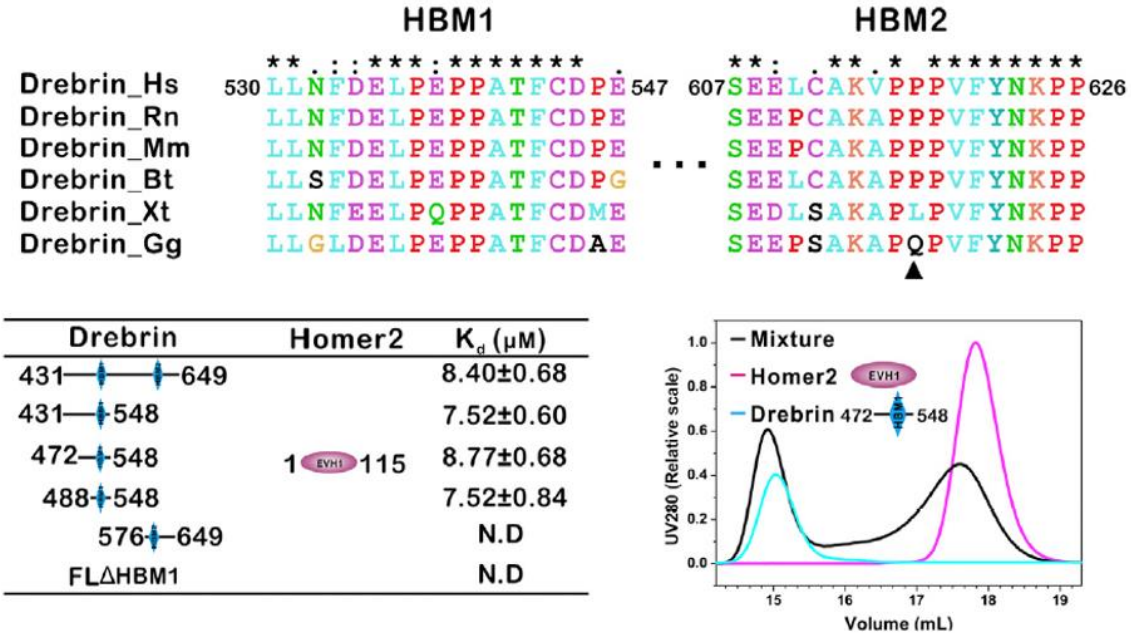

Figure 7: Sequence alignment of Drebrin sequences from different species showing the conserved HBM1 and the slightly less conserved HBM2.
The black triangle shows the less-conserved proline in the second PPXXF motif. Mm, mouse; Rn, rat; Hs, human; Bt, cattle; Xt, Xenopus tropicalis; Gg, chicken. ITC-derived dissociation constants of various Drebrin proteins and Homer2 EVH1 The mapping results show that Drebrin HBM1 (488–548) but not HBM2 can bind to Homer2 EVH1 with moderate affinity. N.D., not detectable. Analytical gel filtration chromatography showing the binding profile of Homer2 EVH1 to Drebrin HBM1 472–548. Figure is taken from (14).

The work of Li and others demonstrates that Homer EVH1 specifically binds to an extended sequence encompassing HBM1 but not HBM2. The main difference between the functionality of the two PPXXF motifs can be understood through the amino acid types in their flanking regions. In the case of HBM2, the phenylalanine in PPXXF is followed by bulky tyrosine, which is most likely enough to change the chemical environment of the linear motif. On the other hand, in HBM1, the PPXXF is followed by a rather flexible cysteine, which seems to be favored for the binding interface. This has been reinforced by experiments with construct mutated in specific positions, which is also thoroughly explained by the authors in their respective paper. The importance of flanking regions have been extensively investigated in the context of other protein-protein interactions as well (40–42). It is interesting to notice that even though the Drebrin-Homer interaction has been investigated on constructs with more than 100 residues, X-ray crystallography data is yet only available from a short peptide containing Drebrin HBM1 fused to the C terminus of Homer2 EVH1 with a 15 residue flexible linker (PDB:5ZZ9). Thus, there is still room for structural investigation of this protein-protein interaction, considering possible contributions of longer Drebrin segments.

2.2 Investigation of non-globular proteins

2.2.1. NMR spectroscopy-a key tool to acces protein dynamics

NMR (Nuclear Magnetic Resonance) spectroscopy is a primary example of the instrumental revolution in the 20th century (43). The discovery of magnetic resonance is originated to physicists (including but not limited to Isidor Isaac Rabi (44), Cornelius Jacobus Gorter (45), Felix Bloch (46) and Edward Mills Purcell (47)). The first aspects of NMR found to be useful for chemists were chemical shift and indirect spin-spin couplings (comprising, without being exhaustive Shrinivasa Shridhar Dharmatti (48), Norman Foster Ramsey Jr. (49), William George Proctor (50) and Herbert Sander Gutowsky (51)). As the field started to emerge rapidly after 1950, more and more biological questions were investigated by NMR spectroscopy, *inter alia* protein structures and dynamics, folding kinetics, ligand-binding and post-translational modifications. Thus, NMR is considered as a method bridging all natural sciences, with enormous versatility in its possible applications.

During the working years of this doctoral dissertation (2021-2025) the field of structural biology has been undergoing a revolution. The grueling work of solving protein structures with methods such as X-ray crystallography, cryo-electron microscopy and NMR spectroscopy has been vastly accelerated by the emergence of the newer versions of AlphaFold (52–54). The algorithm of AlphaFold has been trained on protein structures solved by X-ray crystallography, therefore it performs excellently on targets usually studied by this method: Globular proteins in monomeric form, with well-defined structure, consisting no or minor flexible segments. The natural consequence of that, is other types of proteins such as IDPs (intrinsically disordered proteins), oligomers, or fibrillar proteins such as coiled coils are predicted with lower confidence and accuracy (55). At this point, it is an actively ongoing question, which direction structural biologists should take, as beyond the remarkable results AlphaFold has been continuously providing, there are certain areas, where combining those with NMR yields in better synergy (56). Even during the writing period of this thesis, famous NMR-expert Lewis Kay has written an alerting review paper on aspects where NMR can outperform structure predictions, such as macromolecular complexes and phase-separated condensates (57).

It will be interesting to witness how machine learning-based techniques shape the future of structural biology and protein science. There are already emerging methods to extend AlphaFold to non-globular proteins (58,59), however at this point these techniques can not be considered well-established and widely used. Regardless to these outcomes, the good news for NMR spectroscopists, is that there will be always a need for they expertise, as NMR is capable of much more than solving protein structures in itself.

2.2.1.1. *Time dependence and conformational plasticity*

Protein structures either predicted by AlphaFold or solved by X-ray crystallography are excellent representations of a time-averaged conformation from a pool of conformers in dynamic exchange (60). Thus, they can be applied to deduce information about the arrangements of secondary structural elements and domains, which can already shed light on their functionality. However, the individual conformational states adopted by the protein are crucial for its functionality, so by simply viewing their average we might miss important details, or worse, end up with a conformational state that in itself can not even occur thermodynamically. Therefore, a comprehensive depiction of biomolecular dynamics is of high importance not only to complement the structural information but also for the thorough understanding of the biomolecular functional spectrum (61). Undoubtably, one of the main advantages of NMR techniques compared to crystallographic methods, is that the molecular motions can be captured on a broad timescale (Figure 8). Especially, solution NMR spectroscopy is one of the most powerful as well as most versatile techniques commonly used for the structural and dynamical characterization of proteins.

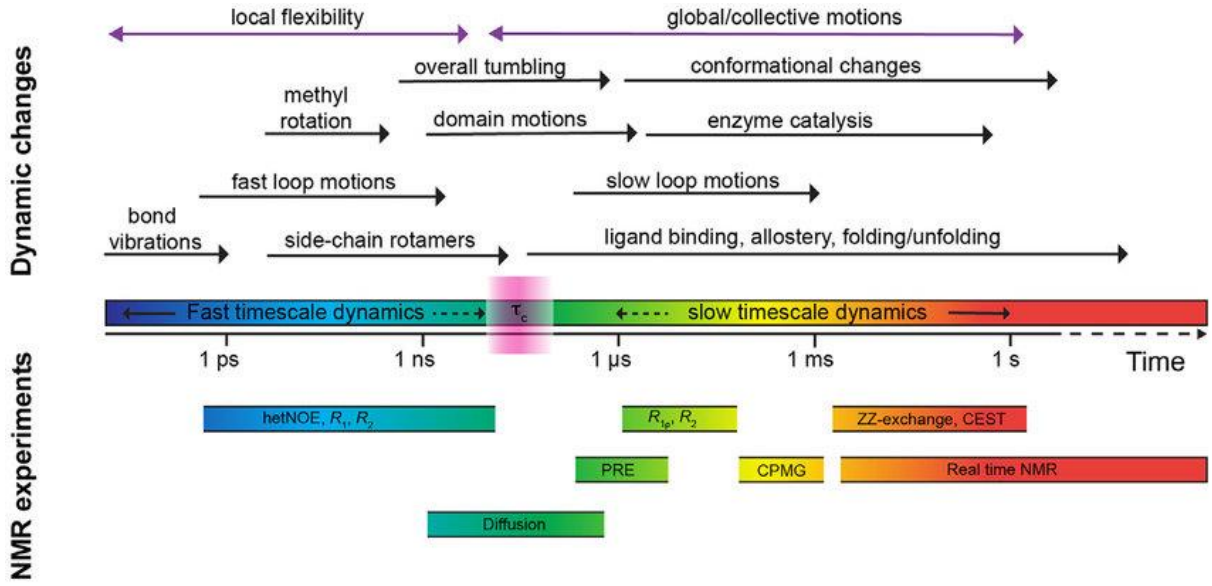

Figure 8: Timescales of protein dynamics and the corresponding NMR techniques.
Overview of the protein dynamics, timescale and available NMR methods to discern atomic-resolution information for the thorough understanding of the biomolecular dynamics. PRE: paramagnetic relaxation enhancement, CPMG: Carr Purcell-Meiboom-Gill relaxation dispersion; CEST: Chemical exchange saturation transfer. Figure is taken from (60).

2.2.1.2. The resonance assignment problem

In order to characterize protein structures and investigate their molecular motions, we first need to obtain fingerprint-like information, most commonly on the ^{1}H-^{15}N HSQC spectrum, termed as resonance-assignment. NMR assignment attempts are reported since the 1970s, notably from Kurt Wüthrich on the BPTI (Bovine Pancreatic Trypsin Inhibitor) protein (62). Subsequently, Wüthrich has been also the first one to report a complete 3D structure, also from BPTI (63). These landmark studies laid the foundation for the use of NMR spectroscopy in determining protein structures and dynamics. Because of this groundbreaking work, Kurt Wüthrich was awarded the 2002 Nobel Prize in Chemistry for "his development of NMR spectroscopy for determining the three-dimensional structure of biological macromolecules." The legacy of Wüthrich has been living on through the emergence of multidimensional NMR techniques, aiming to accelerate and extend resonance assignments of larger and more complex proteins. Heteronuclear 3D NMR has been applied to determine protein solution structures for many years. Scalar magnetization transfer through peptide bonds can be observed in triple resonance 3D NMR and thus makes the sequential assignment of a protein backbone more straightforward (64). This way, assigning globular proteins became more and more routine, exampled by the appearance of automated resonance-assignment algorithms (65–67).

The assignment procedure of IDPs is, on the other hand, much more complicated and requires methods tailored to this problem. One main issue is arising from the narrow distribution of amide proton chemical shifts in disordered proteins. Without a well-defined folding, the chemical environment of amide protons in IDPs is averaged out (68), dissimilarly to globular proteins, where contributions from different local environments yield in broad chemical shift dispersion. This effect however is more evident in the ^{1}H dimension with respect to the ^{15}N one, in agreement with the notion that heteronuclear spins are very important for the study of proteins in general but especially for the study of IDPs (69). This observation is particularly apparent if we compare the $^{1}H^{15}N$ HSQC spectra of the paradigmatic IDP, α-synuclein and one of the most investigated small globular protein, Ubiquitin (Figure 9).

The narrow amide proton chemical shift dispersion presents one of the main challenges for disordered proteins. Several 4-5 or even 6 dimensional NMR methods have been developed in order to overcome this limitation, although they resulted in long experiment time and complex data interpretation (70,71). In my thesis under the section “5.2.3 Drebrin D233 NMR assignment results” I demonstrate the successful application of 3D (HN)CO(CO)NH NMR spectroscopy (72,73) which tremendously reduced the number of multidimensional NMR experiments required and vastly accelerated the assignment procedure.

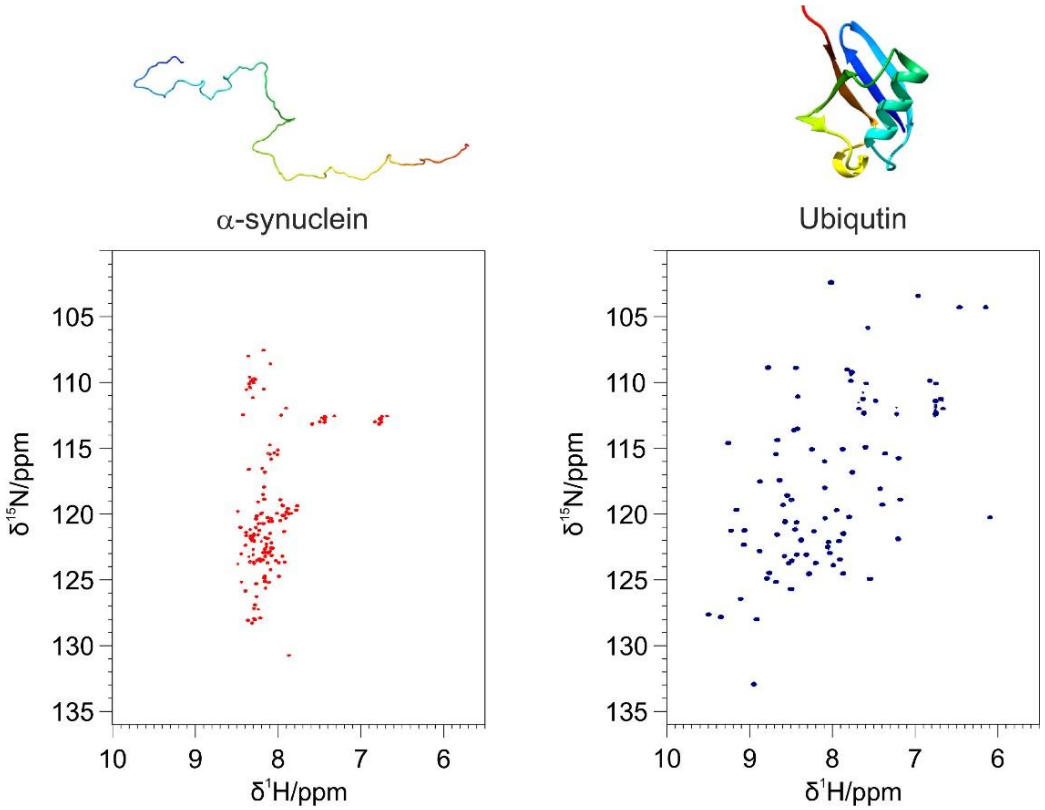

Figure 9: Impact of protein disorder and flexibility on NMR spectra.
The figure shows the comparison between the ^{1}H-^{15}N HSQC spectra of two proteins with different structural and dynamic properties: (left panel) an intrinsically disordered protein (α-synuclein); (right panel) a globular protein (ubiquitin). The left panel reports one of the possible conformers of α-synuclein, the right panel reports the ribbon representation of ubiquitin (PDB 1UBQ). The ^{1}H-^{15}N HSQC spectrum of α-synuclein is characterized by a low cross-peak dispersion and presents many peaks in overlap one to the other, a common feature of intrinsically disordered protein spectra. The ^{1}H-^{15}N HSQC spectrum of ubiquitin shows the large cross-peak dispersion typical of folded proteins. Figure is taken from(69).

2.2.1.3. NMR parameters to describe disordered proteins

Once the backbone and side-chain resonance assignments of a protein are obtained, structural information can be extracted from the NMR data. The first indicators of secondary structure tendencies — beyond the overall impression from the dispersion of the ^{1}H-^{15}N HSQC spectra — are the secondary chemical shifts. Chemical shifts provide sensitive, site-specific information from both the local structure and the dynamics of proteins. In particular, deviations from statistical average values, known as random coil chemical shifts (RCCSs), are widely used to infer local structural propensities (74). Among chemical shifts, the ^{13}Cα shifts are especially informative. They span a broad range (approximately 40–70 ppm), primarily reflecting the electron density effects of the side chain (75). The connection between deviations from random coil values and secondary structure propensities was first clearly described in 1990 by Mike P. Williamson and colleagues (76). Typically, the Cα chemical shifts are the most commonly analyzed: a

positive secondary shift suggests an α-helical environment, while a negative shift indicates a β-sheet conformation. To further exploit chemical shift data, programs such as CheSPI have been developed, which integrate chemical shift information from multiple nuclei, improving the accuracy and robustness of secondary structure predictions (77).

Chemical shifts are not only early indicators of structural preferences, but also excellent reporters of functionalities such as protein-protein interactions, or ligand-binding. The most frequently used approach for this purpose is the CSP (chemical shift perturbation) technique (78–82). This is an easy, cost-and time efficient method, where usually a ^{15}N labelled protein is titrated by the unlabeled partner, and the changes in the amide signals are tracked on $^{1}H^{15}N$ HSQC spectra. When following differences of amide peaks, we have to consider the fact that while shielding in nitrogen nuclei is stronger than in protons, the changes upon titration are bigger in the ^{15}N dimension. In order to address this effect, a scaling factor α for the combined chemical shift has been proposed by Mike P. Williamson in his famous article on the CSP phenomenon (83). The most common value chosen for the scaling factor α is 0.14, where

$$d = \sqrt{\frac{1}{2} + [\delta_H^2 + (\alpha\delta_N^2)]}$$

Another relatively straightforward to measure NMR data are the relaxation properties of different nuclei. In the context of NMR, the term relaxation means the process by which magnetization decays over time. This can be understood through 2 components: T1 relaxation (spin-lattice or longitudinal relaxation) refers to the recovery time of magnetization along z-axis, and T2 relaxation (spin-spin or transverse relaxation) refers to the loss of transverse magnetization (Figure 10).

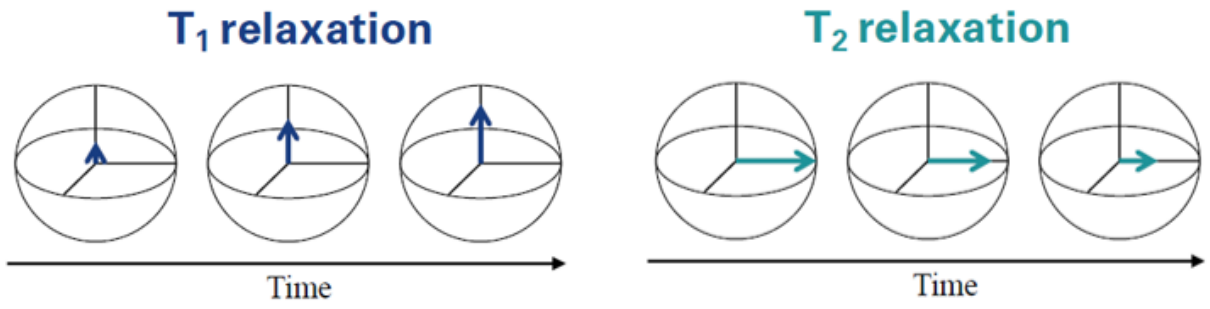

Figure 10: Magnetization returning to equilibrium over time by undergoing the two different processes of relaxation.
T1 relaxation (blue) and T2 relaxation (teal) of one highlighted spin after hit by a 90° pulse.

The relaxation times are often represented by their rates, and they are described by their respective Bloch-equations:

$$R_1 = \frac{1}{T_1}$$

$$R_2 = \frac{1}{T_2}$$

$$M_{\parallel} = M_{eq}{}^{(1-e^{-\frac{t}{T_1}})} \sim M_z$$

$$M_{\perp} = M_{eq}{}^{e^{-\frac{t}{T_2}}} \sim M_x M_y$$

In case of proteins, the most commonly investigated relaxational properties are the relaxation rates of ^{15}N spins of amide groups. To date, techniques for measuring ^{15}N relaxation are considered to be straightforward and robust (84). The factors affecting ^{15}N relaxation the most are the overall rotational correlation time (tumbling rate) of the protein and the internal flexibility of segments in the protein molecule. Since amide nitrogen relaxation is easily measured, it is one of the primary sources of structure validation as it is a good indicator of local flexibility. This can be further exploited in the context of protein-protein interactions, hence upon partner binding, the tumbling speed is decreasing, which can be nicely followed by the differences in relaxation rates. This methodology is particularly useful when it is difficult to localize the binding interface (85,86).

2.2.2. Small Angle X-ray scattering of proteins

2.2.2.1. SAXS as structure validation tool

As one of the key advantages of solution NMR techniques is the fact that we can investigate macromolecules in solution state, the same can be said from SAXS experiments as well. This gives structural biologists the unique ability to explore biomolecules under circumstances close to native conditions. The individual application of scattering methods for structural studies has its limitations, as the spherically averaged information in *ab initio* models can derive the 3 dimensional shape of the solutes with low resolution, introducing ambiguities (87). On the other hand, SAXS is considered to be at its best when complementary structural information is available. It is relatively easy to perform scattering experiments

(as compared to NMR spectroscopy: A magnitude lower sample amount is required, without isotopic labeling), and the resulting SAXS curve can be directly checked against atomic models, either solved by NMR spectroscopy or predicted computationally (88,89), thus experimentally cross-validating the results. It must be kept in mind that since an unambiguous dataset of coordinates can not be directly derived from the SAXS data, the fact that a model fitting the scattering data does not prove that the model in itself is correct. However, having the model characterized by other experimental techniques such as NMR, SAXS is an easily employable complementary technique for structural modeling.

2.2.2.2. SAXS of disordered proteins

Besides aiding protein structure modeling, SAXS can be also applied to characterize flexible macromolecules such as IDPs. Assumption of a dynamic system implies the use of the concept of "ensemble of conformations" to properly describe the data. In this case, the obtained SAXS curve can be considered the average of all conformations coexisting in solution. The goal of modelling flexible proteins is to optimize an ensemble of coordinates to simultaneously describe all data available, in contrast with modelling globular proteins, where optimization of a single set of coordinates to simultaneously describe all data is desired. The two philosophies underlying behind this methodology are Maximum Parsimony (90,91) and Maximum Entropy (92–94). In the context of IDPs, SAXS is once again shining the most during synergetic application with NMR (95,96), and with the help of computational tools (97,98). Discerning between flexible and rigid scenarios is fundamental, as *ab initio* rigid-body modeling of flexible proteins would yield in structurally meaningless and unreliable information. Luckily for both sides, information describing overall size and shape of highly flexible proteins derived from SAXS data complements very well the conformational sampling at residue level provided by NMR. The fact that such complex systems can be investigated and modeled such detailed foreshadows that even in the AlphaFold era, there is and there will be room for experimental structural biology. In fact, progress in the structural interpretation of SAXS data (in terms of conformational dynamics) will likely come from the development of theoretical methods to generate and perturb 3D structures more sophisticatedly.

3. Goals

The primary aim of my research was to achieve atomic-level insight into the intriguing non-globular regions of the neuronal Drebrin protein. These segments have remained largely uncharacterized due to the inherent challenges in their experimental investigation. My goal was to complement and reinforce existing findings from earlier functional studies of Drebrin, and to expand the current understanding by providing high-resolution structural information.

Therefore, I set the goal of characterizing the atomic level structural and dynamical features of the selected non-globular segments of Drebrin, the SAH and the actin-binding D233 (Drebrin residues 233-317) regions. To this end, I intended to perform the following investigation steps:

- Expression of the SAH segment in unlabeled, ^{15}N labeled and ^{13}C,^{15}N-labeled form
- Conducting CD and SAXS measurements on the SAH region for initial, low-resolution structural characterization
- Performing detailed NMR analysis on the SAH segment, including resonance assignment using non-conventional NMR techniques to overcome the expected spectral crowding
- Ensemble-based modeling of the Drebrin-SAH region based on the SAXS and NMR data obtained
- Expression of the D233 segment in unlabeled, ^{15}N labeled and ^{13}C,^{15}N-labeled form
- Conducting CD measurements on the D233 region to compare it with data available in the literature
- Performing pull-down assay investigation of the D233-F-actin interaction
- Performing detailed NMR analysis on the D233 segment, including resonance assignment using non-conventional NMR techniques to overcome the expected spectral crowding
- Performing functional investigations with NMR to assess the Drebrin-Actin interaction such as NMR titrations and relaxation measurements

(31,32)(99)In addition to optimizing the expression and purification of relevant protein segments and conducting NMR-based structural investigations, a key objective of my research was to interpret the findings within a broader structural and functional context. This combined approach aimed to describe the conformational behavior and structural tendencies of Drebrin's non-globular segments as comprehensively as possible, (Figure 11) bridging the gap between static structures and dynamic molecular function.

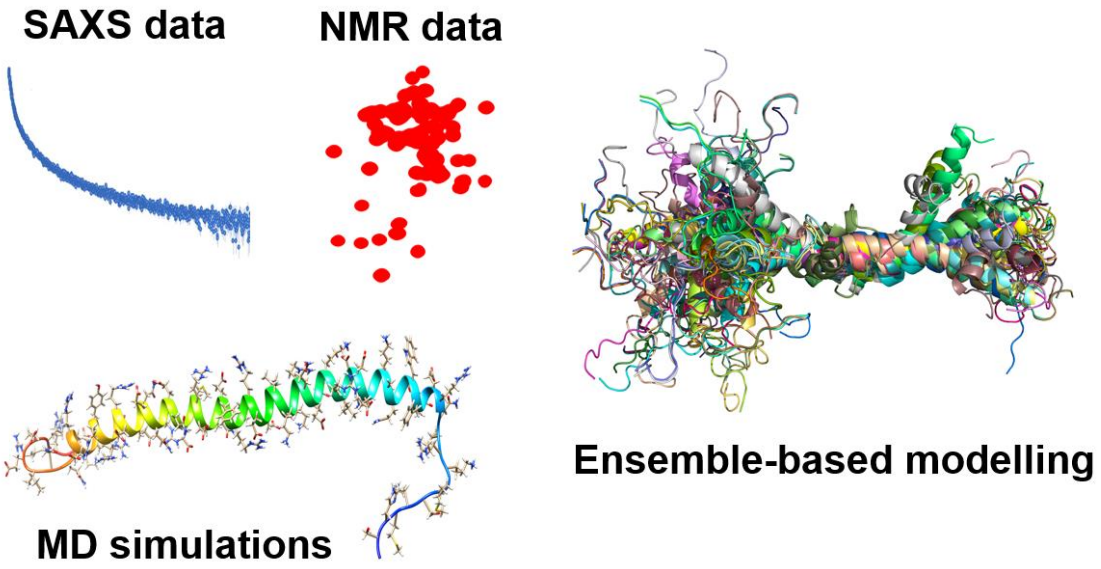

Figure 11: Simplified representation of the integrative modeling methodology.
A model consisting of 60 conformers was created using a selection procedure driven by SAXS and NMR experimental data and aided by MD simulations.

During the detailed investigation of the selected protein segments, I have tried to apply cutting edge methods, mostly complex NMR experiments (Figure 12). My goal was to simultaneously access previously undiscovered structural information while reinforcing the role of sophisticated NMR methodologies even in the Alphafold era in structural biology.

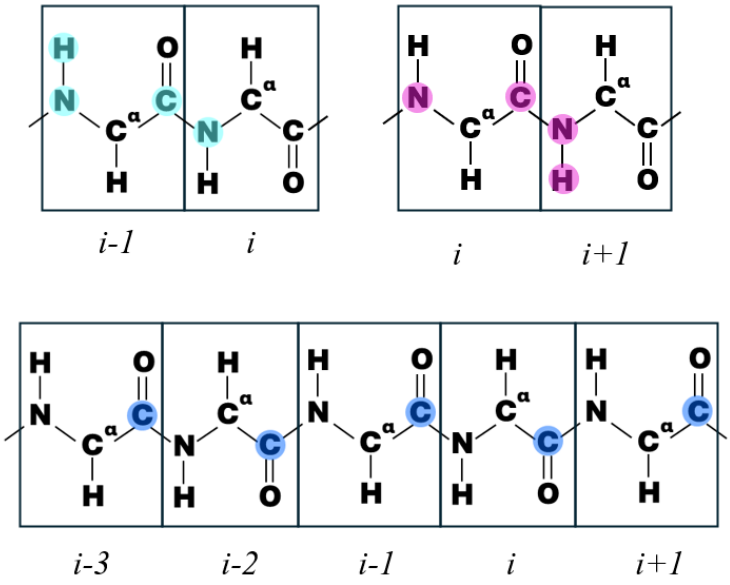

Figure 12: Special NMR techniques for low-complexity proteins used in backbone resonance assignment.
The correlated nuclei along the peptide chain highlighted in the 4D (HACA)CON(CA)NH (turqoise), the 4D (HACA)N(CA)CONH (purple) and the 3D (HN)CO(CO)NH (blue) experiments respectively.

4. Materials and methods

The majority of my experiments were conducted using either the D233 construct (Drebrin residues 233–317) or the Drebrin-SAH construct (Drebrin residues 173–238). While several aspects of the methodologies are similar, numerous minor optimizations of the protocols were needed. Consequently, I have structured this dissertation with separate chapters for the materials and methods, as well as the results, corresponding to Drebrin-SAH and D233. Since the work on Drebrin-SAH samples began earlier, and many of the protocols were subsequently refined during the investigation of D233, it is logical to begin by describing the procedures used in the Drebrin-SAH studies. Chapter 4 (Materials and methods) and Chapter 5 (Results) of this thesis contains quoted sections from my two first-author articles (11,100).

4.1 Drebrin-SAH experiments

4.1.1. Drebrin-SAH cloning, protein expression, and purification.

The DNA sequence of the full Drebrin protein (from Homo Sapiens, Uniprot Q16643) was a gift from Phillip Gordon-Weeks (Addgene plasmid #40362; http://n2t.net/addgene:40362; RRID: Addgene_40362) and used as template for cloning residues 173-238 into EcoRI and BamHI sites of a modified pET-15b vector (Novagen) with N-terminal 6xHis-tag and TEV cleavage site (ENLYFQG) using primers 5'-ttt ttg gat cca atg AAG CGG ATT AAC CGA GAG CA-3' (SAH forward) 3'-ttt ttg aat tct aTT TCC TCC TGT GCT CCT CGA TC-5' (SAH reverse). Expression of the corresponding construct was done with BL21 (DE3) E. coli bacteria cells in M9 minimal medium (101). To produce the necessary isotopically labelled samples, $^{15}NH_4Cl$ and ^{13}C D-glucose were supplemented as the only nitrogen and carbon source. Expression was induced with 1 mM of IPTG (Isopropyl β-D-1-thiogalactopyranoside) at 6 MFU (McFarland Unit) density and cells were harvested by centrifugation after 3 hours incubation at 37°C. The proteins were extracted from the bacterial pellets with sonication in native phosphate buffer (pH=7.4, 300 mM NaCl, 43 mM Na_2HPO_4, 7 mM NaH_2PO_4). The resulting lysate was centrifuged at 14881 x g for 20 min at 4°C, and the supernatant was then filtered through a 0.45 μm filter before purification. The His-tagged protein was purified with a Bio-ScaleTM 5 ml NuviaTM IMAC Ni-affinity column (Bio-Rad). Nonspecifically bound proteins were washed from the column with binding buffer supplemented with 25 mM of imidazole. SAH protein was eluted with an imidazole gradient / 250 mM imidazole. Tobacco Etch Virus (TEV) protease was used for cleaving the His-tag by incubating with the protein for 20 hours at room

temperature. This yielded an 8 residue-long (GSHMKDPM) linker remaining upstream the N-terminal of the SAH sequence. Before the ion exchange chromatography, the buffer was changed to a Low Salt Binding buffer (20 mM NaCl, 42 mM NaH_2PO_4, 8 mM Na_2HPO_4, pH=6.0) using HiTrap Desalting column with Sephadex G-25 resin (Cytiva). For the ion exchange chromatography, Bio-ScaleTM Mini Macro-PrepTM High S column was used, and the protein was eluted in a High Salt Elution buffer (1 M NaCl, 46 mM Na_2HPO_4, 4 mM NaH_2PO_4, pH=7.4). Ultrafiltration was applied using Amicon® Ultra Centrifugal Filter (3 kDa MWCO, Merck, cat#: UFC9003) to concentrate the samples before size exclusion chromatography with SEC70 10x300 mm analytical gel chromatographic column (Bio-Rad). The SAH protein construct used for all structural investigations had the following sequence: gshmkdpm KRINREQFWE QAKKEEELRKE EERKKALDER LRFEQERMEQ ERQEQEERER RYREREQQIE EHRRK. The expected molecular weight of the protein assuming natural isotopic abundance is 9727.75 Da. The purity and integrity of the sample was analyzed by SDS-PAGE.

4.1.2. Drebrin-SAH circular dichroism experiments

ECD measurements were conducted at the Separation Science Research and Education Laboratory of Eötvös Loránd University on a Jasco 1500 CD spectrometer (JASCO Corporation, Tokyo, Japan) (A040661638) using a Jasco J/21 cuvette with 1 mm path length. Drebrin-SAH samples were diluted to 14 µM in Low Salt Buffer (42 mM NaH_2PO_4, 8 mM Na_2HPO_4, 20 mM NaCl, pH=6). ECD spectra were recorded at 20°C with the following parameters: 195–250 nm spectral range, 50 nm/min scanning speed, 1 nm bandwidth, 0.2 nm step size, 0.5 s response time and 3 scans of accumulation. Temperature dependence of helicity was investigated by measuring the ellipticity at 222 nm while heating with a rate of 1 °C/min in the temperature range 5-80 °C recording with 0.5°C increments. Obtained results were compared with CD data of other proteins, published earlier (102), kindly provided by Dániel Süveges. Secondary structure content was determined from the mean residual ellipticity values with the BeStSel software (103).

4.1.3. Drebrin-SAH NMR experiments

NMR spectra were recorded on a 800 MHz Bruker Avance III HD spectrometer equipped with a ^{1}H, ^{13}C, ^{15}N triple resonance helium cooled cryoprobe. Initially, the feasibility of ^{15}N, ^{13}C labeled SAH for structural characterization was evaluated at pH=7.4 using ^{1}H-^{15}N HSQC spectra. However, due to severe exchange broadening of several amide cross peaks, we decided to lower pH to 6.0 in order to reduce the NH exchange rate with the solvent. All further NMR experiments were conducted at 25 °C using 350 µM

sample in 17 mM NaH_2PO_4, 3 mM Na_2HPO_4, 50 mM NaCl, pH 6 with 1 mM NaN_3. Neither the applied change in the pH nor the alteration of the salt concentration is expected to substantially influence the helicity of the construct. The pKa values of the side chains are well outside of the pH range used, and the helicity of other SAHs only decreases at salt concentrations that are higher by about two orders of magnitude (102). The ^{1}H-^{15}N HSQC spectrum of Drebrin-SAH only resolved around 50 backbone amide peaks of the total 73 expected, and the standard triple resonance experiments namely HNCO, i(HCA)CO(CA)NH (also referred as iHNCO), HNCOCACB, HNCACB resulted in severe signal overlap, as was expected by the repetitive low-complexity nature of the protein sequence. Therefore, the 4D (HACA)N(CA)CONH experiment was pivotal to find CO(i)-N(i)-N(i+1)-HN(i+1) correlations and lead the sequential walkthrough, supported by the 3D (H)CC(CO)NH experiments to identify residue types by aliphatic C and H chemical shifts. To reduce the long experimental time of the 4D measurement, 7% nonuniform sampling was used with acquisition times of 14.5 ms (^{1}H, t1), 17.3 ms (^{15}N, t2), 17.3 ms (^{15}N, t3), 8 ms (^{13}C, t4). The ^{1}H-^{15}N HSQC spectrum was repeatedly measured during the collection of spectra for the assignment to monitor the sample integrity. We observed small signs of degradation after several days, however the backbone assignment was feasible. All data were processed using Topspin 3.5 software package (RRID:SCR_014227) and assignments were made by CCPN software(104). Figures have been created by either CCPN or Poky (105). A list of NMR experiments and their detailed descriptions are available (Table 1).

Experiment	Reference	Used for
^{1}H-^{15}N HSQC with Rance-Kay SE, water flip-back pulse ^{15}N	(106)	Fingerprint of NH residues
HNCO with Rance-Kay SE ^{15}N, ^{13}C	(107)	Triple resonance residue i-1 CO assignment
iHNCO with Rance-Kay SE ^{15}N, ^{13}C	(71)	Triple resonance residue i CO assignment
(H)CC(CO)NH with Rance-Kay SE DIPSI-2 spin-lock ^{15}N ^{13}C	(108)	Residue i-1 aliphatic side chain 13C assignment
H(CC)(CO)NH with Rance-Kay SE DIPSI-2 spin-lock ^{15}N ^{13}C	(108)	Residue i-1 aliphatic side chain 1H assignment
(HACA)N(CA)CONH with Rance-Kay SE ^{15}N ^{13}C	(109)	4D CO(i)-N(i)-(Ni+1)-HN(i+1) correlations

Table 1: List of NMR experiments used for Drebrin-SAH resonance assignment

4.1.4. Drebrin-SAH SAXS experiments

Small angle X-ray scattering data ($I(s)$ vs. s, where $s = 4\pi\sin q/\lambda$, λ is the X-ray wavelength 0.123982 nm (10 keV) and $2q$ the scattering angle) were measured at the EMBL-P12 bioSAXS beam line (DESY, Hamburg Germany (110)) from samples of purified Drebrin-SAH at 88, 175 and 350 µM and a corresponding matched buffer (17 mM NaH_2PO_4, 3 mM Na_2HPO_4, 50 mM NaCl, pH=6). Samples were delivered using standard temperature-controlled batch mode operations at 20°C. The data were recorded as sequential sets of 0.1 s individual 2D data frames (Pilatus 6M detector) that underwent subsequent azimuthal averaging to produce 1D scattering profiles normalized to beam transmission (111). Those 1D data frames assessed to be statistically dissimilar (112), e.g., affected by radiation damage, were removed prior to the final averaging of the sample and buffer frames. The buffer scattering was then subtracted from the sample scattering to produce the final reduced and background-corrected SAXS profiles of the SAH samples at each respective concentration. Additional details on data acquisition are listed in the SAXS reporting table (Table 3).

4.1.4.1. Primary SAXS data analysis

Primary SAXS data analysis was performed using the ATSAS 3 software package (113). The radius of gyration, R_g and forward scattering intensity at zero angle, $I(0)$ were determined from both the Guinier approximation ($\ln(I(s))$ vs. s^2, for $sR_g < 1.2$ (114)) and from the scattering pair distance distribution function, or $p(r)$ profile, calculated using GNOM (115) that also provided estimates of the particle maximum dimension, D_{max}. The Porod volume, V_p, and concentration-independent molecular weight estimates were determined using the ATSAS 3 modules DATPORD and DATMW (116), respectively, using the GNOM outputs for the evaluation. Dimensionless Kratky plots of the SAXS data ($sR_g^2(I(s)/I(0))$vs. sR_g) followed the procedure of Receveur-Bréchot and Durand (117). Additional parameters and details such as the measured and working s-ranges of each dataset, Guinier limits/datapoints used for analysis, quality of parameter fits, etc., are reported in the SAXS reporting table (Table 3).

4.1.4.2. Ab initio dummy atom modelling

The SAXS data from the 350 µM sample underwent ab initio dummy atom (DAM) bead modelling to assess the overall structural disposition of SAH. DAMMIF (118) was run several times to generate a 10-member individual DAM model cohort. This cohort underwent subsequent spatial alignment using

DAMSEL, DAMSUP and DAMAVER routines (119) to produce shape, volume and bead-occupancy weighted DAM models DAMAVER, DAMFILT and DAMSTART. The DAMSTART model underwent further refinement in DAMMIN (120) to generate an individual model that fits the data reflecting the overall consensus shape and disposition of Drebrin-SAH in solution. In all cases, data-model fits were assessed using the reduced χ^2 test and Correlation Map (CorMap) P-value (112).

4.1.4.3. Ultra-high Performance Liquid Chromatography and Multi-Angle Light Scattering Size Exclusion Chromatography Experiments

For measuring exact molecular mass, Drebrin-SAH samples in Low Salt Buffer (42 mM NaH_2PO_4, 8 mM Na_2HPO_4, 20 mM NaCl, pH=6, 550 µM) were diluted 50x in H2O and analyzed by Q-TOF MS analysis. To exclude the possibility of potential oligomer forms flying apart and leading to false MW results, additional MALLS-SEC experiments were conducted to prove the monomeric state of the protein in solution.

4.1.4.4. SEC-MALLS Materials and Methods

Size exclusion chromatography (SEC) coupled to multi-angle laser light scattering (MALLS) and refractive index (RI) measurements were performed to evaluate the molecular mass of the Drebrin-SAH. A sample of Drebrin-SAH, 100 µl at 220 µM, was injected onto a Cytiva Superdex Increase 75 5/150 column equilibrated with 17 mM NaH_2PO_4, 3 mM Na_2HPO_4, 50 mM NaCl, pH=6 at a flow rate of 0.3 mL/min. MALLS/RI data from the continuously-flowing SEC-column eluate were measured using a Wyatt (Germany) miniDAWN® TREOS® (3-angle MALLS) instrument and an Optilab T-rEX refractometer. The refractive index increment at 25 °C for the Drebrin-SAH (dn/dc = 0.1931 mL/g) was estimated using the vbar-dndc calculator of SEDFIT (121) based on the absolute RI of the SEC running buffer (1.3317), the SAH amino acid sequence, incident λ (658 nm) and sample temperature. The subsequent molecular weight estimates through the major SEC elution peak were determined from the MALLS scattering intensities and the RI estimate of protein concentration using Wyatt ASTRA 7.0.1 software.

4.1.5. Drebrin-SAH conformer generation and selection

Conformer generation was performed with DIPEND (33). DIPEND uses neighbor-dependent Ramachandran preferences that can be modified by adding a user-defined distribution. Based on the results of several exploratory calculations, we have increased the frequency of sampling helical conformations in several regions of the construct as shown in Figure 13. The generated structures were allowed to deviate from a straight helical one, even by allowing the random presence of cis amide bonds not exceeding the frequency observed for non-proline residues (122). Using these settings, a set of 5,000 conformers were generated, each of which was then subjected to a short, 10 ps molecular dynamics (MD) run in vacuum using GROMACS (123) and the AMER99SB-ILDN force field (124) resulting in a total of 30,000 conformers, used as an initial pool.

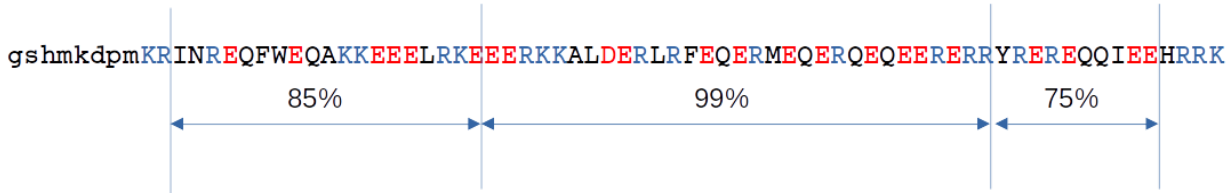

Figure 13: Helical preferences set for different regions of the Drebrin-SAH construct used for conformer generation with DIPEND.

From this initial pool, 5,000 conformers were selected randomly, and these were used as an input for the CoNSensX+ method to select a subset of conformers corresponding to Cα, Cβ chemical shifts as well as to the measured SAXS curve. For this purpose, the SAXS evaluation feature was added to the dockerized version of CoNSEnsX+ (125) (by incorporating the Pepsi-SAXS method (89). For the chemical shift selection, the RMSD metric was used, the SAXS fit was evaluated using the standard $\chi 2$ metric. This procedure - selecting 5,000 conformers randomly and then getting a subset with best correspondence to experimental data - was repeated five times.

To assess the role of side chain conformations, backbone-restrained MD calculations of 20 ns were run in explicit water on each conformer that was included in any of the selected ensembles from the initial pool. The AMBER99SB-ILDN force field and the SPC/E water model (126) was used, structures were put in a rectangular box with walls 1 nm from the nearest atom. Using the default charges, no additional neutralization was necessary. After minimization and two 1 ns equilibration rounds under NVT and NPT conditions with position restraints on all heavy atoms, position restraints on the backbone heavy atoms (N, C, O, Cα) were applied in the production runs. A second pool of conformers was compiled by including 41 conformers from each the 20 ns MD runs by sampling the structures at every 500 ps. Based on an exploratory analysis, conformations containing cis amide bonds were not included in this pool as they were

not required to obtain ensembles with satisfactory correspondence to the experimental (primarily SAXS) data. Termed secondary pool, this conformer set was used as input for a final round of selection based on experimental data with CoNSEnsX+. The selection procedure is summarized in Figure 14.

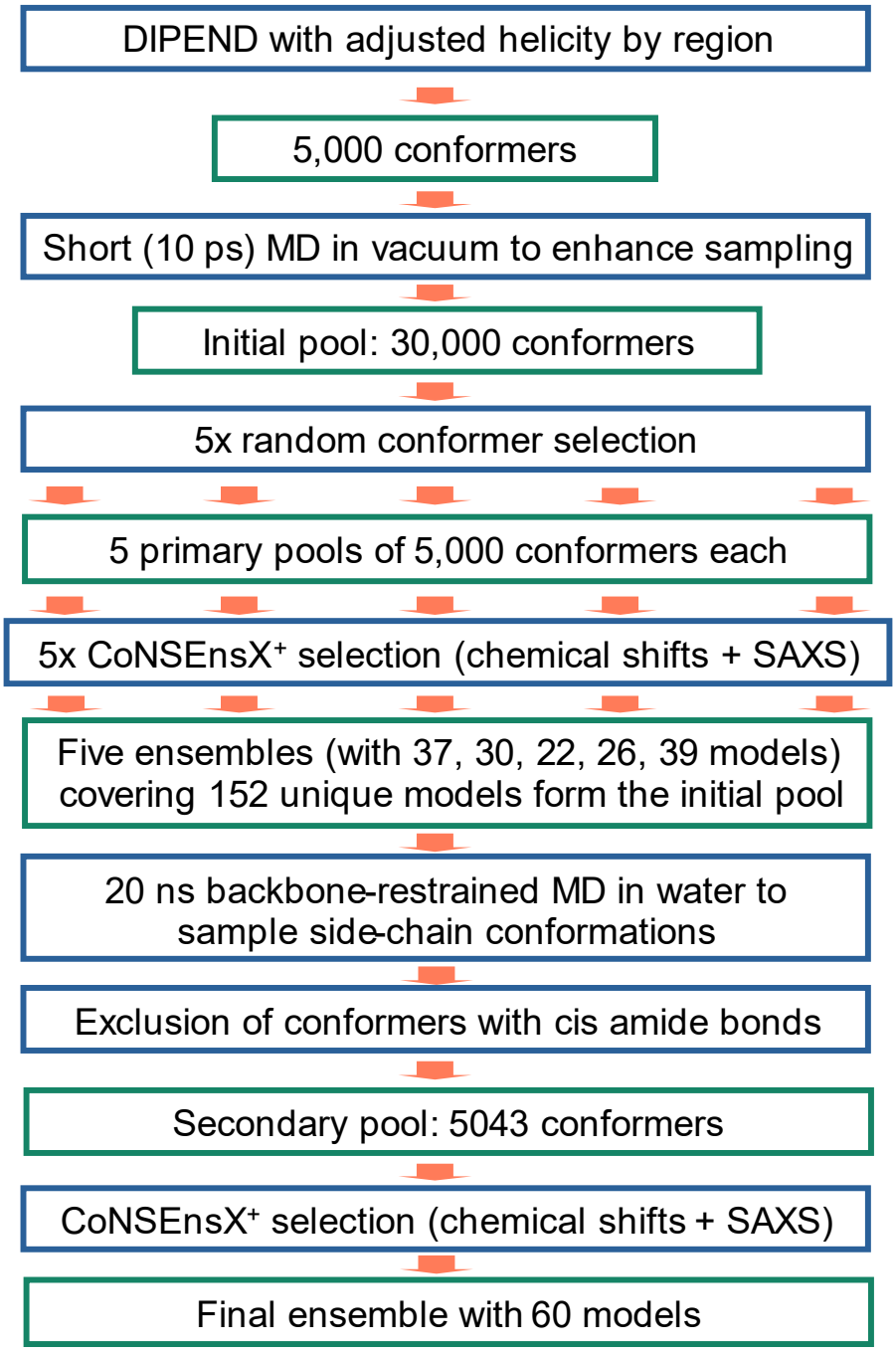

Figure 14: Flowchart of the ensemble selection protocol applied.
Methodology steps are highlighted in blue, and conformer subensembles are highlighted in green boxes.

Correspondence of the selected ensembles with experimental data was assessed using SHIFTX2 (127) and Pepsi-SAXS incorporated into CoNSEnsX+. In addition, the radius of gyration (R_g) and the distance between the Cα atoms of the terminal residues (Gly1 and Lys74) were calculated for each conformer by in-house Python scripts. Superposition of the structures was performed using MOLMOL (128). Structural details were visualized with Chimera (129). Secondary structure analysis was performed using DSSPcont that assigns a probability of each secondary structure state to each residue (130) . DSSPcont output for individual conformers was processed by an in-house script to obtain averaged secondary structure states over the ensemble. The obtained secondary structure state percentages for each residue were used to create an 'alignment' file which could be used as input to WebLogo (131) to generate a logo reflecting the occurrence of secondary structure states for each residue in the ensemble.

Analysis of salt bridges was done with an in-house Perl script according to the criterion described by Barlow and Thornton (132) also used in a more recent comprehensive analysis (133). This requires a distance below 0.4 nm between any side-chain oxygen and nitrogen atoms in Asp/Glu and Arg/Lys residues, respectively. Identification of possible cation-π interactions was performed with an in-house script using 5 characteristic distances between the charged groups of Lys and Arg and the aromatic rings.

Although energy-based identification is favored in the analysis of cation-π interactions (134), in this study we applied a simple geometry-based criterion for three reasons. First, the analyzed geometries stem from classical molecular dynamics calculations, providing geometries not expected to precisely match one optimized at a higher level of theory. Second, as also emphasized elsewhere, our model ensemble is not expected to provide a thermodynamically balanced sample and is also too small to represent exhaustive sampling. Thus, the observed interactions can only be regarded as ones that can be reasonably formed during the internal dynamic rearrangements of the side chains, not as contacts supported by direct experimental evidence. Third, we have also used a simple geometry-based criterion for salt bridge identification, applying similar criteria is more in line with our analysis. For each Phe/Tyr/Trp – Arg/Lys pair, five distances were defined and all of them were required to be below 0.6 nm: 1) the plane of the aromatic ring to Arg Cζ / Lys Nζ , 2) the plane f the aromatic ring to Arg Nε / Lys Cε, 3) Phe/Tyr/Trp Cδ1 to Arg Cζ / Lys Nζ , 4) Phe/Tyr Cδ2 or Trp Cη2 to Arg Cζ / Lys Nζ and 5) Phe/Tyr Cζ or Trp Cε2 to Arg Cζ / Lys Nζ. Requiring these distances to be below 6 Å still allows various relative orientations of the charged groups to the aromatic rings while ensuring that multiple atoms are close to each other to suggest an interaction of non-negligible strength.

4.2 Drebrin D233 experiments

4.2.1. Drebrin D233 cloning, protein expression and purification

The DNA sequence of the full Drebrin protein (from Homo sapiens Uniprot Q16643) was a gift from Phillip Gordon-Weeks (Addgene plasmid #40362; http://n2t.net/addgene:40362;RRID: Addgene_40362) and used as template for cloning residues 233-317 into NdeI and HindIII sites of a modified pET-15b vector (Novagen) with N-terminal 6xHis-tag and TEV cleavage site (ENLYFQG) using primers 5'-aa aaa cat atg GAG GAG CAC AGG AGG AAA C-3' (D233 forward) 3'- aaa AAG CTT CTA TCG ATG GTT GAA GGG CG-5' (D233 reverse). We used BL21 (DE3) E. coli cells for expressing the protein in M9 minimal medium enriched with 1.5 g/l $^{15}NH_4Cl$ and 2.5 g/l ^{13}C D-glucose as the only nitrogen and carbon sources. After reaching OD600=1.0, expression was induced with 1 mM isopropyl β-D-1-thiogalactopyranoside (IPTG), and cells were incubated for 3 h at 37 °C before harvesting by centrifugation. The cells were extracted by sonication using lysis buffer (300 mM NaCl, 43 mM Na_2HPO_4, 7 mM NaH_2PO_4, 5 mM β-Mercaptoethanol, 1 mM AEBSF protease inhibitor cocktail, pH 7.4), and the lysate was centrifuged at 2423xg for 20 min at 4°C. The resulting supernatant was filtered through a 0.45 µm membrane prior to chromatography. A Ni2+-affinity column (Bio-Scale 5 ml Nuvia IMAC) equilibrated with binding buffer (300 mM NaCl, 43 mM Na_2HPO_4, 7 mM NaH_2PO_4, 5 mM β-Mercaptoethanol, pH 7.4) was used to purify His-tagged D233. D233 was eluted with an imidazole gradient / 500 mM imidazole, followed by the cleavage of the His-tag with Tobacco Etch Virus (TEV) protease. Prior to ion exchange chromatography, the buffer was exchanged to a low salt binding buffer (20 mM NaCl, 35 mM NaH_2PO_4, 15 mM Na_2HPO_4, 5 mM β-Mercaptoethanol, pH 6.5), followed by purification using a Q column (Bio-Scale Mini Macro-Prep). The protein was collected in the flow through fraction and concentrated using Amicon Ultra Centrifugal Filter (3 kDa MWCO). The D233 protein construct used for NMR experiments had the following sequence: gshmEEHRRK QQTLEAEEAK RRLKEQSIFG DHRDEEEETH MKKSESEVEE AAAIIAQRPD NPREFFKQQE RVASASAGSC DVPSPFNHR. Assuming natural isotopic abundance, the molecular weight of D233 is 10.32 kDa, which matched migration on SDS-PAGE.

4.2.2. Drebrin D233 CD experiments

ECD measurements were conducted at the Separation Science Research and Education Laboratory of Eötvös Loránd University on a Jasco 1500 CD spectrometer (JASCO Corporation, Tokyo, Japan) (A040661638) using a Jasco J/21 cuvette with 1 mm path length. Drebrin-D233 samples were diluted to 20

μM in Low Salt Buffer (42 mM NaH_2PO_4, 8 mM Na_2HPO_4, 20 mM NaCl, pH=7.4). ECD spectra were recorded at 20°C with the following parameters: 195–260 nm spectral range, 50 nm/min scanning speed, 1 nm bandwidth, 0.2 nm step size, 0.5 s response time and 3 scans of accumulation.

4.2.3. Drebrin D233 Pull-down assay

To assess the functionality of His-tagged Drebrin protein constructs in terms of their ability to bind F-actin, I established a pull-down assay optimized for qualitative binding assessment (Figure 15). This assay served as an essential first step before moving on to more detailed biophysical characterizations, such as NMR or SAXS. Given that the initial step of the protein purification workflow involved Ni-NTA affinity chromatography, it was both efficient and logical to reuse the His-tag as an anchor for immobilization in the pull-down setup. Naturally, the following steps (especially TEV-cleavage) of the protocol designed for purifying an NMR-quality sample were not performed during these batches. During preliminary trials, it became evident that F-actin displayed a degree of nonspecific adherence to Ni-NTA beads, compromising assay selectivity. To overcome this, additives were necessary to reduce the aspecific binding of F-Actin. The working buffer (in which protein samples were also diluted) contained 17 mM NaH_2PO_4, 3 mM Na_2HPO_4, 50 mM KCl, 2 mM $MgCl_2$, 1 mM ATP, 5 mM TCEP, 20 mM Imidazole and 0,1% Tween-20 detergent). The protocol of the assay had the following steps:

- Equilibration of 10 μL Ni-NTA resin beads with working buffer
- Addition of 50 μl His-tagged D233 (10 μM)
- Two washing steps with 500 μL working buffer to remove unbound protein
- Addition of 50 μl F-Actin (10 μM)
- Three washing steps with 500 μL working buffer to remove unbound or loosely associated F-actin
- Elution with 50 μl of working buffer adjusted to 250 mM Imidazole content

The supernatant from each step, as well as the final elution fraction, was collected for SDS-PAGE analysis. This allowed the assessment of co-elution of F-actin with the Drebrin construct and thus served as a qualitative proof of the interaction under these conditions.

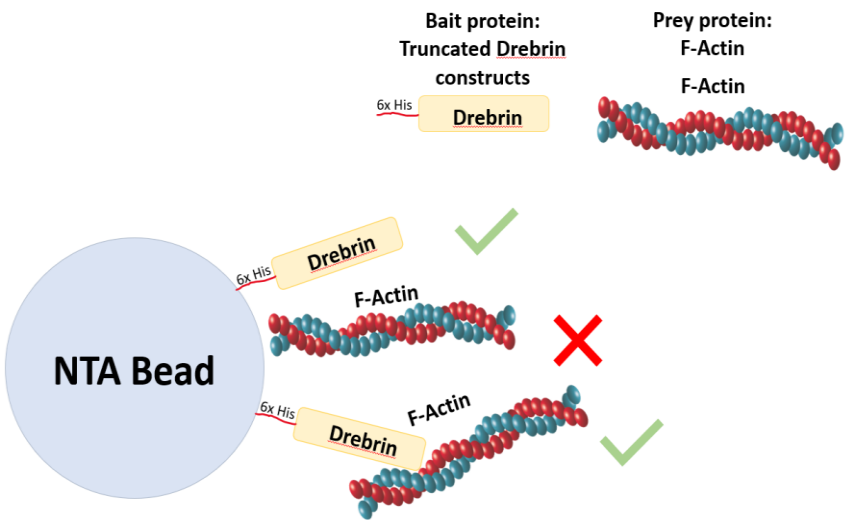

Figure 15: Schematic view of the pull-down assay designed for screening actin-binding Drebrin constructs. Under proper conditions, only the His-tagged bait protein (in this case, D233) could bind to the beads. Prey protein (F-actin) can only occur in the elution fraction, if it was bound to the bait before.

4.2.4. Drebrin D233 NMR experiments

The ^{15}N, ^{13}C labelled D233 sample in NMR buffer (50 mM NaCl, 17 mM NaH_2PO_4, 3 mM Na_2HPO_4, pH 6.0, 5 mM TCEP, 10 % (v/v) D_2O) was transferred to 5 mm NMR tubes with a final protein concentration of 0.3 mM. Data were collected at 25 °C, using a 700 MHz Bruker Avance III NMR spectrometer equipped with a cryogenically cooled TCI probe head with single-axis field gradient. DSS (2,2-dimethyl-2-silapentane-5-sulfonate sodium salt) was used for direct ^{1}H chemical shift referencing, while ^{15}N and ^{13}C chemical shifts were referenced indirectly following the IUPAC definition (135). The backbone assignment strategy made use of long-range carbonyl-carbonyl correlations to bypass the chemical shift degeneracy of amide protons; The 3D (HN)CO(CO)NH experiment takes advantage of the favorable relaxational properties of ^{13}C carbonyl nuclei, due to their rapid segmental dynamics in disordered segments. This enables a particularly long acquisition using a semi-constant time t1-evolution, in the ^{13}C indirect dimension, thereby increasing the resolution. The MOCCA-XY16 pulse scheme allows an extremely long isotropic mixing time making it possible to correlate several adjacent residues. In our experiments, an isotropic mixing time of 500 ms was used, therefore we were able to obtain correlations between up to 5 neighboring amino acids. The experiment also provided some directional information encoded in the peak intensities, with the less intense signals being further removed in sequence from the NH group in question. The assignment procedure was further aided by the information on amino acid type obtained from a 3D (H)CC(CO)NH experiment. To further support the assignment, HNCO and HN(CA)CO experiments were also recorded.

In order to investigate the effect of ATP addition to D233, explorative stepwise titration (0,2 mM, 1 mM, 2 mM ATP concentration) was performed with a stock solution of 25 mM ATP to see if there are notable chemical shift perturbations. "D233 without ATP" sample contained 500 µl of 300 µM ^{15}N labelled D233 in 50 mM KCl, 17 mM NaH_2PO_4, 3 mM Na_2HPO_4, 2mM $MgCl_2$, 5mM TCEP, pH=6.

In order to obtain R2 rates, the corresponding "15N_T2_HSQC" experiment from the NMRlib package (136) was used as pseudo-3D experiment. This pre-defined setup included sensitivity improvement and temperature compensation while using shorter CPMG cycles. The d31 value was chosen to be 0.0086 s. Delays ranged from 8,6 to 344 ms with randomized order (0.0086 s, 0.1376 s, 0.2752 s, 0.0172 s, 0.172 s, 0.3268 s, 0.0344 s, 0.2064 s, 0.086 s, 0.2408 s, 0.3784 s, 0.2064 s, 0.344 s, 0.0688 s). Collected spectra were processed equally and loaded into CCPNMr in order to extract relaxation decays for each residue where it was possible. "D233 without F-actin" sample contained 350 µl of 300 µM ^{15}N labelled D233 in 50 mM KCl, 17 mM NaH_2PO_4, 3 mM Na_2HPO_4, 2mM $MgCl_2$, 5mM TCEP, 1mM ATP, pH=6 and additional 150 µl buffer, while the "D233 with F-actin" sample contained 350 µl of ^{15}N labelled D233 in 50 mM KCl, 17 mM NaH_2PO_4, 3 mM Na_2HPO_4, 2mM $MgCl_2$, 5mM TCEP, 1mM ATP, pH=6 and 150 µl 10 µM F-actin in the same buffer. The comparison of the 2 initial HSQC spectra (without any delay) is shown in the results section (Figure 35: Exploratory NMR titrations of D233.A, ^{1}H-^{15}N HSQC spectrum of D233 overlayed with a spectrum of D233 in the presence of F-actin.) and further referred to as "D233 titration with F-Actin".

5. Results

5.1 Drebrin-SAH results

5.1.1. Drebrin-SAH CD results

CD spectra recorded from the Drebrin-SAH demonstrates that the recombinant protein forms a stable alpha-helix in solution (Figure 16A). The Drebrin-SAH is estimated to exhibit about 63% helicity, slightly lower than that of the GCP60 and M4K4 SAH regions reported earlier (102) (Table 2). However, this value is strongly influenced by the fact that in our 74-residue Drebrin-SAH construct, the first eight residues originate from the non-native linker sequence that remains after TEV cleavage that probably has no regular secondary structure. Throughout the article, we provide amino acid numbering for the full human Drebrin (UniProt Q16643) in square brackets following the residue positions in our construct. Temperature dependence of Drebrin-SAH was monitored at 222 nm (Figure 16B) and compared to previously reported SAH segments from myosin VI, GCP60, and M4K4 in addition to the coiled-coil region of GCN4. While the GCN4 coiled coil exhibits a clear sigmoidal curve indicating cooperative thermal unfolding with a characteristic melting point, the curve recorded for the Drebrin-SAH shows a continuous decrease in the measured helicity at higher temperatures, consistent with the behavior of previously investigated SAH segments of M4K4, GCP60 and myosin VI. These data are consistent with a non-cooperative unfolding of the Drebrin-SAH region, indicating that it does not form a coiled coil but rather a stable monomeric helical structure in solution.

	GCP60	M4K4	DrebrinSAH
Residue nr	56	53	74
MRW [g]	134.97	133.36	131.46
C [uM]	19.85	7.64	15
MW [g]	7558.32	7068.08	9728.04
MRE [deg*dmol^{-1}*cm^{2}]	-27506.11	-28754.40	-24904.01
Helicity [%]	67.7	79.2	63.4

Table 2: Helicity values calculated from the CD data of the previously published GCP60 and M4K4 SAH regions as well as the Drebrin-SAH.

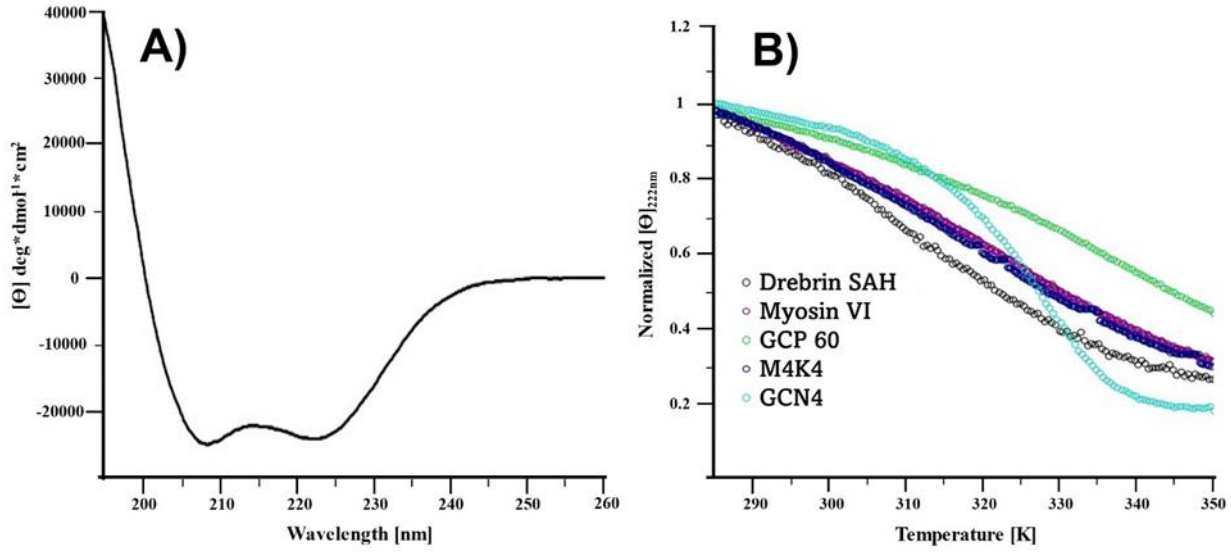

Figure 16: Circular dichroism experiments on Drebin-SAH and other helical proteins.
A, Curve fitting to the experimental CD data of the Drebrin-SAH shows characteristic peaks at 215 and 222 nm indicating alpha-helical structure. B) Temperature denaturation: Mean residual ellipticity at 222 nm normalized to the value measured at 285 K, as a function of temperature (gray circles). Comparison with results obtained for the GCN4 coiled-coil, (cyan), as well as the SAH regions of MYO6 (purple), M4K4 (dark blue) and GCP60 (green).

5.1.2. Drebrin-SAH NMR results

5.1.2.1. Backbone assignment

The high abundance of charged residue repeats and the low complexity of the Drebrin-SAH protein sequence provided an extremely challenging task to perform resonance assignment, as the conventional triple resonance spectra were burdened with severe signal overlap (Figure 17A). The putative single-alpha helical structure carries in itself the parallel alignment of the amide vectors along the transverse axis of the helix resulting in a remarkably low dispersion of the amide NH peaks in the ^{1}H-^{15}N HSQC spectra. Notably, similar spectral crowding was observed for the myosin VIIa SAH (32) domain. Sequential walkthrough was only feasible with the 4D (HACA)N(CA)CONH experiment, which yielded in CO(i)-N(i)-N(i+1)-HN(i+1) correlations making it possible to distinguish between overlapping signals in the ^{15}N and ^{1}H dimensions (109) (Figure 17B). The (H)CC(CO)NH and H(CC)(CO)NH experiments also produced some ambiguity, but starting from anchor residues like I11 [175 in the full UniProt entry Q16643], W17 [181], L26 [190], A35 [199], M47 [211], T61 [225] and I68 [232] was sufficient to unambiguously identify all backbone and most of the sidechain connections. Nuclear Magnetic Resonance data for the Drebrin SAH structural ensemble reported in this article have been deposited at the Biological Magnetic Resonance Data Bank, under deposition ID:52729.

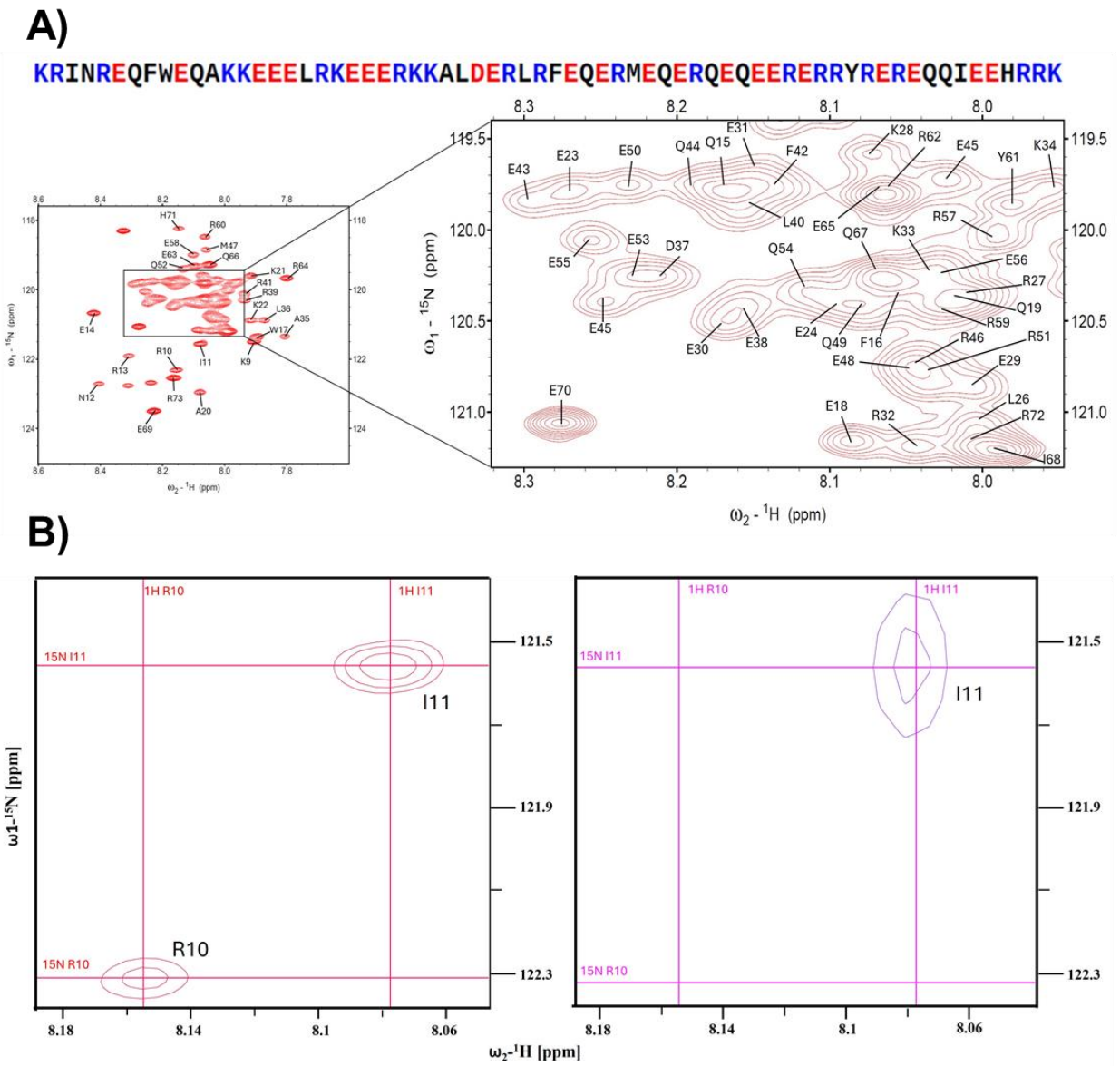

Figure 17: NMR assignment results for Drebrin-SAH.
A) Sequence of the Drebrin-SAH domain. The low complexity and the high amount of charged residues in the protein sequence is highlighted with blue (positive charge) and red (negative charge). The panel displays the ^{1}H-^{15}N HSQC spectrum of the Drebrin Single Alpha Helix in 50 mM NaCl, 17 mM NaH_2PO_4, 3 mM Na_2HPO_4, pH 6.0 at 25 °C. The expansion highlights severely overlapping NH resonances in the central region. The assignments of chemical shifts are shown with one-letter amino acid codes. B) Sequential assignment by walking through the NH signals correlated by the 4D (HACA)N(CA)CONH experiment. Left, ^{1}H-^{15}N HSQC spectrum of the Drebrin Single Alpha Helix in 50 mM NaCl, 17 mM NaH_2PO_4, 3 mM Na_2HPO_4, pH=6.0 at 25 °C showing the position of two following residues. Right, 4D (HACA)N(CA)CONH view of the same spectral width, starting from R10. The complete backbone resonance assignment was obtained with the combinative use of 3D HNCO, iHNCO, HCCCONH and the 4D (HACA)N(CA)CONH experiments using the following strategy: first, COi and COi-1 peaks were picked in iHNCO and HNCO spectra respectively. Then the corresponding NH peaks were accurately picked on the HSQC plane, which otherwise would have been impossible due to the extreme overlap. With these in hand, we could use the 4D (HACA)N(CA)CONH spectrum with dimension order ^{1}H,^{15}N,^{15}N,^{13}C. Assuming the NH and CO peaks are picked correctly, a 4D cross peak observed in the previously described way unambiguously led us to the NH peak of the following residue. The CO correlations were further proven with the HNCO experiments, which in itself was found to be insufficient to correlate with the iHNCO peaks, due to its high degeneracy.

5.1.2.2. *Secondary chemical shift analysis*

To further confirm the high level of helicity in the Drebrin-SAH, secondary Cα and Cβ chemical shifts were determined by subtracting random coil chemical shift values calculated by POTENCI from experimentally observed chemical shift values (74). The resulting profiles clearly supported a predominantly α-helical conformation across the SAH segment (Figure 18). The highest degree of helicity was observed in the central portion of the SAH domain, with a modest decrease toward both the N-terminal and C-terminal ends. This pattern is consistent with previous observations for similar motifs, such as the SAH region of myosin VI (31) It is important to note that these conclusions were drawn using a truncated Drebrin construct. As is often the case with truncated proteins, regions near the artificial termini may display enhanced dynamic behavior or incomplete folding due to the absence of stabilizing sequence context (Figure A1). Therefore, further investigation using an extended Drebrin construct encompassing flanking regions of the SAH domain would be valuable.

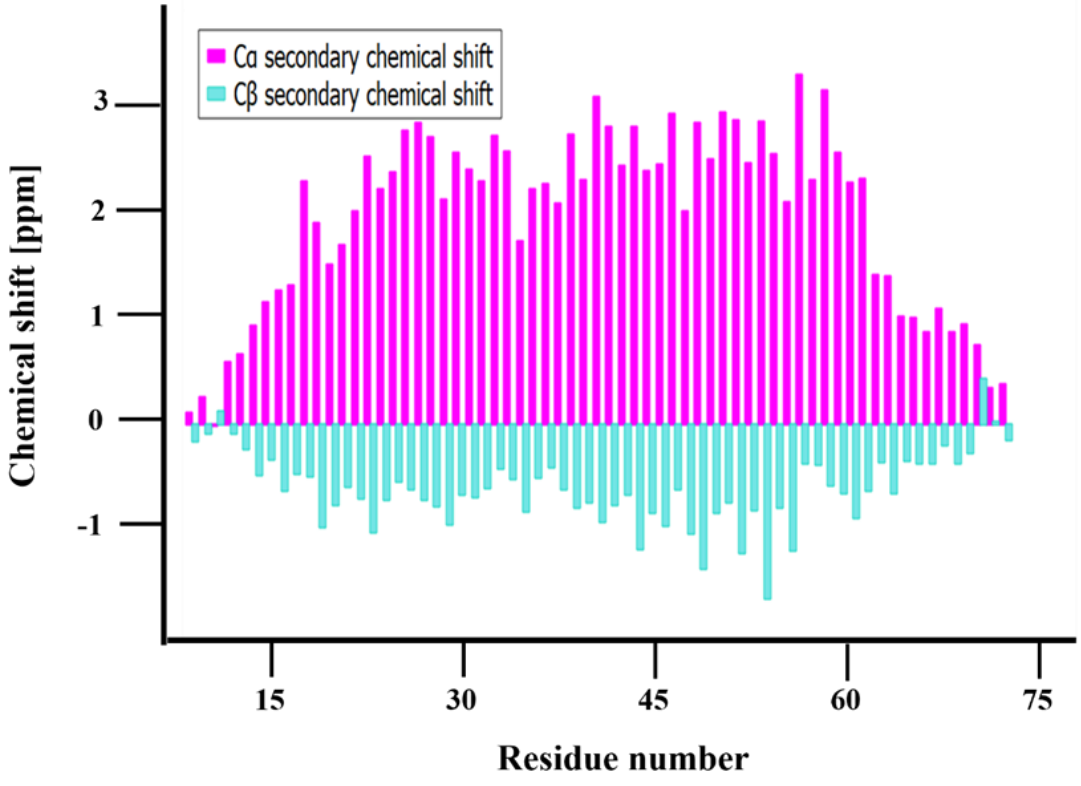

Figure 18: Secondary chemical shifts of Drebrin-SAH.
Magenta columns: secondary Cα chemical shifts, high positive difference from random coil values indicate the local helicity Teal columns: secondary Cβ chemical shifts, the negative difference from random coil values further indicate the local helicity.

5.1.3. Drebrin-SAH SAXS results

5.1.3.1. Small angle X-ray scattering indicates that Drebrin-SAH prefers extended structural states in solution.

The SAXS data, and primary data analysis of Drebrin-SAH measured at three sample concentrations are summarized in Figure 19 and in Table 3. In general, the SAXS profiles (Figure 19A) appear similar, where all three profiles exhibit a relatively featureless monotonic decay in the scattering intensities. Indeed, when the SAXS datasets in Fig. 18A are scaled to protein concentration in mg/mL, and then compared, all three profiles are statistically similar (χ^2= 1.07–1.09; CorMap-P = 0.01–0.02) indicating no discernible concentration-dependent effects on the scattering intensities. The radius of gyration, *Rg*, are consistent across all three samples, spanning 2.9–3.2 nm, as is the concentration independent molecular weight (MW) estimate of 8.5 kDa derived from scattering invariants (Fig 18D and Table 3). The subsequent dimensionless Kratky plots for all three samples (Figure 19B) attest to the extended structural-state hypothesis, where a systematic increase in the transformed intensities are observed as sR_g increases. The dimensionless Kratky plots are absent the typical 'bell-shaped maximum' of a globular protein, or a plateau at increasing sR_g as is often observed for intrinsically disordered proteins (117). The corresponding $p(r)$ profiles (Figure 19C) all yield a highly anisotropic distribution of real-space scattering-pair distances that extend out to a maximum particle dimension, D_{max}, of 12–13.5 nm, which is, once again, considerable for a 10 kDa protein (e.g., compared to BSA (Bovine Serum Albumin) Dmax = 8 nm). However, the $p(r)$ profiles, although highly anisotropic, do not conform to what would be expected for a cross-sectionally thin and stiff-rod type particle that are characterized by a sharp increase in the frequency of scattering-pair distances toward a definable maximum in $p(r)$ at low-r (relating to the rod cross-section) followed by a systematic near-linear decay in $p(r)$ as r approaches D_{max} (136). For example, the $p(r)$ profile calculated from a single-conformation, extended a-helix model of Drebrin-SAH (Figure S3C, inset) retains 'stiff-rod-like' features in the distance distribution that are otherwise less-evident in the $p(r)$ determined from the SAXS data. This suggests that although the Drebrin-SAH prefers to adopt extended states, there may be components of flexibility in the structure that deviate the Drebrin-SAH structure away from a truly stiff rod-like conformation.

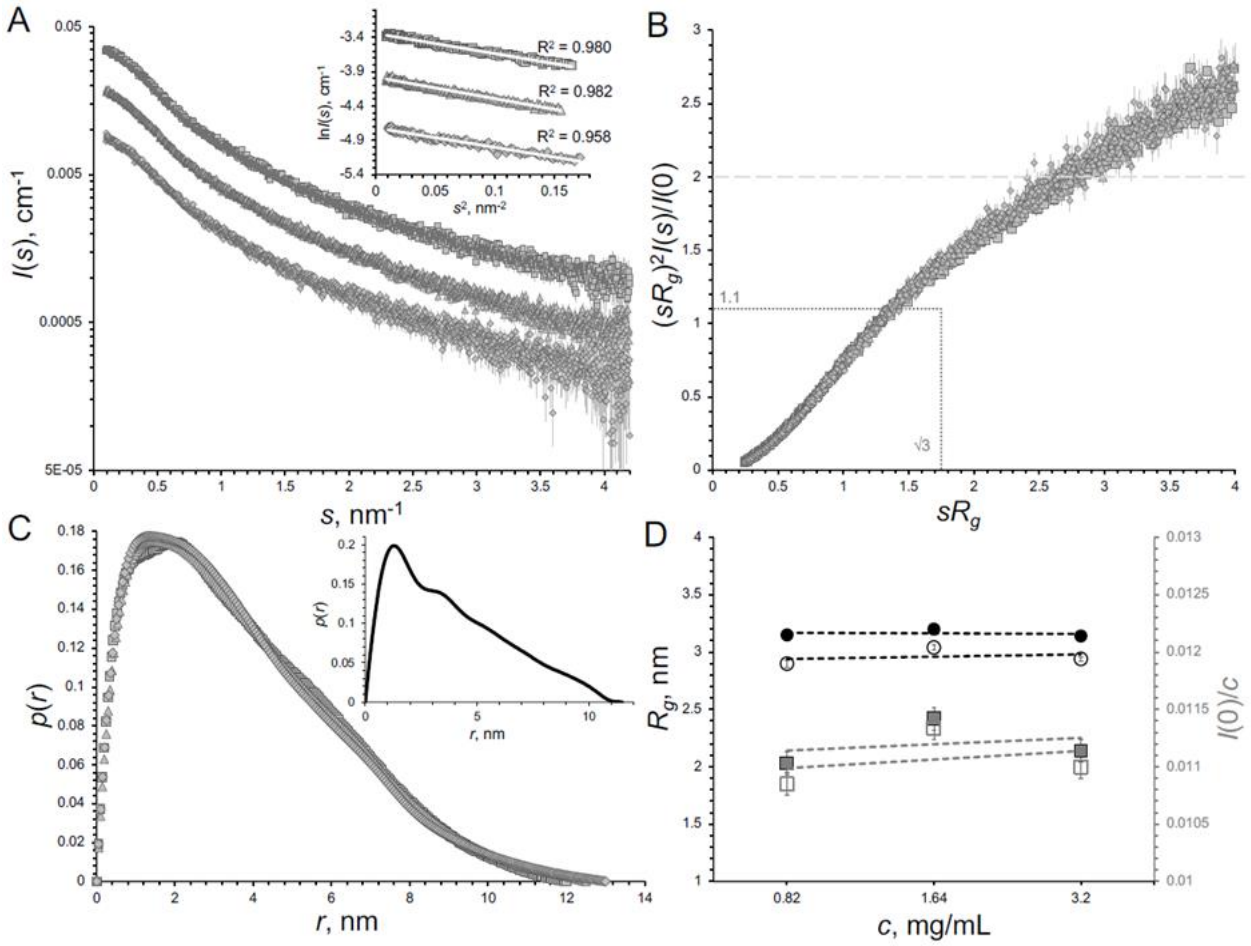

Figure 19: SAXS data and plots for the SAH of Drebrin.
A. **Background-subtracted SAXS data (working s-range) from three sample concentrations of Drebrin. From top to bottom: 3.2 mg/mL (grey squares), 1.64 mg/mL (grey triangles) and 0.84 mg/mL (grey diamonds). Inset: Corresponding Guinier plots and respective linear fits to the Guinier region at very-low angles (~0.28 < sR_g < 1.2). (Table 3) B. Dimensionless Kratky plots for the three SAXS datasets qualitatively demonstrating the extended nature/states of the SAH population in solution (a 'globular maximum' is absent in the transformed scattering intensities at 1.1, √3 and the data do not plateau toward ~2 at higher sR_g, which is otherwise indicative of an intrinsically disordered protein). C. Real-space scattering-pair distance distributions ($p(r)$ profiles, area-normalized to 1) calculated from the SAXS datasets in A showing the highly anisotropic distribution of distances that extend to a Dmax of 12–13.5 nm. Inset: The $p(r)$ calculated from a single-particle model of Drebrin-SAH where the α-helix adopts an extended 'stiff' rod-shaped conformation (model 48 of the NMR ensemble). D. The dependence of the R_g (black) and $I(0)/c$ (grey) as a function of protein concentration, c, demonstrating little-to-no concentration effects on these structural parameters. Closed circles/squares: parameters obtained from $p(r)$; Open circles/squares: parameters determined from the Guinier approximation.**

Sample details

Organism	*Homo sapiens*
Scattering particle composition	
Protein	**Drebrin** – UniProt Q16643 amino acids 172–238 single alpha helix incorporating an additional eight non-native amino acids at the N-terminus (GSHMKDPM) derived from the remnants of a protein affinity tag, post TEV cleavage.
Sample environment	

Solvent composition	17 mM NaH_2PO_4, 3 mM Na_2HPO_4, 50 mM NaCl, pH 6		
Sample temperature	20 °C		
In beam sample cell	1 mm pathlength in-vacuum quartz capillary; continuous flow		
Sample concentration, *c*	0.82 mg/mL	1.64 mg/mL	3.2 mg/mL
SAS data collection			
Data acquisition/reduction software	EMBL bioSAXS *SASFLOW* pipeline(137) ; *BECQUEREL* beam line control software(138) . Batch-mode robot sample delivery.		
Source/instrument description or reference	EMBL P12 bioSAXS beam line(140) equipped with a Pilatus 6M detector (Dectris). Sample-to-detector distance = 3 m. *s*-axis calibrated to silver behenate.		
X-ray wavelength (energy)	λ = 0.123982 nm (10 keV)		
	SAH, 0.82 mg/mL	SAH, 1.64 mg/mL	SAH, 3.2 mg/mL
Measured *s*-range (s_{min}–s_{max} nm^{-1})	0.023–4.43		
Working *s*-range (s_{min}–s_{max} nm^{-1})*	0.095–4.00	0.095–4.07	0.086–4.27
Method for scaling intensities	Absolute scaling relative to the scattering from water, cm^{-1} and normalized to beam transmission		
Exposure time (number of sample frames used for averaging)	0.1 s (101)	0.1 s (77)	0.1 s (20)
SAS-derived structural parameters			
Methods/Software	*PRIMUS* (ATSAS 3.0)(141) including *GNOM 5*(142)		
Guinier Analysis	SAH, 0.82 mg/mL	SAH, 1.64 mg/mL	SAH, 3.2 mg/mL
$I(0)/c \pm \sigma$ ($mL.cm^{-1}.mg^{-1}$)	0.01085 (0.0001)	0.01134 (0.0001)	0.01100 (0.0001)
$R_g \pm \sigma$ (nm)	2.90 (0.03)	3.04 (0.02)	2.94 (0.02)
min < sR_g < *max* limit (data point range) †	0.29–1.20 (28–137)	0.29–1.20 (26–130)	0.28–1.20 (26–134)
Linear fit assessment (Pearson correlation coefficient^2, R^2)	0.958	0.982	0.980
P(r) analysis			
$I(0)/c \pm \sigma$ ($mL.cm^{-1}.mg^{-1}$)	0.01103 (0.0001)	0.01142 (0.0001)	0.01114 (0.0001)
$R_g \pm \sigma$ (nm)	3.15 (0.05)	3.20 (0.02)	3.14 (0.02)
d_{max} (nm)	13.0	12.5	12.0
s-range (nm^{-1})	0.10–4.0	0.124–4.04	0.095–4.18
P(*r*) fit assessment χ^2 (CorMap-*P*)	0.98 (0.485)	1.06 (0.486)	1.01 (0.293)
Scattering particle size			
Methods/Software	ATSAS 3: *DATPOROD*, *DATMW*(143) modules		
Volume estimates	SAH, 0.82 mg/mL	SAH, 1.64 mg/mL	SAH, 3.2 mg/mL
Porod volume, V_p (nm^3)[a]	17.8	18.8	17.9
Molecular weight estimates (kDa)			
Expected MW calculated from amino acid sequence	9.73		

MW from SAXS/*P*(*r*): DatBayes[a] (MW range; > 0.9 confidence)	8.5 (6.6–16.5)	8.5 (6.6–9.1)	8.5 (6.6–9.1)
From SAS-independent method: MALLS/RI (± σ)	-	-	10.985 (0.024)
MW ratio (MALLS/expected)	-	-	1.13
RI dn/dc value (*SEDFIT*)(121)			0.1931 mL/g
***Ab initio* bead modelling**			
Methods/Software	Dummy-atom shape/volume reconstruction using *DAMMIF*(144)/*DAMMIN*(145)		
Dataset used for shape reconstruction	SAH, 3.2 mg/mL, *GNOM 5* input.		
s-range for individual model building (s_{min}–s_{max} nm^{-1})	0.095–4.18		
Symmetry	P1		
# of individual model reconstructions	10 *DAMMIF* models, fast-mode, spatially aligned with *DAMSEL*, *DAMSUP*, *DAMAVER*(146) (normalized spatial discrepancy across the model cohort = 0.939). DAMSTART output used as input into *DAMMIN*.		
Model fit χ^2 (CorMap-*P*)	0.992 (0.259) (evaluated across the *s*-range 0.095–3.64 nm^{-1})		
Data and model deposition SASBDB accession code: SASDVV6			

Table 3: SAXS Reporting Table: Extended single alpha helix (SAH) of Drebrin.
The working *s*-range was determined using a combination of AUTORG16 (s_{min}) and SHANUM17 (s_{max}). Point range refers to the data points of the measured SAXS profiles of each dataset (not the working s-range); refer to the SASBDB entry SASDVV6 for the SAXS profiles measured across the full s-range at each sample concentration. aPorod volume and concentration-independent MW estimates from the SAXS data were calculated using the corresponding GNOM.out files as input into DATPOROD and DATMW, respectively.

5.1.3.2. Molecular weight measurements

The MW estimate from SAXS was additionally validated using SEC-MALLS/RI measurements from the same Drebrin-SAH sample, yielding a MW average of 11 kDa (Table 3; Figure 20). Combined, the MW results demonstrate that the Drebrin-SAH is monomeric under the sample conditions used for SAXS which are identical to the sample conditions used for NMR. This has been further validated as the protein mass from the MS experiment was calculated to be 9727.0 Da, with 0.75 Da difference from the expected 9727.75 Da. The difference can be attributed to the accuracy of the MALS-SEC method, which is one magnitude less than the Q-TOF MS, however, the oligomeric state could still be reliably assessed. Both methods clearly indicate that the region is monomeric under the conditions used. Of note, the Rg of the Drebrin-SAH monomer is comparatively large for a ~10 kDa protein (Table 4). For example, the R_g of bovine serum albumin (BSA) – a much larger 66 kDa globular protein (SASBDB ID: SASDFQ8) – is 2.8 nm, which is smaller than the R_g of the Drebrin-SAH. This simple 'R_g -to-MW' comparison suggests that

the mass distribution of Drebrin-SAH is not evenly distributed in all directions around the centre of mass but is rather distributed toward structurally extended mass/volume-states.

	BSA	α-synuclein	Drebrin-SAH
MW [g]	66	14.4	9.7
R_g [nm]	2.8	3.5	2.95
D_{max}	3	1.72	1.36

Table 4: R_g, D_{max} and MW comparison of Drebrin-SAH with globular and disordered proteins. The SAXS results from Drebrin-SAH support the hypothesis of an extended molecule with limited allowance for local flexibility.

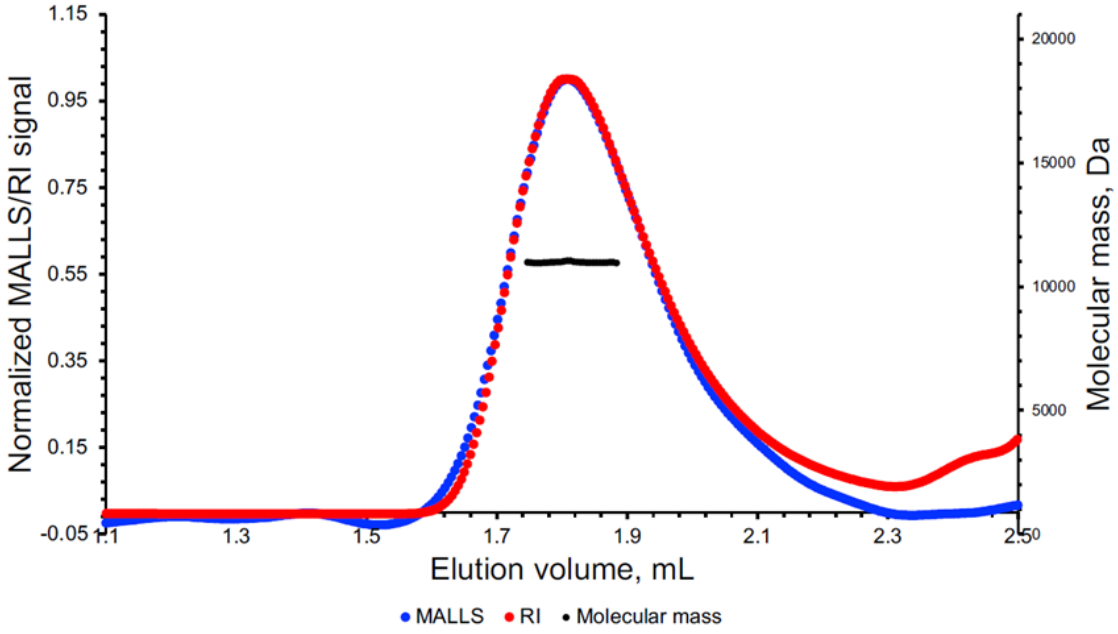

Figure 20: Size exclusion chromatography (SEC) MALLS/RI analysis of Drebrin-SAH. Multi-angle laser light scattering trace (MALLS, Rayleigh ratio, blue) and differential refractive index (dRI, red) SEC-elution profiles with the associated calculated experimental molecular mass estimates/correlation through the SEC peak (~11 kDa) demonstrating that the SAH is a monomer in solution (expected molecular mass, monomer = 9.7 kDa).

5.1.3.3. Scattering decay analysis

An analysis of the decay in the scattering intensities in the mid-s region of the scattering data (~0.55–2.0 nm^{-1}) was performed to evaluate the mass-fractal scaling relationships of the Drebrin-SAH samples. In the larger-angle region of the scattering profile, the relationship between $I(s)$ and s maybe generalized as:

$$I(s) \propto s^{-Dm}$$

where *Dm* is the mass-fractal dimension of the particles (146). The *Dm* encodes information relating to the interatomic distances on different length scales internal to a molecule, in effect describing the scaling relationship between the mass enclosed by the particle volume and its linear dimensions (shape-characteristics). This parameter is determined from the negative slope of the decay in the scattering intensities in the intermediate-angle region of the scattering profile when the data are plotted as Log$I(s)$ vs Log(s) (Figure 21A). The *Dm* is, in turn, related to the Flory exponent, υ (where $\upsilon = 1/ Dm$) that describes the relationship between the R_g of a polymer and the number of monomer units – in this case amino acids – comprising the chain length (117,148). For globular/compact particles/solids the *Dm* ranges from 3–4 ($\upsilon \approx 0.25–0.33$); for a flat planar 'disc' like object, *Dm* is 2 ($\upsilon \approx 0.5$); for a self-crossing random-walk chain, the *Dm* is also 2 ($\upsilon \approx 0.5$), while for a well-solvated swollen chain or intrinsically disordered protein, the *Dm* is around 1.7–1.8 ($\upsilon \approx 0.55$-0.59) and; for stiff highly-extended rod-like particles the *Dm* is even lower, approaching ~1 ($\upsilon \approx 1$). For the Drebrin-SAH samples, the *Dm* is ~1.36 ($\upsilon = 0.73–0.74$; Figure 21A) which is a too-shallow decay in the scattering intensity for the scaling relationship to be categorized as highly-flexible/disordered, and too large to be considered as a purely stiff and rod-like. What the *Dm* analysis suggests, when combined with the R_g observations, dimensionless Kratky plot, $p(r)$ and D_{max} descriptions, is that the Drebrin-SAH is present in solution as a set of structures that have a likely preference toward sampling extended conformations and that there is an allowance for limited bending/flexibility in these states, as opposed to adopting a well-defined single stiff rod-like extended structure. Subsequent *ab initio* bead-modelling, and the spatial alignment of the globally restored shape derived from SAXS with the conformational ensemble of alpha-helical variants determined from NMR (Figure 21B) are entirely consistent with the extended, multi-state conformational sampling of Drebrin-SAH in solution.

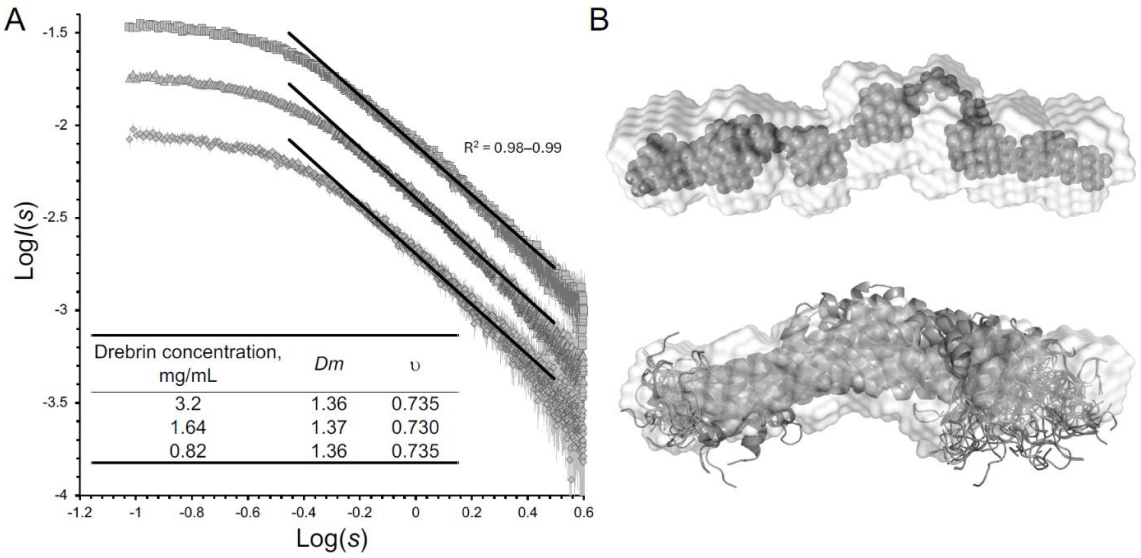

Figure 21: A Log-Log scale representation of the SAXS data measured from Drebrin-SAH.
(top to bottom: 3.2 mg/mL (grey squares), 1.64 mg/mL (grey triangles) and 0.84 mg/mL (grey diamonds)), with corresponding estimates of the decay in the scattering intensities determined from the linear slope of Log*I*(s) vs Log(*s*) across the mid-s region of each profile (~0.55–2.0 nm-1; black lines). The mass fractal dimension, *Dm*, and corresponding estimate of the Flory exponent (υ, where υ ~ 1/*Dm*) are consistent with the scaling behavior of extended, but not stiff/linear rod-like particles. B. Top: Examples of the shape of SAH reconstructed from the 3.2 mg/mL SAXS data profile showing the anisotropic/extended distribution of mass (volume occupancy) of an individual bead model (grey spheres) aligned into to the envelope generated from the minimized spatial alignment of a 10-model cohort (white surface). Bottom: A spatial alignment and comparison between the Drebrin-SAH model-ensemble (grey ribbons) derived from NMR and the overall shape of a spatially-aligned dummy-atom 10-model cohort reconstructed from the 3.2 mg/mL SAXS dataset (white surface).

5.1.4. Drebrin-SAH computational results

5.1.4.1. Structural ensembles of the Drebrin-SAH region reveal an extended yet dynamic helix

We have generated an initial pool of 30,000 structures with regionally adjusted, high helicity (Figure 13) using DIPEND (33) and GROMACS (123) (*vide infra* 4.1.5 Drebrin-SAH conformer generation and selection). After randomly choosing 5,000 structures, we have selected subsets from these based on their correspondence to Cα / Cβ chemical shifts and the measured SAXS curve. After repeating these steps five times, we generated a secondary pool from the models included in any of the selections and subjecting each of them to a 20 ns molecular dynamics run with the backbone coordinates fixed. The final ensemble was selected from this secondary pool for correspondence with the Cα / Cβ chemical shifts and the measured SAXS curve (Figure 14). To assess the ensembles generated at each step, additional evaluations and selections were performed (Figure 22A, B).

Acceptable χ^2 values for the SAXS fit could only be obtained for ensembles explicitly selected for correspondence with the SAXS data. Our analysis of the radius of gyration (*Rg*) and end-to-end distance reveals that SAXS data favors more extended structures than chemical shifts alone. Selection only for chemical shifts improves the SAXS fit slightly but not beyond the acceptance limit, whereas selection only for SAXS data renders the correspondence with the chemical shifts even worse than that of the initial pool. This observation justifies the simultaneous use of both data types to obtain conformers that reflect both the local structure governed by the chemical shifts and the overall shape reported by the SAXS measurements. Such ensembles exhibit only slightly worse fitting to these data than the best ones selected for only one of the data types (Figure 22A, B). Hα chemical shifts, not used in any of the selection, behave similarly to Cα / Cβ shifts in terms of improvement, consistent with the fact that they are mostly sensitive to local conformation similar to Cα shifts (148). The selections were performed to minimize the RMSD between the experimental and back-calculated chemical shifts. RMSD is independent of the use of primary or secondary chemical shifts. In contrast, the correlation between calculated and experimental secondary shifts is a much more sensitive measure than using primary chemical shifts. The high correlation for sequence-corrected secondary chemical shifts indicated that the trends in local structural preferences are reproduced acceptably.

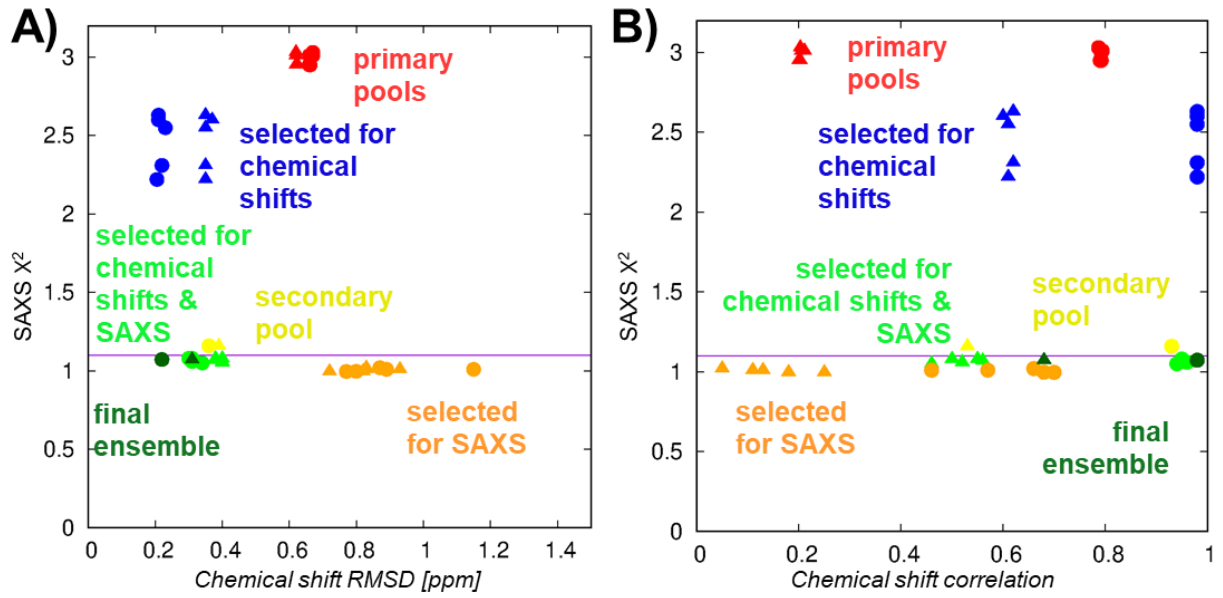

Figure 22: Correspondence of the different ensembles to experimental data.
A) and B) correspondence to SAXS and chemical shift data using RMSD and correlation for secondary chemical shifts (RMSD is the same for primary and secondary shifts). Filled circles represent Cα and filled triangles Cβ chemical shifts

The *Rg* of the conformers selected for SAXS data either alone or in combination with chemical shifts is in fairly good agreement with the value of 2.9 nm estimated directly based on the SAXS measurements.

End-to-end distance between the Cα atoms of the first and last residues suggests that the construct does not adopt an entirely straight helical structure but still prefers a largely extended conformation (Figure 23A, B).

The final ensemble consists of 60 conformers and exhibits very good correspondence both with the SAXS (Figure 23C) and chemical shift data (Figure 23D), thus, it is expected that the ensemble adequately reproduces both the local and global structural features of the Drebrin-SAH region. Of course, the limited number of conformers is not expected to represent all aspects of the actual structural diversity in the SAH region, but arguably our selection procedure largely reduces the possibility of overfitting, and hence provides a conservative ensemble-based representation.

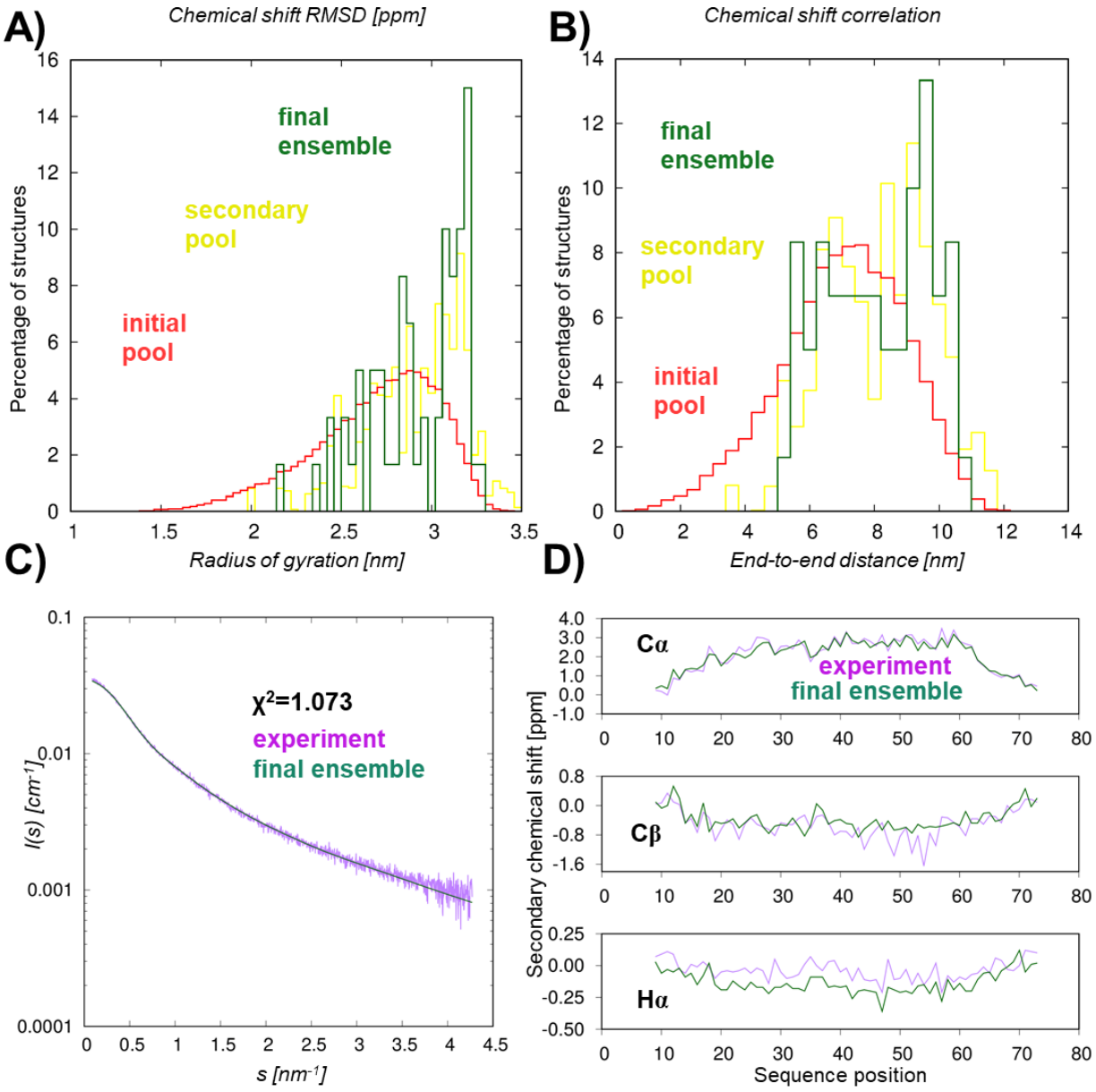

Figure 23: End-to-end distances and Rg values of the different subensembles showing preference of extended conformations.
A) Distribution of the radius of gyration and B) end-to-end distance in conformers of the initial pool, the secondary pool and the final ensemble. C) Comparison of the experimental SAXS curve with the one back-calculated for the final ensemble. D) Comparison of experimental secondary chemical shifts with those estimated for the final ensemble. The lines connecting the points are shown for better visualization of the trends.

PCA (Principal component analysis) of the selected conformers with respect to the conformational diversity of the initial pool reinforces this conclusion, i.e. the different selections sample only well-defined regions represented by the 1st and 3rd principal components. The 1st PC largely describes the compact/extended nature of the molecule, whereas the 3rd PC corresponds to a bending motion (Figure 24). Thus, the inclusion of arbitrary non-native conformers that might improve the correspondence to experimental data randomly by simply enhancing the diversity of the ensemble is expected to be negligible.

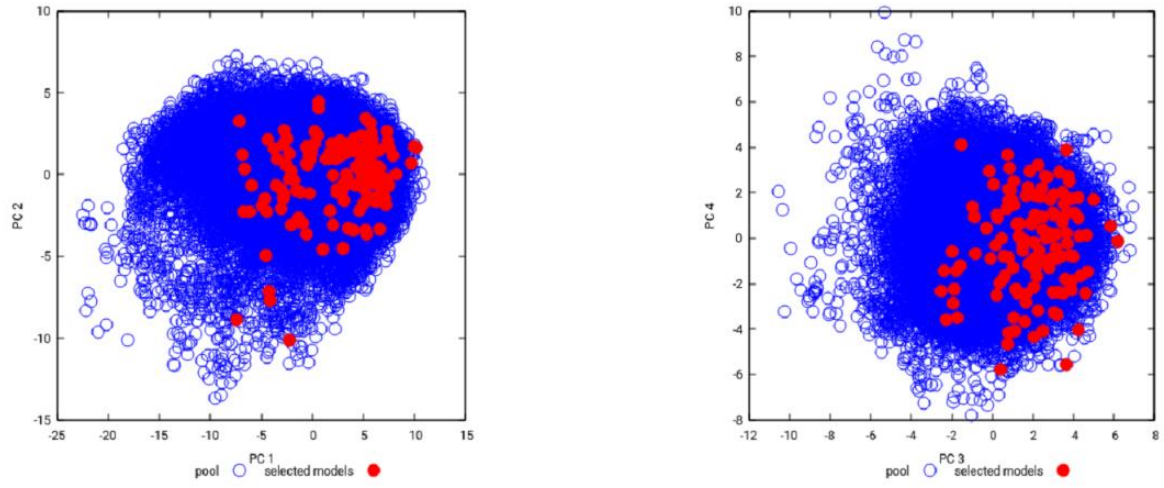

Figure 24: Principal component analysis of the initial pool with the models selected from the primary pools highlighted.
The selected conformers do not sample the full extent of the PC1 and PC3 coordinates, indicating clear structural preferences for the selected ensembles.

5.1.4.2. DSSP analysis

DSSPcont analysis, assigning the probabilities of secondary structure states to each residue, reveal strong helical propensity of the central region of the helix in the final ensemble (Figure 25A). The region between residues 26-59 [190-223] can be characterized with a high probability of alpha-helical state, with segments 26-31 [190-195] and 38-59 [202-223] with least 90%, including the region 49-52 [213-216] with an assigned 100% of state 'H'. The N-terminal part, remaining from the expression tag, is largely disordered. Even when considering this, the helicity is decreasing from the central part towards the terminal

regions in an asymmetric manner, with a steeper transition towards the C-terminus (Figure 25B). The structures themselves show two kinds of deviations from a straight helix: the terminal regions are unfolded, whereas in the central regions there are occasional "kinks" of the helix (Figure 25C). The structural ensemble has been deposited to PED with the ID PED00524.

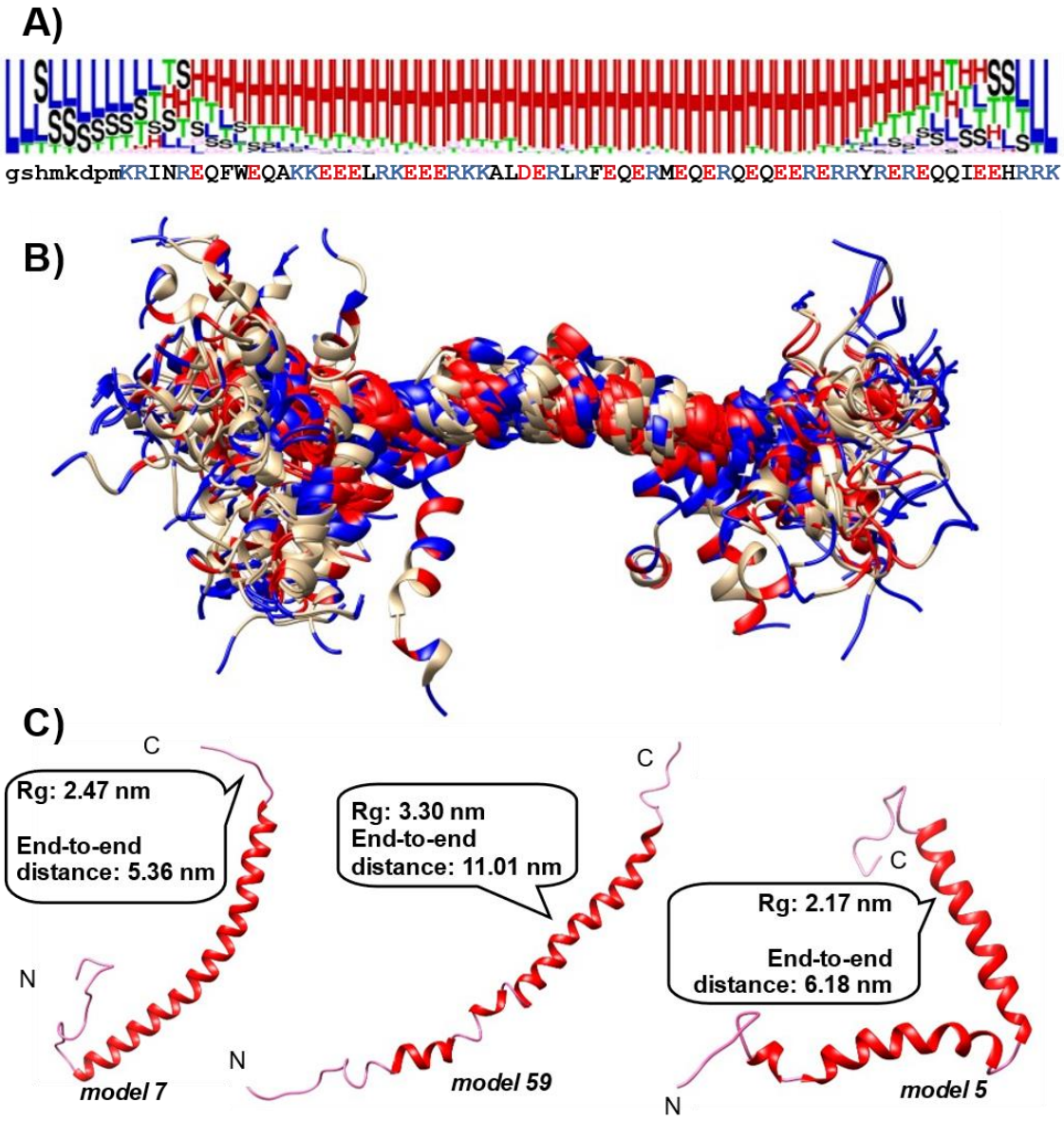

Figure 25: Overall structure of the Drebrin-SAH region.
A) Secondary structure logo of the Drebrin-SAH region reflecting the secondary structure state probabilities obtained via DSSPcont. The sequence of the construct is shown below the logo. B) Ribbon representation of the final selected ensemble of 60 conformers for the Drebrin-SAH region. For clarity, the first 8 residues, corresponding to the expression tag, are not shown. Conformers have been superimposed over residues 26-59 [190-223] with high helicity. Positively charged residues are colored blue, negatively charged red. C) Conformers of the final ensemble with the lowest end-to-end distance (model 7), lowest radius of gyration (model 5) and the model for which both these are the largest (model 59).

5.1.4.3. *Interactions between charged residues are highly dynamic.*

As expected, being a signature of the SAH structural motif, oppositely charged residues on the same face of the helix can form ionic interactions with each other. The secondary pool, from which the final ensembles were selected, was generated to sample possible side chain conformations. In accordance, the final ensemble reveals diverse interactions between charged residues, even for conformers having virtually identical backbone conformations. However, owing to our selection methodology (*vide supra* 4.1.5 Drebrin-SAH conformer generation and selection), the 60-member ensemble cannot be regarded as reflecting any thermodynamic equilibrium or being large enough to sample all possible interactions that might be relevant. Rather, it can be used to indicate several structural features that might actually occur without being incompatible with the experimental data used. In principle, regarding the full ensemble, almost none of the charged residues forms an interaction solely with one specific, oppositely charged partner. Hence, each Asp/Glu can establish salt bridges with more than one Lys/Arg and vice versa. The sole exception is Arg39 [203], only forming an ion pair with Glu43 [207], but potentially participating in a cation-π interaction with Phe42 [206] in several conformers. A typical pattern is that residues can interact with partners in both directions, i.e. the partner is located either towards the N- or the C-terminus. The most regular pattern, dominated by i-i+3 and i-i+4 salt bridges, is observed for the highly helical region between residues 39-59 [203-223] (Figure 26A). Salt bridges between residues at different distances along the sequence (e.g., Glu30 [194]-Arg41 [205] in model 5, shown in Figure 26C) typically indicate non helical local conformation in the given structures. From the two charged residues located in the expression tag, Lys5 only forms occasional interactions with Asp6, whereas Asp6 can form salt bridges with multiple residues in the SAH region, mostly conforming to the i-i+3 or the i-i+4 pattern.

Closer inspection reveals that there are instances of residues simultaneously interacting with two oppositely charged residues (Figure 26B). There are cases where one residue is “sandwiched” between two oppositely charged partners, one at each side, similar to arrangements described previously based on molecular dynamics studies. However, for example, Arg51 [215] can make simultaneous interactions with two glutamates located in C-terminal direction along the helix .Although our 60-membered ensemble does not necessarily sample all possible interactions that occur in the region, this remarkable diversity even on this relatively small sample strongly suggests highly dynamic side-chain rearrangements, consistent with earlier suggestions and observations. In our ensemble, the occurrence of salt bridges with the orientation having the negatively charged residue towards the N-terminus is slightly more common than the opposite direction, at odds with the conclusions obtained on model peptides combined with an analysis of PDB structures (150). The reason of this apparent discrepancy might be that our sampling of conformations and

interactions is far from exhausting, and also that the previous study focused on Lys→Glu and Glu→Lys pairs in their model peptides, whereas most of the salt bridges in Drebrin-SAH involve Arg residues, especially in the region with the highest helicity, located in the C-terminal half. In our relatively small sample of conformers, lysine side chains seem to behave similarly to those of arginines in terms of being able to form interactions with multiple partners, thus, we observe no hints of different dynamics of salt bridges involving Lys and Arg residues as observed in molecular dynamics simulations.

5.1.4.4. Aromatic-aromatic and cation-π interactions in the Drebrin-SAH region.

The most remarkable sequence feature of the Drebrin-SAH is the presence of a Phe-Trp residue pair near its N-terminal part, located within the motif 14EQFWEQ19 [178-183]. The Phe and Trp residues are assigned 60 and 74% 'H' state in the final ensemble, respectively, thus, although far from being among the residues with the highest helical character, they are clearly part of the SAH structure. Analysis of the conformations generated reveal that the two aromatic rings can form edge-to-face interactions where one edge of the phenyl ring is within 0.5 nm of the indole ring plane, as can be expected for consecutive aromatic residues in an alpha-helix (150).

A systematic analysis of the atomic distances between the aromatic rings of Trp, Phe, Tyr residues and the charged groups of Arg and Lys side chains, a number of putative cation-π interactions have been revealed (Figure 26C). Although our conformational ensemble can not be expected to sample all possible such contacts and cation-π interactions can vary greatly in strength, the estimation of which would require quantum chemical analysis, our observations suggest that basically all aromatic residues can form such interactions with multiple partners. Notably, the indole ring of Trp17 [181] can be close to the amino group of Lys21 [185] or the guanidino groups of Arg10 [174] or Arg13 [177] .The i-i+4 spacing of Trp17 [181] and Lys21 [185], as well as their aromatic → cationic order is consistent with a weak stabilizing interaction observed in some helical model peptides (151). However, this region adopts non helical conformations in a remarkable number of the selected structures, some of these are still compatible with the presence of the cation-π interaction with one of the preceding arginine residues. In addition, Phe16 [180] can interact with Lys9 [173], or Arg13 [177], and even Lys5 from the remaining linker, the latter two of which can also pair with Trp17 [181] (Figure A2). Phe42 [206] can form cation-π interactions with Arg39 [203], Arg41 [205] or Arg46 [210], and Tyr61 [225] with Arg57 [221], Arg60 [224], Arg62 [226] or Arg64 [228]. Regarding residue spacing, the most common pattern observed is the i-i+3 and i-i+4 interactions, compatible with the helical nature of the region. Interestingly, Phe42 [206] is the only aromatics where interaction with the neighboring residue Arg41 [205] might occur. Analysis of the potentially interacting pairs reveals that these do not disturb the helical structure, compatible with the high helicity of both Arg41 [205] and Phe42 [206] (96 and 92%, respectively). In these structures, the orientation of the aromatic plane is parallel with the

helix axis rather than the perpendicular one more common in pairs with larger interresidue distances. As in the largely extended SAH region practically all residues are solvent-exposed, all cation-π interactions can be regarded as occurring on the molecular surface, consistent with earlier suggestions (134). The overall prevalence of potential cation-π interactions prompts us to suggest that, to some extent, compete with the classical ion pairs, and thus the aromatic side-chains act as additional transient interaction partners for nearby positively charged side chains, essentially being a part of the dynamically reorganizing pattern.

In the largely helical structure of the Drebrin-SAH region, all aromatic sidechains are largely exposed, the most exposed being Phe16 [180] of the FW motif, leading to the straightforward suggestion that these residues might be important recognition sites for intermolecular interactions (Figure A2). However, the cation-π interactions described above might contribute to the partial shielding of aromatic rings, rendering them less exposed to the solvent in the monomeric SAH.

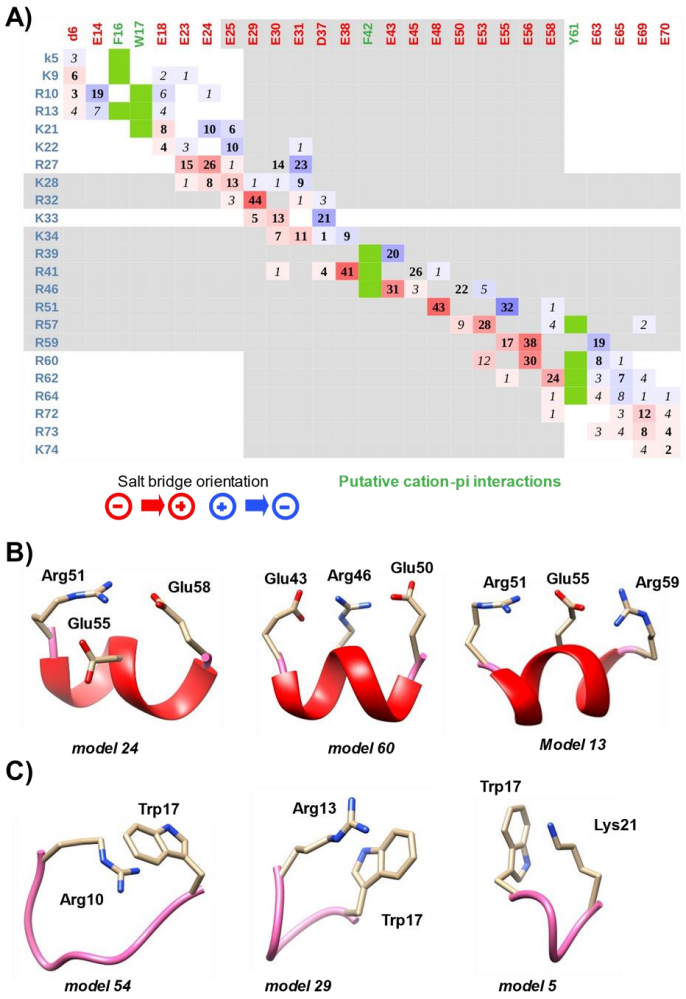

Figure 26: Residue-residue interactions in the Drebrin-SAH region.
A) occurrences of ion pairs between charged residues and putative cation-π interactions in the ensemble. The numbers represent the times a given ion pair was observed. Due to simultaneous ion pair formations, one residue can participate in more than 60 pairs in the ensemble of 60 conformers. Interactions where the Asp/Glu reside is closer to the N-terminus are colored red, opposite orientations are colored blue. i-i+3 and i-i+4 salt bridges are shown with bold numbers, other salt bridges in italics. Residues in segments over 85% helicity according to DSSPcont are shown in gray background. Putative cation-π interactions between aromatic and positively charged residues are shown with green boxes. B) examples of simultaneous salt bridges in selected conformers. C) Examples of cation-π interactions between Trp17 [181] and positively charged residues in selected conformers

5.1.4.5. Structure, dynamics and unique features of the Drebrin-SAH region

Simultaneous consideration of global (as revealed by SAXS) and local (as reported by NMR chemical shifts) structural features is indispensable to obtain structural ensembles of single alpha-helical regions that reflect their actual dynamics and the extent of their deviations from a straight helical conformation. Apart from the disordered N-terminal residues originating from the expression tag, the

dynamical features of the actual SAH region are clearly deducible from both the NMR and SAXS results. Ensemble-based modeling suggests that the Drebrin-SAH forms a stable helical structure with moderate but non-negligible deviations from a fully extended helix. Analysis of side-chain interactions reveals a continuous dynamic reorganization of ion pairs, and the presence of interactions distinct from the expected i-i+3 and i-i+4 patterns, presumably contributing to the emergence and transient stabilization of nonhelical local structures. We propose that the aromatic residues, characteristic of the Drebrin-SAH, take part in this dynamic interaction network by forming various cation-π, and, in the case of the Phe16 [180]-Trp17 [181] pair, aromatic-aromatic interactions. The specific Phe-Trp sequence motif along with Phe42 [206] and Tyr61 [225] might provide a docking site for potential interacting partners where they can form competing intra- and intermolecular interactions.

The non-uniform structural and dynamical features along the Drebrin-SAH region seem to be dictated by the local sequence, i.e. the presence of aromatic residues and the characteristically different Arg/Lys ratio in the N- and C-terminal halves of the helix. This view is supported by the highly conserved nature of the SAH in Drebrin orthologs (Table A6) which is somewhat surprising in such a low complexity region where the major direction of evolutionary pressure could be expected to maintain the overall helical structure. The high conservation of the aromatic residues, together with their location on one side of the helix, reinforces their role as potential interaction sites and also their participation in specific stabilizing interactions.

Compared to the thoroughly characterized Myosin 6 and Myosin VIIa SAHs, the abundance of aromatic residues is a quite unique feature in Drebrin-SAH. The Myosin 6 SAH does not contain a natural aromatic residue, whereas the Myosin VII SAH contains mainly histidines beside a single Tyr. Histidine residues can participate in multiple different interactions with positively charged Arg side chains (152), of which the H-bonding interaction is calculated to be the strongest one. In the available Myosin VIIa SAH X-ray structure (5WST), only His897 is in the central region of the helix, and it does not interact with any nearby positively charged residue, although its potential interaction with Arg900 can not be excluded. The other two aromatic residues, His and Tyr, have no assigned coordinates in the construct, but are located very close to the termini, unlikely to contribute to the stabilization of the helix.

A survey of SAHs in UniProt suggests that although aromatic residues are not uncommon in predicted SAH domains, and even consecutive aromatic residues can occur, the FW motif is specific for the SAH in Drebrin and the related Drebrin-like protein (Uniprot ID for the human ortholog: Q9UJU6). This suggests that the presence of aromatic side chains is not only compatible with the stable single-helical structure but might be an important functional feature. Further investigation of SAH sequences with different amino acid composition is needed to uncover the exact role of these residues.

5.2 Drebrin D233 results

5.2.1. Drebrin D233 CD spectroscopy results

Initial secondary structural characterization of the Drebrin D233 construct has been done with similar circular dichroism experiments, as the first attempts to confirm the high helical content of Drebrin-SAH. As prior to my studies, this was the only available structural information from the actin-binding region of Drebrin, it served as an important benchmark to compare the CD spectra of my prepared construct with the one published by Grintsevitch and colleagues (Figure 27).

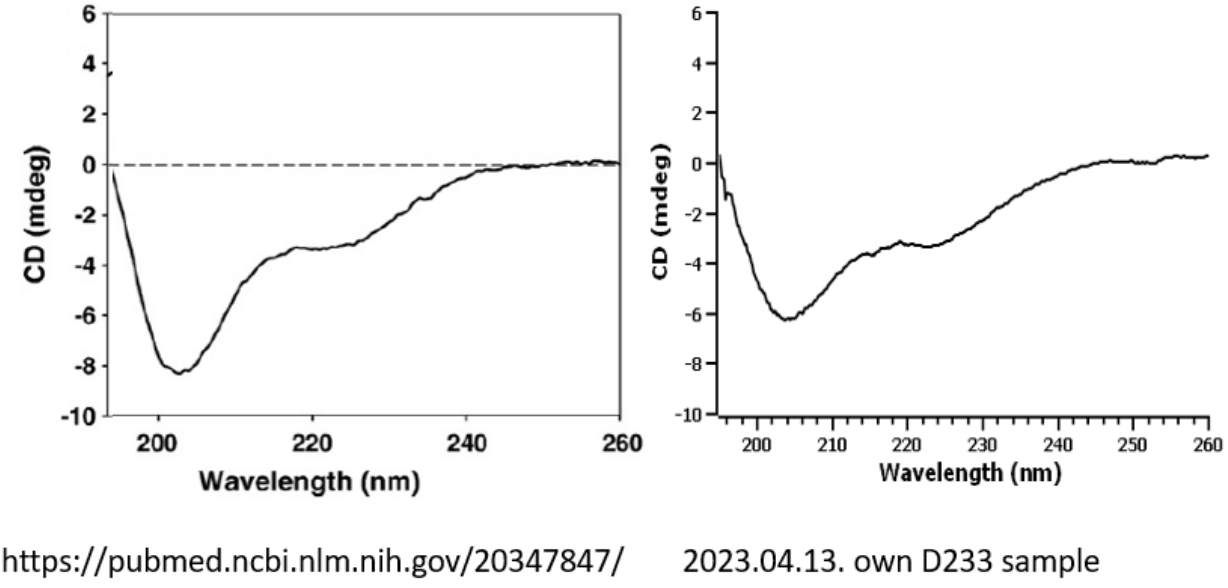

Figure 27: Comparison of CD curve fitting to published and obtained data from the actin-binding core in Drebrin. Left: Figure published by Grintsevitch and colleagues (24)**, right: CD curve recorded from D233 sample.**

The shape of the CD curve recorded from D233 sample is statistically similar to the one from Grintsevitch and colleagues, confirming the successful cloning and expression of the desired segment. BestSel secondary structure content calculation from the CD data resulted in 0.5 % helix, 38.3 % antiparallel, 0.0 % parallel, 16.2 % turn and 45 % others. These results strengthened the hypothesis that the protein is dominantly disordered, however the determined high amount of β-sheet was rather unexpected. Nevertheless, the results of CD spectroscopy experiments turned out to be good enough validation of the prepared protein construct and confirmed the need of a more detailed structural characterization of the ABD in Drebrin.

5.2.2. Drebrin D233 Pull-down assay results

The pull-down assay protocol designed in-house for the screening of protein-protein interactions with a His-tagged construct was tested to evaluate if the binding of F-actin by D233 can be detected (Figure 28).

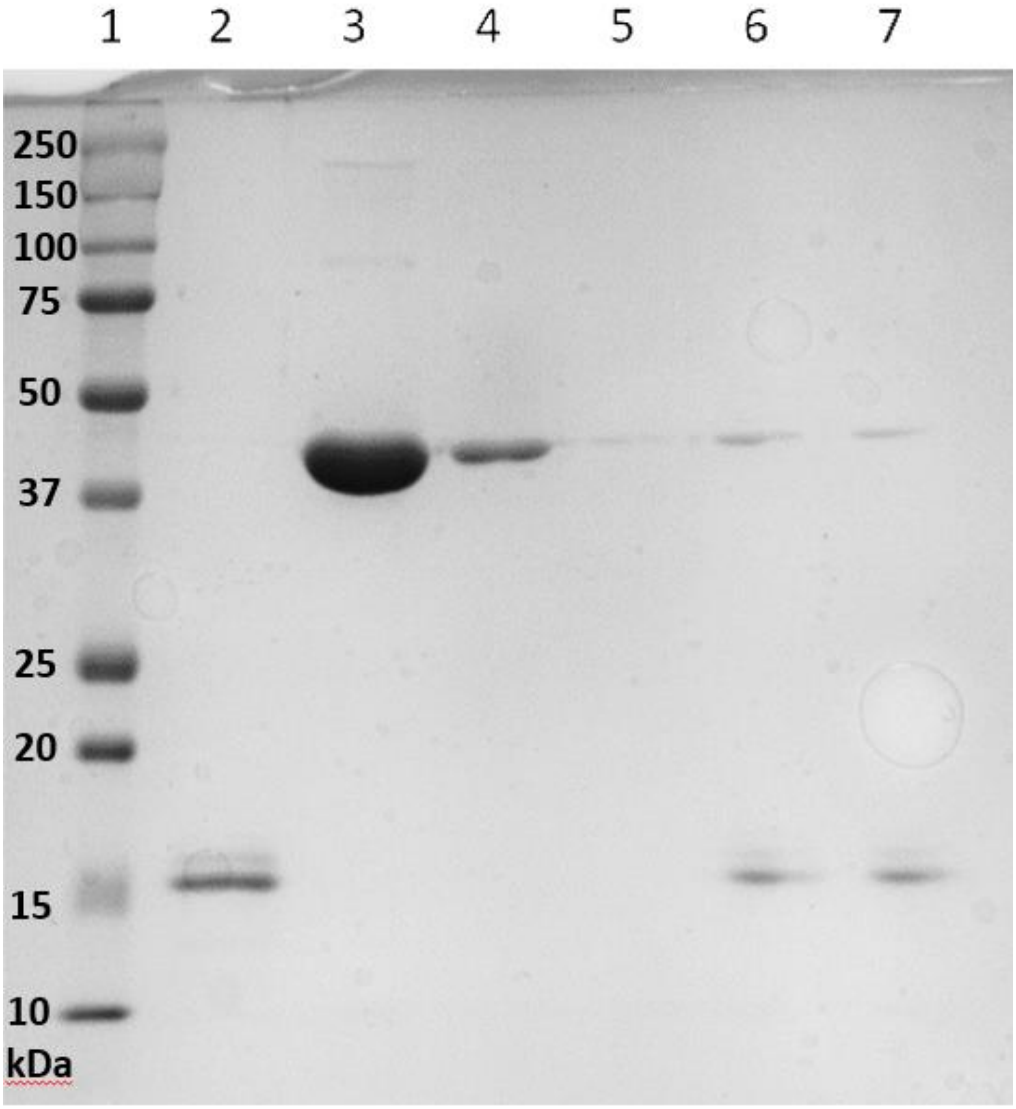

Figure 28: SDS-PAGE results from the Drebrin-actin pull-down assay.
1: MW2: D233 input (10 uM)3: F-actin input (10 uM)4: F-actin input (5 uM)5: negative control elution: 10 uM F-actin elution7: 5 uM F-actin elution

The results indicate that the stoichiometry of the Drebrin-Actin interaction is far from equivalent, as seemingly the same amount of D233 could bind the same, very low amount from 10 and 5 micromolar F-Actin input samples as well. This further suggests that on the surface of each actin filaments there might be several Drebrin-binding sites after polymerization, thereby shifting the stoichiometry. The amount of F-

actin found in the elution fractions is rather low, which can have several reasons. Primarily, biophysical assays relying on immobilization may not fully capture the behavior of disordered proteins, especially if a transient interaction is hypothesized. Mechanistical properties of the large actin filaments makes these methods even more difficult. Considering these factors, I concluded that the D233 construct is feasible for the investigation of Actin-binding, however a more systematic analysis of carefully designed experiments, which are more sensible to these types of interactions is required.

5.2.3. Drebrin D233 NMR assignment results

The results of the backbone assignment can be considered complete (Figure 29,30). From the 85 amino acids, 81 have been assigned unambiguously. The amide backbone chemical shifts of the four proline residues are missing due to the lack of HN protons. Aliphatic ^{13}C side chain resonances have been also included in the deposition. Cβ chemical shifts of prolines all appear close to 32 ppm suggesting the presence of trans isomers. The aliphatic carbon chemical shifts were used to derive secondary structure propensities with CheSPI (77), and compared with the predicted propensities by ODiNpred (153), based on amino acid sequence alone (Figure 31). The assignments obtained for D233 have been deposited in the BMRB with the access number 52895.

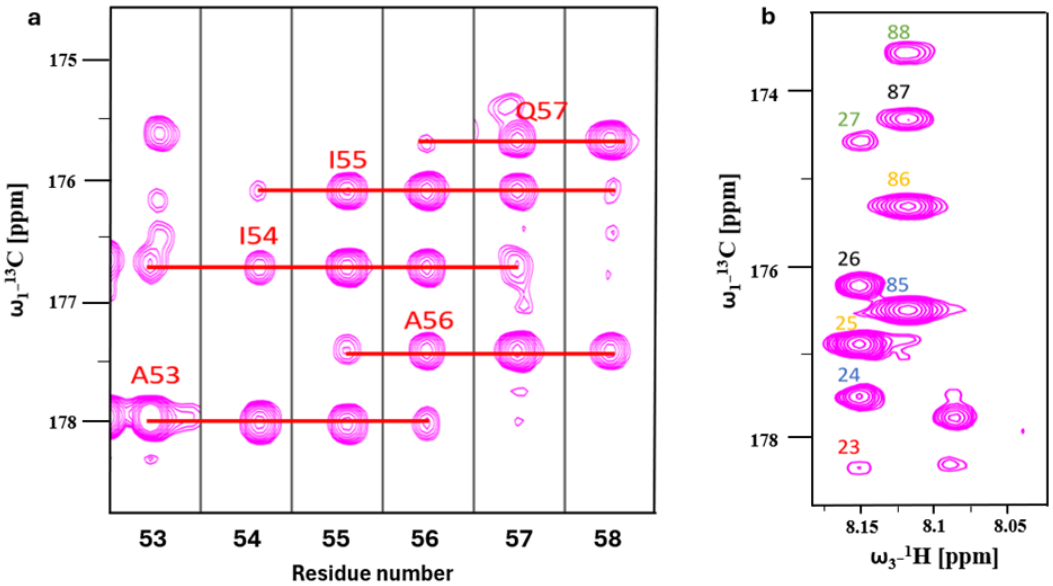

Figure 29: Long range correlations between carbonyl-carbonyl signals in D233.
(a) Strip plots for adjacent residues (plotted at the amide 1H regions for A53 to R58) of uniformly 13C,15N-labelled D233 from 3D (HN)CO(CO)NH experiment. (b) A zoomed F1-F3 region of the 3D (HN)CO(CO)NH spectrum showing the correlation between multiple carbonyl signals (green:i+1, black:i, orange:i-1, blue:i-2, red:i-3). In highly resolved areas it is possible to recognize up to 5 carbonyl correlations following each other in the sequence.

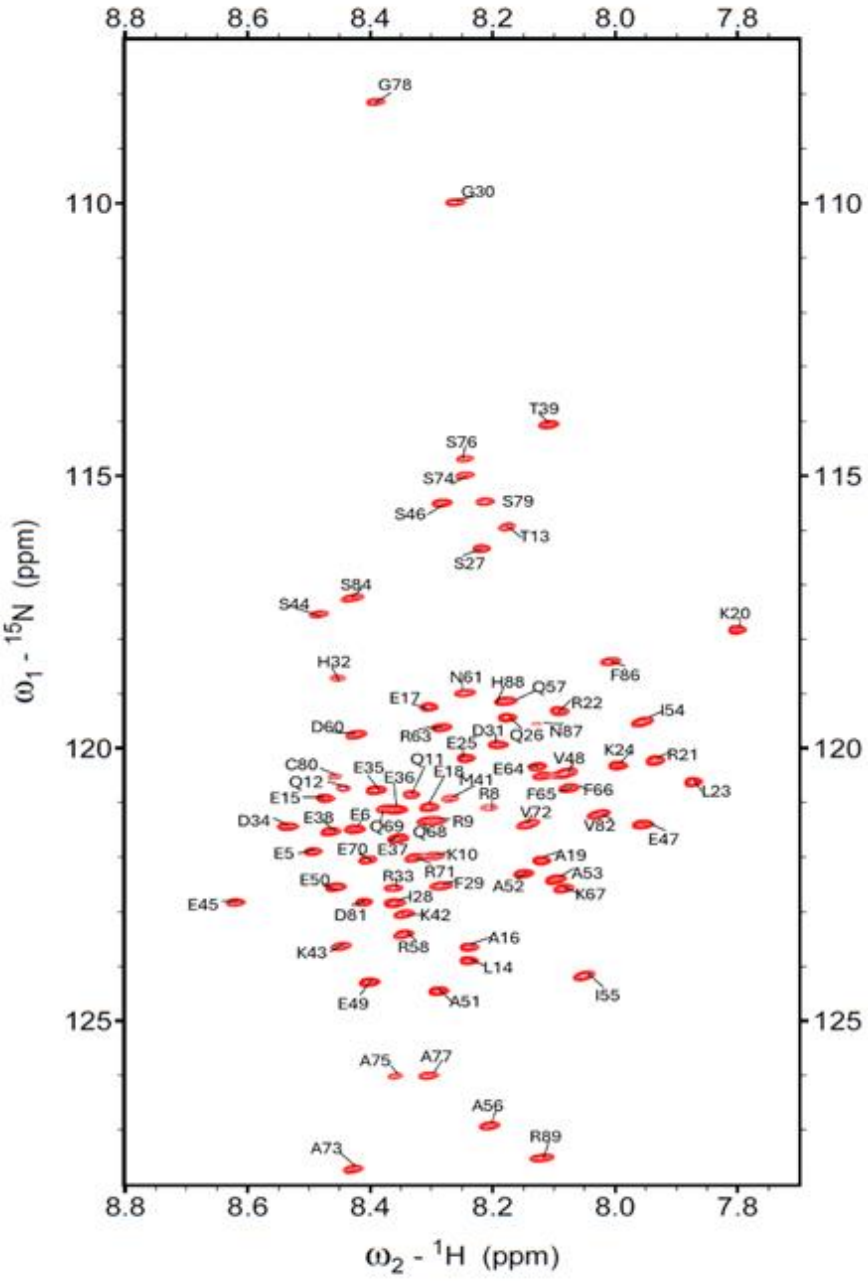

Figure 30: Resonance-assignment of the D233 protein.
^{1}H-^{15}N HSQC spectrum of the D233 construct in 50 mM NaCl, 17 mM NaH_2PO_4, 3 mM Na_2HPO_4, pH 6.0, 5 mM TCEP measured at 25 °C.

The relative propensities revealed by CheSPI align well with the ODiNpred disorder prediction. Following the first 20 residues, the construct adapts a mostly disordered conformation with a minor region of decreased mobility around residue 60. The observed high helical content at the N-terminus might be considered as the C-terminal extension of the Single-Alpha Helix, as in the full protein, the presence of a

longer stable helix is plausible. This raises further questions about the exact domain organization of Drebrin, highlighting the importance of investigating the actin-binding region of Drebrin at an atomic level.

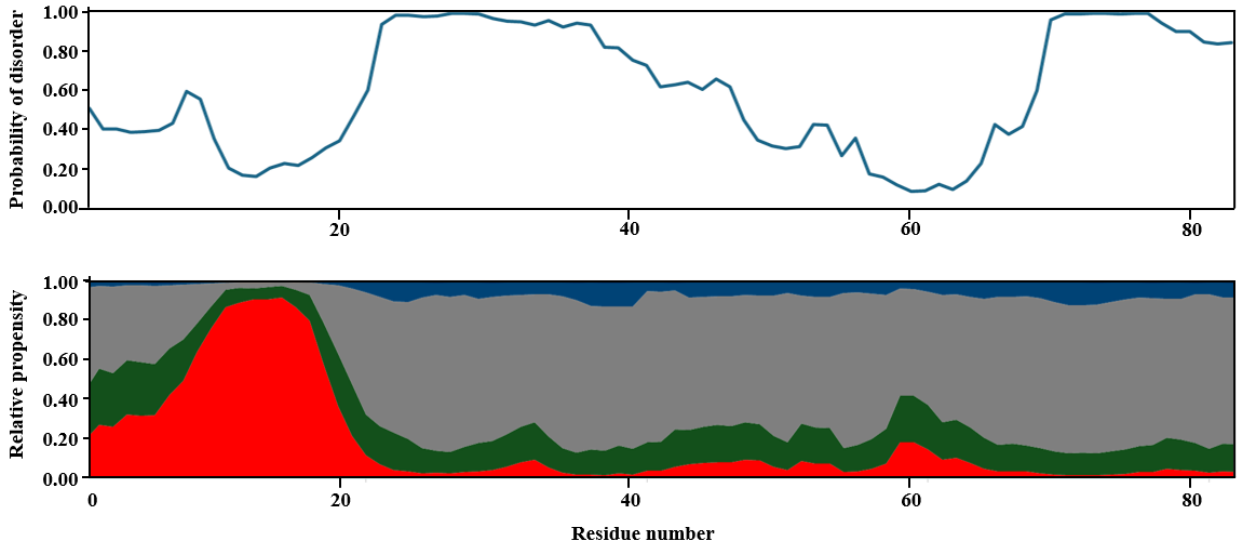

Figure 31: Secondary structural results from the D233 protein.
Comparison of disorder prediction according to ODiNpred (top panel, blue line) with secondary structure propensities obtained via CheSPI (bottom panel; red area: α-helix, green area: turn, grey area: disordered, blue area: extended).

In between the time-consuming acquisition of different 3D experiments, I routinely ran quick 2D experiments, to be able to follow any changes in the sample quality. For this purpose, I frequently chose the $^{1}H^{15}N$ bTROSY experiment, as it is a remarkably quick way to obtain fingerprint-like information from the protein. However, the 3D experiments themselves were $^{1}H^{15}N$ HSQC-based, therefore my other 2D experiments, e.g. the one used for peak picking and resonance-assignment were 2D $^{1}H^{15}N$ HSQC experiments. The bTROSY pulse sequence is quite similar to an HSQC, but without a 180° pulse on ^{1}H during t1 which would refocus the chemical shift evolution and also without decoupling pulse applied in t2. In order to select just the slowest relaxing signal of the four cross peaks that are normally mixed in an HSQC experiment, phase cycling of the ϕ1 and the Ψ2 is used to cancel out all other signals. This leads to a divergence in the ppm value of the chemical shift (Figure 32), which needs to be corrected afterwards when comparing a TROSY to an HSQC-based experiment.

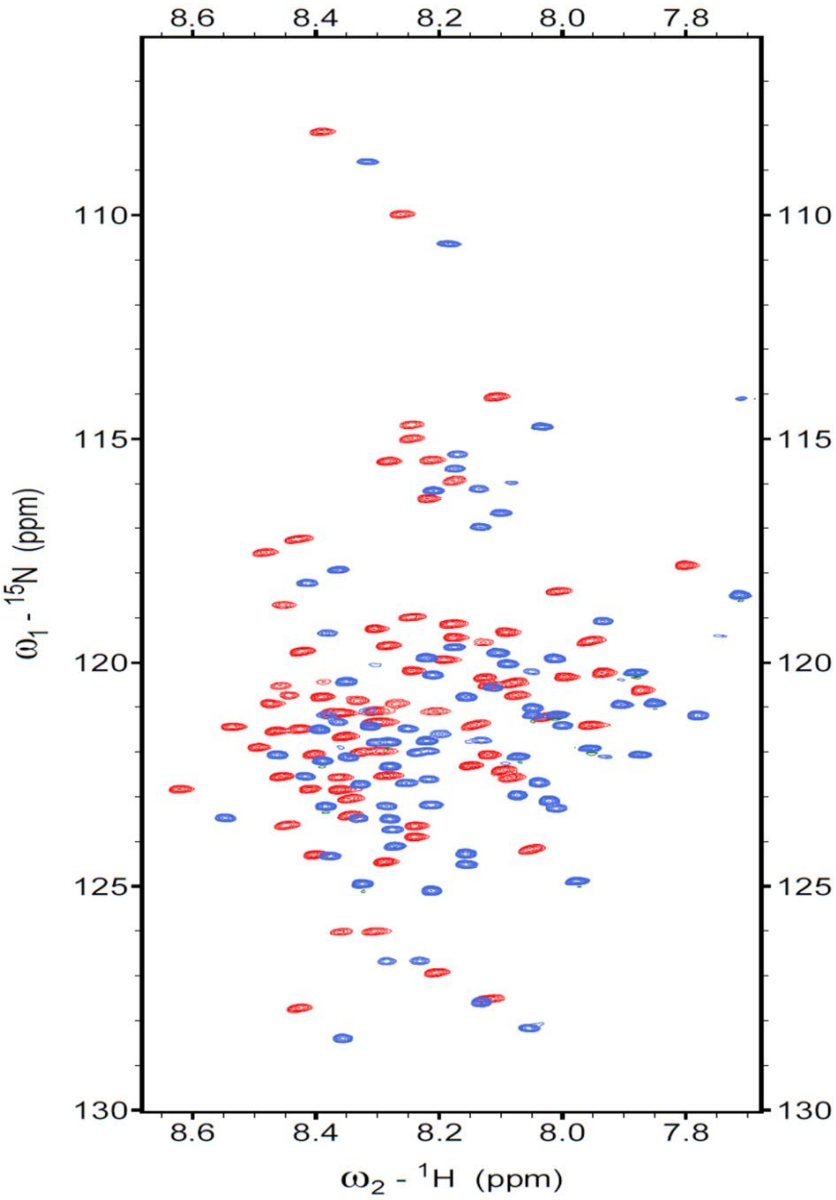

Figure 32: Differences between the $^{1}H^{15}N$ bTROSY and the $^{1}H^{15}N$ HSQC spectra.
$^{1}H^{15}N$ bTROSY spectra is shown in blue and the $^{1}H^{15}N$ HSQC spectra is shown in red. Assigned peaks are labeled with one letter amino acid code.

When superimposing the $^{1}H^{15}N$ bTROSY and $^{1}H^{15}N$ HSQC spectra recorded from the D233 protein, I made an interesting observation: If we take a scalar coupling with an average value of 93 Hz regardless of the amino acid type and then shift one of the spectra by half of that value, the vast majority of the NH signals overlap as expected, but I still experienced a well-defined remaining shift in the case of about 15 peaks (Figure 33). Based on the CheSPI results, these 15 amino acids are exactly the helical segment near the N-terminal that can be interpreted as practically the only structural element of the disordered protein

(Figure 34). This observation raises the possibility of developing a fast, fingerprint-like method aimed at determining the local, possibly transient structural elements of mostly disordered proteins.

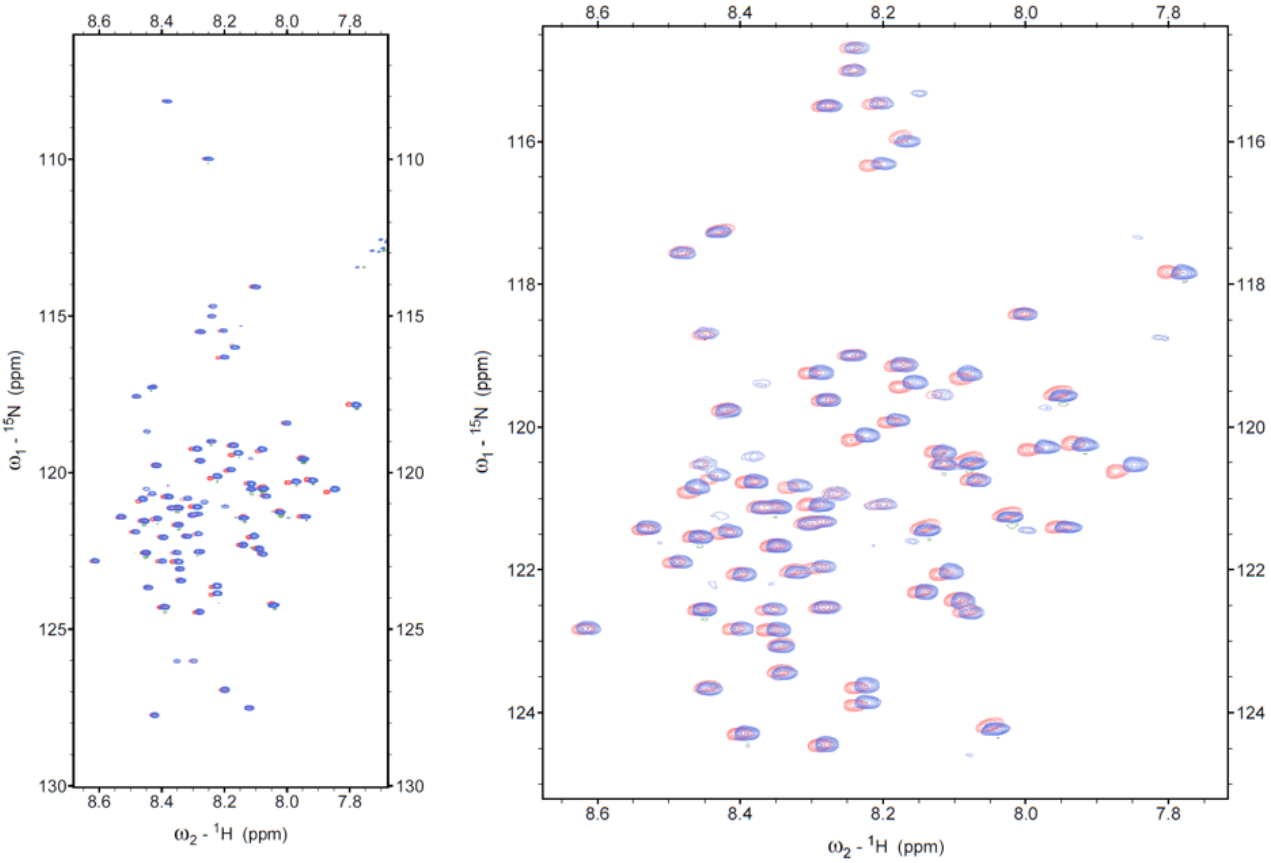

Figure 33: Superimposed $^1H^{15}N$ HSQC and $^1H^{15}N$ bTROSY spectra.
There is a well-defined subset of peak here a remaining shift is still observable after correction.

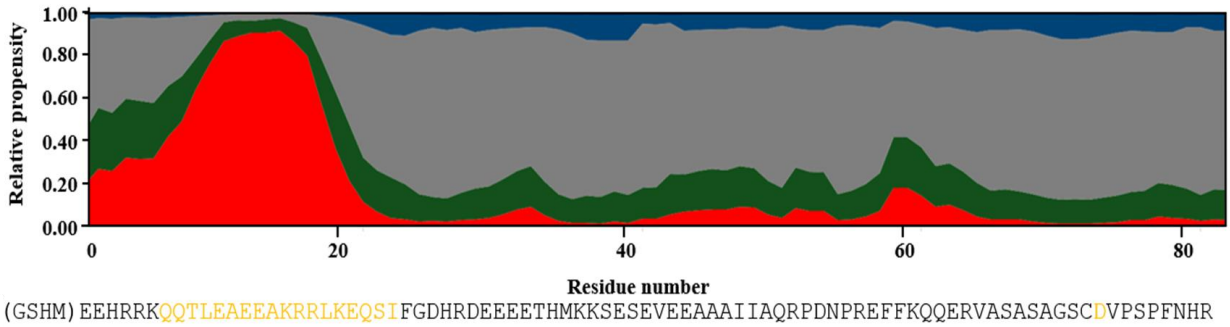

Figure 34: Peaks with remaining shift highlighted along the amino acid sequence of the D233 construct.
Besides asparagine 81, they are located sequentially adjacent, strengthening the connection of the observed effect with the detected secondary structural content near the N-termini of the protein

5.2.4. Exploratory NMR investigation of the Drebrin D233-Actin interaction

The first attempt to perform stepwise F-actin titration of D233 was hindered by the observation that the addition of ATP causes notable chemical shift perturbation of several, but not all amide NH peaks, raising the possibility of some kind of interaction between the protein and the small molecule (Figure 35,B). ATP is on the one hand not necessary for the actin polymerization, but accelerates the process, and has been also suggested to play some role in the Drebrin-actin interaction (15,24). As intrinsically disordered proteins are also capable of ATP binding (154), it is important to distinguish between ATP-and actin-induced effects. In order to do so, we also performed titration experiments with F-actin where all solutions contained ATP in the same concentration. We found almost no or minor chemical shift perturbations, however non-uniform peak intensity changes appeared in a few cases (Figure 35,A).

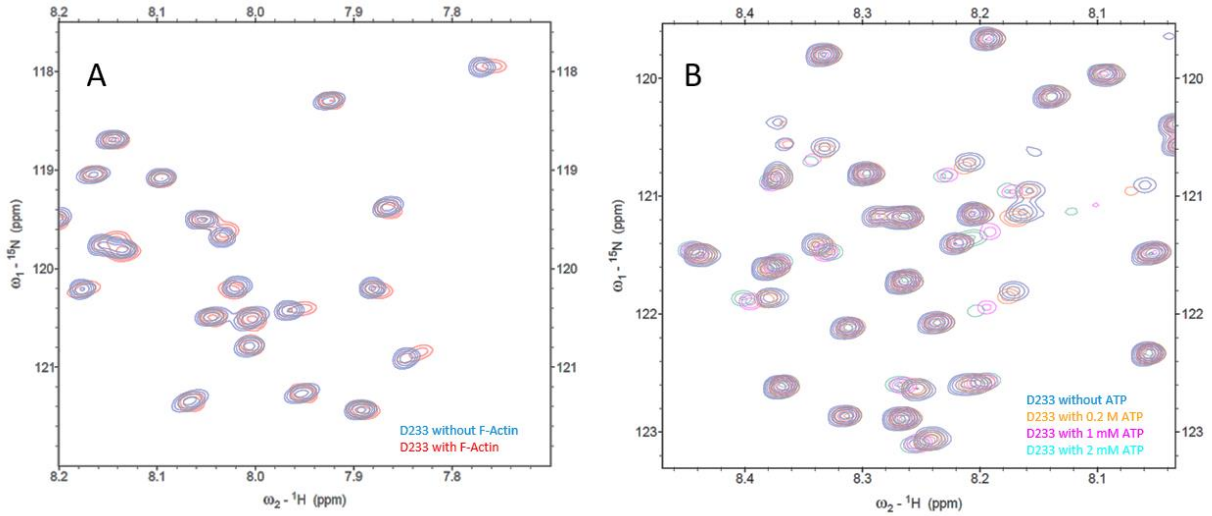

Figure 35: Exploratory NMR titrations of D233.
A, ^{1}H-^{15}N HSQC spectrum of D233 overlayed with a spectrum of D233 in the presence of F-actin. B, ^{1}H-^{15}N HSQC spectrum of D233 overlayed with spectra of D233 in the presence of increasing ATP concentrations.

T2 relaxation experiments indicated significant changes in the protein dynamics upon F-actin addition, suggesting an increase in molecular weight, likely caused by the binding of the flexible D233 to the slowly tumbling actin filaments (Figure 36). The R2 rates of the disordered D233 protein were mostly within the range between 1-3, as expected (85). Notably, the helical segment revealed by CheSpi near the N-terminal showed larger R2 values, further proving the presence of a less mobile region in the largely disordered construct. The somewhat surprising observation, that the increase in the R2 rates is rather uniformal than sequentially localized, and thereby not highlighting the interaction interface raises the possibility of a complex binding

mechanism. It is possible that the kinetics of protein-protein interaction occurs on a time scale where the R2 relaxation rates average out in such a way that they lose their sensitivity to the chemical shifts existing in the free and bound forms. For this reason, the effect is not localized to certain regions of the sequence, raising the possibility of a higher order motion governing the interaction.

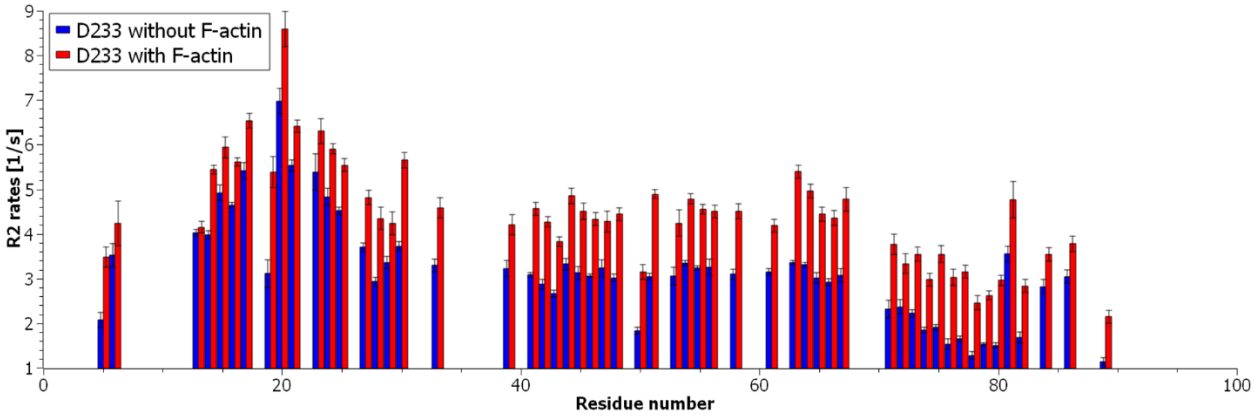

Figure 36: Changes in D233 protein dynamics upon addition of F-actin.
Backbone ^{15}N R2 relaxation rates of D233 in the absence (blue) and presence (red) of F-actin.

6. Discussion

During my PhD work, I managed to substantially extend the atomic-level information available from Drebrin. This has been mainly achieved through the investigation of 2 selected protein segments: the Drebrin-SAH and the D233 construct.

I established the expression of both proteins in *E. coli* host system and established their respective purification protocols. Since none of these have been investigated by others, or at least, have not been published, I had to try several approaches and compare them, in order to have a robust sample preparation method. The isotopic labelling required for NMR experiments is very costly, therefore I had to make sure that I can make the most from the batches I decided to label. At the end, 250 ml of ^{13}C and ^{15}N labelled media was enough to get one concentrated and pure enough sample for multidimensional NMR investigations.

I performed the complete backbone-and partial side-chain assignment of the 2 proteins. The severe signal overlap resulted in an extremely challenging assignment process in both cases. The 4D (HACA)CON(CA)NH and 4D (HACA)N(CA)CONH experiments helped me to deposit only the 3rd available chemical shift list from a SAH to the BMRB, and the 3D (HN)CO(CO)NH experiment accelerated the process tremendously for the disordered D233. I would like to emphasize that since there is no other assignment available from these protein segments, I had no reference to compare my assigned peaks, therefore no other information could aid the process.

From the 2 available SAH papers where NMR was the main method to obtain structural information, Peckham and colleagues had a very similar spectral crowding, which they could also only overcome by tedious work. Bax and colleagues however applied perdeuteration, which mitigated spectral overlay resulting from dipolar coupling between parallelly aligned amide vectors. I am almost certain that this approach would improve the $^{1}H^{15}N$ HSQC spectra of Drebrin-SAH as well. However, this labelling technique has an even higher price than the conservative ^{13}C and ^{15}N strategy. When I started my PhD, a complete assignment of the Drebrin-SAH was rather a bold dream, than a realistic expectation. Therefore, I had no intention to apply such an expensive methodology, with the huge risk, that it will be still insufficient to solve the problem. Retrospectively, I could have made the process less demanding while obtaining much better

resolution in D_2O, but it was a reasonable decision to first verify what I can and what I can not achieve.

In the future, it would still open up possibilities, to attempt this, for example, pH titration experiments would be useful to characterize the role of the ionic interactions in detail. To this end, the NMR analysis of the behavior of the side chain carbon atoms closest to the titratable groups (in Asp, Glu, Lys and Arg but also in His residues), thus most sensitive to the pH-induced changes, is necessary. This requires spectra where these carbons are both clearly resolved, and their unambiguous assignment is possible. Once I would manage to obtain proper resolution, I could probe the presence of salt bridges between the charged side chains of the SAH which are believed to play key importance in the dynamics of the extended motif. It would be my interest to perform pH titration of both backbone and sidechain nuclei to experimentally determine pKa values, which then can be directly compared to their expected values. Any deviations would be clear indicators of favorable protonated or deprotonated states caused by local chemical environment, thereby proving the presence of opposing charges in proximity. Another ambitious aim would be to investigate the putative kinks and local unfoldings in the helix by measuring amide hydrogen-deuterium exchange rates to determine regional flexibility. With acquiring these important information on local mobility and electrostatic parameters, I could further extend the modelling of the dynamic behavior of SAH motifs encoded in their unique sequential properties.

On the side of the D233 construct, there are also many questions remaining unanswered. By providing the chemical shift list of this segment, I laid the foundation of further, more detailed investigations. Some of these (exploratory NMR titrations, T2 relaxation measurements) have been briefly discussed in the results section, but as my exchange period in Linz had to come to an end, I did not have the necessary time to properly investigate and analyze these observations. It would be important to dissect the possible contributions caused by ATP and actin itself, as well as to monitor the changes in the actin organization as much as possible, to account for the actin bundling activity of Drebrin.

Investigating the actin-binding properties of Drebrin is a challenging task hindered by the complexity of the sample environment. My preliminary results suggest the possibility of an ultrafast interaction between the intrinsically disordered D233 construct and slowly tumbling actin filaments, similar to the situation of nuclear transport receptors and FG segments (86,155). To

further characterize this biomolecular interaction, I would first investigate whether ATP influences the conformation of Drebrin constructs by evaluating chemical shift perturbations. It would be advised to use appropriate controls like phosphate-containing compounds, other nucleotides etc. to characterize the specificity of the observed interaction. If ATP-induced conformational changes occur, their impact on actin-binding could be assessed using additional NMR titration experiments. Once this has been achieved, the next step could be to extend the initial T2 relaxation experiments using varying Drebrin:actin ratios to identify the regions mainly responsible for binding.

To complement the findings obtained with NMR spectroscopy and ensure robust conclusions, I would consider applying fluorescence anisotropy-based assays, which provide an effective means of monitoring interactions between the flexible Drebrin segments and the high-molecular-weight F-Actin. This approach would allow rapid screening of Drebrin constructs of varying lengths, enabling me to precisely define the actin-binding region.

From the secondary chemical shift analysis, it appears that the segment near the N-terminal region of the D233 construct, following immediately the SAH segment, exhibits substantial helical propensity. This raises the question on the exact boundaries of the helical and intrinsically disordered regions. Among the plethora of actin-binding proteins there are some that have been described to be intrinsically disordered. In two of these, helical segments and helical structural propensity seem to play a role in actin binding (156,157). In addition, SAH segments are relatively abundant in cytoskeleton-associated proteins. These observations call for the detailed investigation of the role of the SAH segment and the neighboring disordered region of Drebrin in actin binding. One possible way for that could be implementing segmental labeling strategies. Specifically, constructs where the SAH segment is labeled with ^{15}N, ^{13}C, while the intrinsically disordered segment remains unlabeled, and vice versa. An intein-based expression system might be optimal for this purpose. Such segmentally labeled constructs would not only mitigate spectral crowding but also facilitate direct spectral comparisons between the shorter and extended constructs in both free and actin-bound states. On top of intein-based systems, other methods, such as the use of a cell-free expression system would be also worth considering. Incorporating amber codon suppression could be employed, as has been successfully demonstrated for glutamine-rich proteins (158,159) . This would not be able to yield the exact labeling pattern achievable by segmental labeling but would still enable to obtain site-specific information that could not be otherwise available due to substantial spectral crowding.

7. Thesis points

1./a: *I prepared plasmid DNA containing the sequence encoding the previously predicted single alpha-helix region in the postsynaptic Drebrin protein. I transformed this nucleic acid construct into E. coli cells, then optimized the bacterial expression and recombinant protein purification protocols, thus preparing a protein sample suitable for NMR structural analysis.*

1./b: *To characterize the Drebrin-actin interaction, which is yet to be described on an atomic level with consensus, I designed the D233 construct, prepared the necessary plasmid DNA, and then further developed the methods for the expression and purification of the single alpha-helix to prepare a protein sample suitable for NMR functional studies.*

2./a: *I confirmed the monomer structure of the single alpha-helix in aqueous solution by CD spectroscopy and mass spectrometry. I performed the complete ^{1}H-^{15}N-^{13}C resonance assignment of the protein backbone, and the partial resonance assignment of the protein side chains by 4-dimensional NMR experiments. I demonstrated the local structural preference of the protein through Cα and Cβ secondary chemical shifts.*

2./b: *Using NMR experiments specialized for disordered proteins, I performed the full ^{1}H-^{15}N-^{13}C resonance assignment of the D233 protein backbone and the partial resonance assignment of the protein side chains. The obtained chemical shifts indicated a high degree of disorder in the protein, with the exception of the helical region observed at the N-terminal section.*

3: *Driven by NMR and SAXS data, further aided by molecular dynamics simulations, I constructed an ensemble-based model of the single alpha-helix, which reflects both the local and global structural parameters revealed by experiments and highlights the formation of a transient network of salt bridges and cation-pi interactions that provide the extraordinary stability of the helical motif.*

4: *To characterize the Drebrin-actin interaction at the atomic level, I optimized NMR titrations and T2 relaxation measurements. Based on the changes observed in the D233 signals upon addition of F-actin, I was able to set up a method to confirm the binding, which can serve as the basis for more detailed studies in the future.*

8. Acknowledgements

I would like to express my gratitude towards all the wonderful people I had the chance to meet during this journey. My work heavily relied on collaborations bridging research groups and countries, and on top of the results yielded from these experiments, I mostly improved as a scientist and as a person while being inspired by amazing colleagues.

I am grateful to my former supervisors, Dr Szilveszter Gergely for navigating my first research project during my BSc and Dr Ádám Fizil to introduce me to the world of NMR spectroscopy during my MSc thesis work and guiding me to the Gáspári group for my PhD years.

I am thankful to Dr Cy M Jeffries for his immense trust on me and for letting me operate the SAXS beamline in Hamburg. His contributions to data processing and analysis were beyond helpful.

I am extremely happy to remember my 10 month long exchange in Linz, which was more than successful and enjoyable, thanks to the sparking research group members, whom I dearly miss until this very day. It was a great pleasure to be managed by Dr Frans Mulder, and to share work, knowledge and fun with Julie Maibøll Kaasen. This project was only possible in the organized lab environment rigorously provided by Jakob Schmelzer.

I would not become the independently working young scientist without the always encouraging attitude of my supervisor Dr Bálint Ferenc Péterfia, and our research group leader Dr Zoltán Gáspári. I am thankful for them to give me freedom in research and trusting me while throwing into deep water. My problem-solving skills could not have developed so much if not their endless faith, that I will navigate myself out of difficulties.

During the burdensome and demotivating segments of my PhD, I could always rely on my friends to keep my mental health, and I am grateful to be accompanied by such amazing people.

Last but not least, I am pleased to be a member of a family, which was always behind me, and raised me to be the person I am today.

Without all of you, this thesis would not have been prepared, and I am grateful for everything I got from you during these challenging 4 years!

9. List of publications

9.1 Journal publications of the theses

Varga, S., Péterfia, BF., Dudola, D., Farkas, V., Jeffries, CM., Permi, P., Gáspári, Z. (**2025**). Dynamic Interchange of Local Residue-Residue Interactions in the Largely Extended Single Alpha-Helix in Drebrin. Biochemical Journal, vol. 482, no. 08, pp. 383–399, https://doi.org/10.1042/BCJ20253036

Varga, S., Kaasen, JM., Gáspári, Z., Péterfia, BF., Mulder, FAA. (2025). Resonance assignment of the intrinsically disordered actin-binding region of Drebrin. Biomolecular NMR Assignments, https://doi.org/10.1007/s12104-025-10239-0

9.2 Further journal publications

Szabó, AL., Nagy-Kanta, E., Varga, S., Jáger, EA., Pongor, CI., Laki, M., Laki, AJ., Gáspári, Z. (**2025**). Diffusion-based size determination of solute particles: a method adapted for PSD proteins, FEBS Open Bio, revised manuscript submitted

Karjalainen, M., Kontunen, A., Anttalainen, A., Mäkelä, M., Varga,S., Lepomäki, M., Anttalainen, O., Kumpulainen, P., Oksala, N., Roine, A., Vehkaoja, A. (**2022**). Characterization of signal kinetics in real time surgical tissue classification system. Sensors and Actuators B: Chemical, Volume 365, 2022, 131902, https://doi.org/10.1016/j.snb.2022.131902.

9.3 Conference talks

-Conference presentation at the “3rd ML4NGP MEETING on Machine Learning and Non-globular proteins, Vilnius, May 20-23, 2025” conference
-Conference presentation at the “Hungarian NMR Working Committee Meeting, Balatonszemes, May 8-9, 2025” conference
-Conference presentation at the “Hungarian Molecular Life Science Conference 2025, Eger, March 28-30, 2025” conference
-Presentation at the “Zechmeister László Lecture Competition, Hungarian Academy of Sciences, 2024.11.15.” lecture competition, 2nd place award
-Conference presentation at the “Hungarian NMR Working Committee Meeting, Balatonszemes, May 23-24, 2024” conference

9.4 Conference posters

-Poster at the “46th Danish NMR meeting, Rebild January 30-31, 2025” conference
-Poster at the “Small Angle Neutron and X-ray Scattering from biomacromolecules in solution, 16 – 20 September 2024 | Grenoble, France, organized by European Molecular Biology Organization” course
-Poster at the “The 48th FEBS Congress, 29 June – 3 July 2024, Milano, Italy” conference
-Poster at the “45th Danish NMR meeting, Roskilde January 29-30, 2024” conference
-Poster at the “NMR for combatting diseases: from cancer to SARS-CoV-2 - Sesto Fiorentino, Italy, 27/03/2023 - 31/03/2023, organized by ICGEB” course
-Poster at the “iNEXT-Discovery 2023 Experimental and computational aspects of Structural Chemistry and Biology 22-24 June 2023 Budapest, Hungary" conference

10. Bibliography

1. Boeckers TM. The postsynaptic density. Cell Tissue Res. 2006 Nov 25;326(2):409–22.
2. SUNDBERG RD, SCHAAR FE, POWELL MJ, DENBOER D. Tissue mast cells in human umbilical cord, and the anticoagulant activity of dried extracts of cords and placentae. Anat Rec. 1954 Jan;118(1):35–56.
3. Klauck TM, Scott JD. The postsynaptic density: A subcellular anchor for signal transduction enzymes. Cell Signal. 1995 Nov;7(8):747–57.
4. Ziff EB. Enlightening the Postsynaptic Density. Neuron. 1997 Dec;19(6):1163–74.
5. Kennedy MB, Bennett MK, Erondu NE. Biochemical and immunochemical evidence that the “major postsynaptic density protein” is a subunit of a calmodulin-dependent protein kinase. Proceedings of the National Academy of Sciences. 1983 Dec;80(23):7357–61.
6. Husi H, Ward MA, Choudhary JS, Blackstock WP, Grant SGN. Proteomic analysis of NMDA receptor–adhesion protein signaling complexes. Nat Neurosci. 2000 Jul 1;3(7):661–9.
7. Sheng M, Sala C. PDZ Domains and the Organization of Supramolecular Complexes. Annu Rev Neurosci. 2001 Mar;24(1):1–29.
8. Grabrucker AM. A role for synaptic zinc in ProSAP/Shank PSD scaffold malformation in autism spectrum disorders. Dev Neurobiol. 2014 Feb 11;74(2):136–46.
9. Savioz A, Leuba G, Vallet PG. A framework to understand the variations of PSD-95 expression in brain aging and in Alzheimer’s disease. Ageing Res Rev. 2014 Nov;18:86–94.
10. Durand CM, Betancur C, Boeckers TM, Bockmann J, Chaste P, Fauchereau F, et al. Mutations in the gene encoding the synaptic scaffolding protein SHANK3 are associated with autism spectrum disorders. Nat Genet. 2007 Jan 17;39(1):25–7.
11. Varga S, Péterfia BF, Dudola D, Farkas V, Jeffries CM, Permi P, et al. Dynamic interchange of local residue–residue interactions in the largely extended single alpha-helix in Drebrin. Biochemical Journal. 2025 Apr 24;482(08):383–99.

12. Pérez-Martínez M, Gordón-Alonso M, Cabrero JR, Barrero-Villar M, Rey M, Mittelbrunn M, et al. F-actin-binding protein drebrin regulates CXCR4 recruitment to the immune synapse. J Cell Sci. 2010 Apr 1;123(7):1160–70.
13. Lin W, Shiomoto S, Yamada S, Watanabe H, Kawashima Y, Eguchi Y, et al. Dendritic spine formation and synapse maturation in transcription factor-induced human iPSC-derived neurons. iScience. 2023 Apr;26(4):106285.
14. Li Z, Liu H, Li J, Yang Q, Feng Z, Li Y, et al. Homer Tetramer Promotes Actin Bundling Activity of Drebrin. Structure. 2019 Jan 2;27(1):27-38.e4.
15. Hayashi K, Ishikawa R, Kawai-Hirai R, Takagi T, Taketomi A, Shirao T. Domain Analysis of the Actin-Binding and Actin-Remodeling Activities of Drebrin [Internet]. 1999. Available from: http://www.idealibrary.com
16. Mikati MA, Grintsevich EE, Reisler E. Drebrin-induced stabilization of actin filaments. Journal of Biological Chemistry. 2013 Jul 5;288(27):19926–38.
17. Lappalainen P, Kessels MM, Jamie M, Cope T V, Drubin DG. Essay The ADF Homology (ADF-H) Domain: A Highly Exploited Actin-binding Module. Vol. 9, Molecular Biology of the Cell. 1998.
18. Hayashi K, Shirao T. Change in the shape of dendritic spines caused by overexpression of drebrin in cultured cortical neurons. J Neurosci. 1999 May 15;19(10):3918–25.
19. Shirao T, Hanamura K, Koganezawa N, Ishizuka Y, Yamazaki H, Sekino Y. The role of drebrin in neurons. Vol. 141, Journal of Neurochemistry. Blackwell Publishing Ltd; 2017. p. 819–34.
20. Poukkula M, Kremneva E, Serlachius M, Lappalainen P. Actin-depolymerizing factor homology domain: A conserved fold performing diverse roles in cytoskeletal dynamics. Cytoskeleton. 2011 Sep 13;68(9):471–90.
21. Yao N, Li J, Liu H, Wan J, Liu W, Zhang M. The Structure of the ZMYND8/Drebrin Complex Suggests a Cytoplasmic Sequestering Mechanism of ZMYND8 by Drebrin. Structure. 2017 Nov 7;25(11):1657-1666.e3.
22. Biou V, Brinkhaus H, Malenka RC, Matus A. Interactions between drebrin and Ras regulate dendritic spine plasticity. European Journal of Neuroscience. 2008 Jun 28;27(11):2847–59.

23. Ivanov A, Esclapez M, Pellegrino C, Shirao T, Ferhat L. Drebrin A regulates dendritic spine plasticity and synaptic function in mature cultured hippocampal neurons. J Cell Sci. 2009 Feb 15;122(4):524–34.
24. Grintsevich EE, Galkin VE, Orlova A, Ytterberg AJ, Mikati MM, Kudryashov DS, et al. Mapping of Drebrin Binding Site on F-Actin. J Mol Biol. 2010;398(4):542–54.
25. Worth DC, Daly CN, Geraldo S, Oozeer F, Gordon-Weeks PR. Drebrin contains a cryptic F-actin-bundling activity regulated by Cdk5 phosphorylation. Journal of Cell Biology. 2013;202(5):793–806.
26. Ma W, Yang L, He L. Overview of the detection methods for equilibrium dissociation constant KD of drug-receptor interaction. J Pharm Anal. 2018 Jun;8(3):147–52.
27. Wang E, Wang CLA. (i,i+ 4) Ion Pairs Stabilize Helical Peptides Derived from Smooth Muscle Caldesmon. Arch Biochem Biophys. 1996 May;329(2):156–62.
28. Knight PJ, Thirumurugan K, Xu Y, Wang F, Kalverda AP, Stafford WF, et al. The Predicted Coiled-coil Domain of Myosin 10 Forms a Novel Elongated Domain That Lengthens the Head. Journal of Biological Chemistry. 2005 Oct;280(41):34702–8.
29. Li J, Chen Y, Deng Y, Unarta IC, Lu Q, Huang X, et al. Ca2+-Induced Rigidity Change of the Myosin VIIa IQ Motif-Single α Helix Lever Arm Extension. Structure. 2017 Apr 4;25(4):579-591.e4.
30. Rosas R, Aguilar RR, Arslanovic N, Seck A, Smith DJ, Tyler JK, et al. A novel single alpha-helix DNA-binding domain in CAF-1 promotes gene silencing and DNA damage survival through tetrasome-length DNA selectivity and spacer function. Elife. 2023;12.
31. Barnes CA, Shen Y, Ying J, Takagi Y, Torchia DA, Sellers JR, et al. Remarkable Rigidity of the Single α-Helical Domain of Myosin-VI As Revealed by NMR Spectroscopy. J Am Chem Soc. 2019 Jun 5;141(22):9004–17.
32. Batchelor M, Wolny M, Baker EG, Paci E, Kalverda AP, Peckham M. Dynamic ion pair behavior stabilizes single -helices in proteins. Journal of Biological Chemistry. 2019 Mar 1;294(9):3219–34.
33. Harmat Z, Dudola D, Gáspári Z. Dipend: An open-source pipeline to generate ensembles of disordered segments using neighbor-dependent backbone preferences. Biomolecules. 2021 Oct 1;11(10).

34. Spink BJ, Sivaramakrishnan S, Lipfert J, Doniach S, Spudich JA. Long single α-helical tail domains bridge the gap between structure and function of myosin VI. Nat Struct Mol Biol. 2008 Jun;15(6):591–7.
35. Sivaramakrishnan S, Spink BJ, Sim AYL, Doniach S, Spudich JA. Dynamic charge interactions create surprising rigidity in the ER/K α-helical protein motif. Proceedings of the National Academy of Sciences. 2008 Sep 9;105(36):13356–61.
36. Kovács Á, Dudola D, Nyitray L, Tóth G, Nagy Z, Gáspári Z. Detection of single alpha-helices in large protein sequence sets using hardware acceleration. J Struct Biol. 2018 Oct 1;204(1):109–16.
37. Baboolal TG, Sakamoto T, Forgacs E, White HD, Jackson SM, Takagi Y, et al. The SAH domain extends the functional length of the myosin lever. Proceedings of the National Academy of Sciences. 2009 Dec 29;106(52):22193–8.
38. Wolny M, Batchelor M, Bartlett GJ, Baker EG, Kurzawa M, Knight PJ, et al. Characterization of long and stable de novo single alpha-helix domains provides novel insight into their stability. Sci Rep. 2017 Mar 13;7.
39. Beneken J, Tu JC, Xiao B, Nuriya M, Yuan JP, Worley PF, et al. Structure of the Homer EVH1 Domain-Peptide Complex Reveals a New Twist in Polyproline Recognition. Neuron. 2000 Apr;26(1):143–54.
40. Karlsson E, Schnatwinkel J, Paissoni C, Andersson E, Herrmann C, Camilloni C, et al. Disordered Regions Flanking the Binding Interface Modulate Affinity between CBP and NCOA. J Mol Biol. 2022 Jul;434(13):167643.
41. Karlsson E, Ottoson C, Ye W, Andersson E, Jemth P. Intrinsically Disordered Flanking Regions Increase the Affinity of a Transcriptional Coactivator Interaction across Vertebrates. Biochemistry. 2023 Sep 19;62(18):2710–6.
42. Palopoli N, González Foutel NS, Gibson TJ, Chemes LB. Short linear motif core and flanking regions modulate retinoblastoma protein binding affinity and specificity. Protein Engineering, Design and Selection. 2018 Mar 1;31(3):69–77.
43. Giunta CJ, Mainz V V. Discovery of Nuclear Magnetic Resonance: Rabi, Purcell, and Bloch. In 2020. p. 3–20.
44. Rabi II. Space Quantization in a Gyrating Magnetic Field. Physical Review. 1937 Apr 15;51(8):652–4.

45. van der Waals JH. van der Waals, J. H.: Gorter's Footprints on the Trail That Led to Magnetic Resonance. In: Encyclopedia of Magnetic Resonance. Chichester, UK: John Wiley & Sons, Ltd; 2007.
46. Alvarez LW, Bloch F. A Quantitative Determination of the Neutron Moment in Absolute Nuclear Magnetons. Physical Review. 1940 Jan 15;57(2):111–22.
47. Purcell EM, Torrey HC, Pound R V. Resonance Absorption by Nuclear Magnetic Moments in a Solid. Physical Review. 1946 Jan 1;69(1–2):37–8.
48. Arnold JT, Dharmatti SS, Packard ME. Chemical Effects on Nuclear Induction Signals from Organic Compounds. J Chem Phys. 1951 Apr 1;19(4):507–507.
49. Liddel U, Ramsey NF. Temperature Dependent Magnetic Shielding in Ethyl Alcohol. J Chem Phys. 1951 Dec 1;19(12):1608–1608.
50. Proctor WG, Yu FC. The Dependence of a Nuclear Magnetic Resonance Frequency upon Chemical Compound. Physical Review. 1950 Mar 1;77(5):717–717.
51. Gutowsky HS, McCall DW. Nuclear Magnetic Resonance Fine Structure in Liquids. Physical Review. 1951 Jun 1;82(5):748–9.
52. Baek M, DiMaio F, Anishchenko I, Dauparas J, Ovchinnikov S, Lee GR, et al. Accurate prediction of protein structures and interactions using a three-track neural network. Science (1979). 2021 Aug 20;373(6557):871–6.
53. Jumper J, Evans R, Pritzel A, Green T, Figurnov M, Ronneberger O, et al. Highly accurate protein structure prediction with AlphaFold. Nature. 2021 Aug 26;596(7873):583–9.
54. Abramson J, Adler J, Dunger J, Evans R, Green T, Pritzel A, et al. Accurate structure prediction of biomolecular interactions with AlphaFold 3. Nature. 2024 Jun 13;630(8016):493–500.
55. Gáspári Z. Fehérjeszerkezetek a számítógépből: a 2024-es kémiai Nobel-díj. Magyar Kémikusok Lapja. 2025 Feb;
56. Laurents D V. AlphaFold 2 and NMR Spectroscopy: Partners to Understand Protein Structure, Dynamics and Function. Front Mol Biosci. 2022 May 17;9.
57. Sever AIM, Ahmed R, Rößler P, Kay LE. Solution NMR goes big: Atomic resolution studies of protein components of molecular machines and phase-separated condensates. Curr Opin Struct Biol. 2025 Feb;90:102976.

58. Pajkos M, Clerc I, Zanon C, Bernadó P, Cortés J. AFflecto: A web server to generate conformational ensembles of flexible proteins from AlphaFold models. J Mol Biol. 2025 Feb;169003.
59. Tesei G, Trolle AI, Jonsson N, Betz J, Knudsen FE, Pesce F, et al. Conformational ensembles of the human intrinsically disordered proteome. Nature. 2024 Feb 22;626(8000):897–904.
60. Kawale AA, Burmann BM. Characterization of backbone dynamics using solution NMR spectroscopy to discern the functional plasticity of structurally analogous proteins. STAR Protoc. 2021 Dec;2(4):100919.
61. Sekhar A, Kay LE. An NMR View of Protein Dynamics in Health and Disease. Annu Rev Biophys. 2019 May 6;48(1):297–319.
62. Wagner G, Wüthrich K. Proton NMR studies of the aromatic residues in the basic pancreatic trypsin inhibitor (BPTI). Journal of Magnetic Resonance (1969). 1975 Dec;20(3):435–45.
63. Berndt KD, Güntert P, Orbons LPM, Wüthrich K. Determination of a high-quality nuclear magnetic resonance solution structure of the bovine pancreatic trypsin inhibitor and comparison with three crystal structures. J Mol Biol. 1992 Oct;227(3):757–75.
64. Li KB, Sanctuary BC. Automated Resonance Assignment of Proteins Using Heteronuclear 3D NMR. 1. Backbone Spin Systems Extraction and Creation of Polypeptides. J Chem Inf Comput Sci. 1997 Mar 1;37(2):359–66.
65. Guerry P, Duong VD, Herrmann T. CASD-NMR 2: robust and accurate unsupervised analysis of raw NOESY spectra and protein structure determination with UNIO. J Biomol NMR. 2015 Aug 28;62(4):473–80.
66. Bahrami A, Assadi AH, Markley JL, Eghbalnia HR. Probabilistic Interaction Network of Evidence Algorithm and its Application to Complete Labeling of Peak Lists from Protein NMR Spectroscopy. PLoS Comput Biol. 2009 Mar 13;5(3):e1000307.
67. Schmidt E, Güntert P. A New Algorithm for Reliable and General NMR Resonance Assignment. J Am Chem Soc. 2012 Aug 1;134(30):12817–29.

68. Yao J, Dyson HJ, Wright PE. Chemical shift dispersion and secondary structure prediction in unfolded and partly folded proteins. FEBS Lett. 1997 Dec 15;419(2–3):285–9.
69. Schiavina M, Bracaglia L, Bolognesi T, Rodella MA, Tagliaferro G, Tino AS, et al. Intrinsically disordered proteins studied by NMR spectroscopy. J Magn Reson Open. 2024 Mar 1;18.
70. Murrali MG, Schiavina M, Sainati V, Bermel W, Pierattelli R, Felli IC. 13C APSY-NMR for sequential assignment of intrinsically disordered proteins. J Biomol NMR. 2018 Mar 28;70(3):167–75.
71. Mäntylahti S, Tossavainen H, Hellman M, Permi P. An intraresidual i(HCA)CO(CA)NH experiment for the assignment of main-chain resonances in 15N, 13C labeled proteins. J Biomol NMR. 2009;45(3):301–10.
72. Yoshimura Y, Kulminskaya N V., Mulder FAA. Easy and unambiguous sequential assignments of intrinsically disordered proteins by correlating the backbone 15N or 13C' chemical shifts of multiple contiguous residues in highly resolved 3D spectra. J Biomol NMR. 2015;61(2):109–21.
73. Kulminskaya N V., Yoshimura Y, Runager K, Sørensen CS, Bjerring M, Andreasen M, et al. Near-complete 1H, 13C, 15N resonance assignments of dimethylsulfoxide-denatured TGFBIp FAS1-4 A546T. Biomol NMR Assign. 2016 Apr 1;10(1):25–9.
74. Nielsen JT, Mulder FAA. Potenci: Prediction of temperature, neighbor and ph-corrected chemical shifts for intrinsically disordered proteins. J Biomol NMR. 2018 Mar 1;70(3):141–65.
75. Wang Y, Jardetzky O. Investigation of the Neighboring Residue Effects on Protein Chemical Shifts. J Am Chem Soc. 2002 Nov 1;124(47):14075–84.
76. Williamson MP. Secondary-structure dependent chemical shifts in proteins. Biopolymers. 1990 Aug 15;29(10–11):1423–31.
77. Nielsen JT, Mulder FAA. CheSPI: chemical shift secondary structure population inference. J Biomol NMR. 2021 Jul 1;75(6–7):273–91.
78. Cioffi M, Hunter CA, Packer MJ, Spitaleri A. Determination of Protein–Ligand Binding Modes Using Complexation-Induced Changes in ^{1}H NMR Chemical Shift. J Med Chem. 2008 Apr 1;51(8):2512–7.

79. Chung WK, Freed AS, Holstein MA, McCallum SA, Cramer SM. Evaluation of protein adsorption and preferred binding regions in multimodal chromatography using NMR. Proceedings of the National Academy of Sciences. 2010 Sep 28;107(39):16811–6.
80. Macleod GT, Ivannikov M V. Examining Mitochondrial Function at Synapses In Situ. In 2017. p. 279–97.
81. Baminger B, Ludwiczek ML, Kontaxis G, Knapp S, Konrat R. Protein–protein interaction site mapping using NMR-detected mutational scanning. J Biomol NMR. 2007 Jun 20;38(2):133–7.
82. Zuiderweg ERP. Mapping Protein−Protein Interactions in Solution by NMR Spectroscopy. Biochemistry. 2002 Jan 1;41(1):1–7.
83. Williamson MP. Using chemical shift perturbation to characterise ligand binding. Prog Nucl Magn Reson Spectrosc. 2013 Aug;73:1–16.
84. Ishima R. Recent Developments in 15N NMR Relaxation Studies that Probe Protein Backbone Dynamics. In 2011. p. 99–122.
85. Yoshimura Y, Holmberg MA, Kukic P, Andersen CB, Mata-Cabana A, Fabio Falsone S, et al. MOAG-4 promotes the aggregation of α-synuclein by competing with self-protective electrostatic interactions. Journal of Biological Chemistry. 2017 May 19;292(20):8269–78.
86. Milles S, Mercadante D, Aramburu IV, Jensen MR, Banterle N, Koehler C, et al. Plasticity of an Ultrafast Interaction between Nucleoporins and Nuclear Transport Receptors. Cell. 2015 Oct 22;163(3):734–45.
87. Volkov V V., Svergun DI. Uniqueness of *ab initio* shape determination in small-angle scattering. J Appl Crystallogr. 2003 Jun 1;36(3):860–4.
88. Svergun D, Barberato C, Koch MHJ. *CRYSOL* – a Program to Evaluate X-ray Solution Scattering of Biological Macromolecules from Atomic Coordinates. J Appl Crystallogr. 1995 Dec 1;28(6):768–73.
89. Grudinin S, Garkavenko M, Kazennov A. *Pepsi-SAXS* : an adaptive method for rapid and accurate computation of small-angle X-ray scattering profiles. Acta Crystallogr D Struct Biol. 2017 May 1;73(5):449–64.

90. Bernadó P, Mylonas E, Petoukhov M V., Blackledge M, Svergun DI. Structural Characterization of Flexible Proteins Using Small-Angle X-ray Scattering. J Am Chem Soc. 2007 May 1;129(17):5656–64.
91. Pelikan M, Hura G, Hammel M. Structure and flexibility within proteins as identified through small angle X-ray scattering. Gen Physiol Biophys. 2009;28(2):174–89.
92. Bottaro S, Bengtsen T, Lindorff-Larsen K. Integrating Molecular Simulation and Experimental Data: A Bayesian/Maximum Entropy Reweighting Approach. In 2020. p. 219–40.
93. Pesce F, Lindorff-Larsen K. Refining conformational ensembles of flexible proteins against small-angle x-ray scattering data. Biophys J. 2021 Nov;120(22):5124–35.
94. Różycki B, Kim YC, Hummer G. SAXS Ensemble Refinement of ESCRT-III CHMP3 Conformational Transitions. Structure. 2011 Jan;19(1):109–16.
95. Martin EW, Holehouse AS, Peran I, Farag M, Incicco JJ, Bremer A, et al. Valence and patterning of aromatic residues determine the phase behavior of prion-like domains. Science (1979). 2020 Feb 7;367(6478):694–9.
96. González-Magaña A, de Opakua AI, Merino N, Monteiro H, Diercks T, Murciano-Calles J, et al. Double Monoubiquitination Modifies the Molecular Recognition Properties of p15 ^{PAF} Promoting Binding to the Reader Module of Dnmt1. ACS Chem Biol. 2019 Sep 18;acschembio.9b00679.
97. Sagar A, Jeffries CM, Petoukhov M V., Svergun DI, Bernadó P. Comment on the Optimal Parameters to Derive Intrinsically Disordered Protein Conformational Ensembles from Small-Angle X-ray Scattering Data Using the Ensemble Optimization Method. J Chem Theory Comput. 2021 Apr 13;17(4):2014–21.
98. Lira-Navarrete E, de las Rivas M, Compañón I, Pallarés MC, Kong Y, Iglesias-Fernández J, et al. Dynamic interplay between catalytic and lectin domains of GalNAc-transferases modulates protein O-glycosylation. Nat Commun. 2015 May 5;6(1):6937.
99. Grintsevich EE. Remodeling of actin filaments by drebrin a and its implications. In: Advances in Experimental Medicine and Biology. Springer New York LLC; 2017. p. 61–82.

100. Varga S, Kaasen JM, Gáspári Z, Péterfia BF, Mulder FAA. Resonance assignment of the intrinsically disordered actin-binding region of Drebrin. Biomol NMR Assign. 2025 Jun 14;
101. Studier FW. Protein production by auto-induction in high-density shaking cultures. Protein Expr Purif. 2005 May;41(1):207–34.
102. Süveges D, Gáspári Z, Tóth G, Nyitray L. Charged single α-helix: A versatile protein structural motif. Proteins: Structure, Function and Bioinformatics. 2009 Mar;74(4):905–16.
103. Micsonai A, Moussong É, Wien F, Boros E, Vadászi H, Murvai N, et al. BeStSel: Webserver for secondary structure and fold prediction for protein CD spectroscopy. Nucleic Acids Res. 2022 Jul 5;50(W1):W90–8.
104. Vranken WF, Boucher W, Stevens TJ, Fogh RH, Pajon A, Llinas M, et al. The CCPN data model for NMR spectroscopy: Development of a software pipeline. Proteins: Structure, Function, and Bioinformatics. 2005 Jun 6;59(4):687–96.
105. Lee W, Rahimi M, Lee Y, Chiu A. POKY: a software suite for multidimensional NMR and 3D structure calculation of biomolecules. Bioinformatics. 2021 Sep 29;37(18):3041–2.
106. Iii AP, Wright P. Sensitivity Improvement in Proton-Detected Two-Dimensional Heteronuclear Correlation NMR Spectroscopy. Vol. 93, JOURNAL OF MAGNETIC RESONANCE.
107. Grzesiek S, Bax AD. Improved 3D Triple-Resonance NMR Techniques Applied to a 31 kDa Protein. Vol. 96, JOURNAL OF MAGNETIC RESONANCE. 1992.
108. Montelione GT, Lyons BA, Emerson SD, Tashiro M. An efficient triple resonance experiment using carbon-13 isotropic mixing for determining sequence-specific resonance assignments of isotopically-enriched proteins. J Am Chem Soc. 1992 Dec 1;114(27):10974–5.
109. Tossavainen H, Salovaara S, Hellman M, Ihalin R, Permi P. Dispersion from Cα or NH: 4D experiments for backbone resonance assignment of intrinsically disordered proteins. J Biomol NMR. 2020 Mar 1;74(2–3):147–59.
110. Blanchet CE, Spilotros A, Schwemmer F, Graewert MA, Kikhney A, Jeffries CM, et al. Versatile sample environments and automation for biological solution X-ray

scattering experiments at the P12 beamline (PETRA III, DESY). J Appl Crystallogr. 2015 Apr 1;48(2):431–43.

111. Franke D, Kikhney AG, Svergun DI. Automated acquisition and analysis of small angle X-ray scattering data. Nucl Instrum Methods Phys Res A. 2012 Oct;689:52–9.
112. Franke D, Jeffries CM, Svergun DI. Correlation Map, a goodness-of-fit test for one-dimensional X-ray scattering spectra. Nat Methods. 2015 May 6;12(5):419–22.
113. Manalastas-Cantos K, Konarev P V., Hajizadeh NR, Kikhney AG, Petoukhov M V., Molodenskiy DS, et al. *ATSAS 3.0* : expanded functionality and new tools for small-angle scattering data analysis. J Appl Crystallogr. 2021 Feb 1;54(1):343–55.
114. Guinier A. La diffraction des rayons X aux très petits angles : application à l'étude de phénomènes ultramicroscopiques. Ann Phys (Paris). 1939 Apr 28;11(12):161–237.
115. Svergun DI. Determination of the regularization parameter in indirect-transform methods using perceptual criteria. J Appl Crystallogr. 1992 Aug 1;25(4):495–503.
116. Hajizadeh NR, Franke D, Jeffries CM, Svergun DI. Consensus Bayesian assessment of protein molecular mass from solution X-ray scattering data. Sci Rep. 2018 May 8;8(1):7204.
117. Receveur-Brechot V, Durand D. How Random are Intrinsically Disordered Proteins? A Small Angle Scattering Perspective. Curr Protein Pept Sci. 2012 Feb 1;13(1):55–75.
118. Franke D, Svergun DI. *DAMMIF* , a program for rapid *ab-initio* shape determination in small-angle scattering. J Appl Crystallogr. 2009 Apr 1;42(2):342–6.
119. Volkov V V., Svergun DI. Uniqueness of *ab initio* shape determination in small-angle scattering. J Appl Crystallogr. 2003 Jun 1;36(3):860–4.
120. Svergun DI. Restoring Low Resolution Structure of Biological Macromolecules from Solution Scattering Using Simulated Annealing. Biophys J. 1999 Jun;76(6):2879–86.
121. Schuck P. Size-Distribution Analysis of Macromolecules by Sedimentation Velocity Ultracentrifugation and Lamm Equation Modeling. Biophys J. 2000 Mar;78(3):1606–19.
122. Jabs A, Weiss MS, Hilgenfeld R. Non-proline Cis peptide bonds in proteins. J Mol Biol. 1999 Feb;286(1):291–304.

123. Pronk S, Páll S, Schulz R, Larsson P, Bjelkmar P, Apostolov R, et al. GROMACS 4.5: A high-throughput and highly parallel open source molecular simulation toolkit. Bioinformatics. 2013 Apr;29(7):845–54.
124. Lindorff-Larsen K, Piana S, Palmo K, Maragakis P, Klepeis JL, Dror RO, et al. Improved side-chain torsion potentials for the Amber ff99SB protein force field. Proteins: Structure, Function and Bioinformatics. 2010 Jun;78(8):1950–8.
125. Dudola D, Kovács B, Gáspári Z. CoNSEnsX+ Webserver for the Analysis of Protein Structural Ensembles Reflecting Experimentally Determined Internal Dynamics. J Chem Inf Model. 2017 Aug 28;57(8):1728–34.
126. Berendsen HJC, Grigera JR, Straatsma TP. The missing term in effective pair potentials. J Phys Chem. 1987 Nov 1;91(24):6269–71.
127. Neal S, Nip AM, Zhang H, Wishart DS. Rapid and accurate calculation of protein 1H, 13C and 15N chemical shifts. J Biomol NMR. 2003 Jul;26(3):215–40.
128. Koradi R, Billeter M, Wüthrich K. MOLMOL: A program for display and analysis of macromolecular structures. J Mol Graph. 1996 Feb;14(1):51–5.
129. Pettersen EF, Goddard TD, Huang CC, Couch GS, Greenblatt DM, Meng EC, et al. UCSF Chimera—A visualization system for exploratory research and analysis. J Comput Chem. 2004 Oct;25(13):1605–12.
130. Carter P, Andersen CAF, Rost B. DSSPcont: Continuous secondary structure assignments for proteins. Nucleic Acids Res. 2003 Jul 1;31(13):3293–5.
131. Crooks GE, Hon G, Chandonia JM, Brenner SE. WebLogo: A Sequence Logo Generator: Figure 1. Genome Res. 2004 Jun;14(6):1188–90.
132. Barlow DJ, Thornton JM. Ion-pairs in proteins. J Mol Biol. 1983 Aug;168(4):867–85.
133. Donald JE, Kulp DW, DeGrado WF. Salt bridges: Geometrically specific, designable interactions. Proteins: Structure, Function, and Bioinformatics. 2011 Mar 5;79(3):898–915.
134. Gallivan JP, Dougherty DA. Cation-π interactions in structural biology. Proceedings of the National Academy of Sciences. 1999 Aug 17;96(17):9459–64.
135. Markley JL, Bax A, Arata Y, Hilbers CW, Kaptein R, Sykes BD, et al. Recommendations for the presentation of NMR structures of proteins and nucleic acids. IUPAC-IUBMB-IUPAB Inter-Union Task Group on the Standardization of

Data Bases of Protein and Nucleic Acid Structures Determined by NMR Spectroscopy. J Biomol NMR. 1998;12(1):1–23.

136. Svergun DI, Koch MHJ. Small-angle scattering studies of biological macromolecules in solution. Reports on Progress in Physics. 2003 Oct 1;66(10):1735–82.
137. Franke D, Kikhney AG, Svergun DI. Automated acquisition and analysis of small angle X-ray scattering data. Nucl Instrum Methods Phys Res A. 2012 Oct;689:52–9.
138. Hajizadeh NR, Franke D, Svergun DI. Integrated beamline control and data acquisition for small-angle X-ray scattering at the P12 BioSAXS beamline at PETRAIII storage ring DESY. J Synchrotron Radiat. 2018 May 1;25(3):906–14.
139. Blanchet CE, Spilotros A, Schwemmer F, Graewert MA, Kikhney A, Jeffries CM, et al. Versatile sample environments and automation for biological solution X-ray scattering experiments at the P12 beamline (PETRA III, DESY). J Appl Crystallogr. 2015 Apr 1;48(2):431–43.
140. Manalastas-Cantos K, Konarev P V., Hajizadeh NR, Kikhney AG, Petoukhov M V., Molodenskiy DS, et al. *ATSAS 3.0* : expanded functionality and new tools for small-angle scattering data analysis. J Appl Crystallogr. 2021 Feb 1;54(1):343–55.
141. Svergun DI. Determination of the regularization parameter in indirect-transform methods using perceptual criteria. J Appl Crystallogr. 1992 Aug 1;25(4):495–503.
142. Hajizadeh NR, Franke D, Jeffries CM, Svergun DI. Consensus Bayesian assessment of protein molecular mass from solution X-ray scattering data. Sci Rep. 2018 May 8;8(1):7204.
143. Franke D, Svergun DI. *DAMMIF* , a program for rapid *ab-initio* shape determination in small-angle scattering. J Appl Crystallogr. 2009 Apr 1;42(2):342–6.
144. Svergun DI. Restoring Low Resolution Structure of Biological Macromolecules from Solution Scattering Using Simulated Annealing. Biophys J. 1999 Jun;76(6):2879–86.
145. Volkov V V., Svergun DI. Uniqueness of *ab initio* shape determination in small-angle scattering. J Appl Crystallogr. 2003 Jun 1;36(3):860–4.
146. Günther P. Small-angle X-ray scattering. Graber O, Kratky O, editors. London: Academic Press; 1982. 17–51 p.

147. Johansen D, Trewhella J, Goldenberg DP. Fractal dimension of an intrinsically disordered protein: Small-angle X-ray scattering and computational study of the bacteriophage λ N protein. Protein Science. 2011 Dec 26;20(12):1955–70.
148. Wang Y, Jardetzky O. Probability-based protein secondary structure identification using combined NMR chemical-shift data. Protein Science. 2002 Apr;11(4):852–61.
149. Baker EG, Bartlett GJ, Crump MP, Sessions RB, Linden N, Faul CFJ, et al. Local and macroscopic electrostatic interactions in single α-helices. Nat Chem Biol. 2015;11(3):221–8.
150. Bhattacharyya R, Samanta U, Chakrabarti P. Aromatic-aromatic interactions in and around α-helices [Internet]. Vol. 15, Protein Engineering. 2002. Available from: http://www.rcsb.org
151. Yamada S. The Cation–π Interaction. Singapore: Springer Nature Singapore; 2022. 44–47 p.
152. Calinsky R, Levy Y. Histidine in Proteins: pH-Dependent Interplay between π–π, Cation–π, and CH–π Interactions. J Chem Theory Comput. 2024 Aug 13;20(15):6930–45.
153. Dass R, Mulder FAA, Nielsen JT. ODiNPred: comprehensive prediction of protein order and disorder. Sci Rep. 2020 Sep 8;10(1):14780.
154. Lin S, Hu G, Zhang M, Li J. ATP Binding and Inhibition of Intrinsically Disordered Protein Interactions. Langmuir. 2025 Feb 11;41(5):3315–24.
155. Mulder FAA. Fuzzy and fast nuclear transport. Journal of Biological Chemistry. 2018 Mar;293(12):4564–5.
156. Ruskamo S, Chukhlieb M, Vahokoski J, Bhargav SP, Liang F, Kursula I, et al. Juxtanodin is an intrinsically disordered F-actin-binding protein. Sci Rep. 2012 Nov 29;2(1):899.
157. Xue B, Robinson RC. Actin-Induced Structure in the Beta-Thymosin Family of Intrinsically Disordered Proteins. In 2016. p. 55–71.
158. Urbanek A, Morató A, Allemand F, Delaforge E, Fournet A, Popovic M, et al. A General Strategy to Access Structural Information at Atomic Resolution in Polyglutamine Homorepeats. Angewandte Chemie. 2018 Mar 26;130(14):3660–3.

159. Urbanek A, Popovic M, Morató A, Estaña A, Elena-Real CA, Mier P, et al. Flanking Regions Determine the Structure of the Poly-Glutamine in Huntingtin through Mechanisms Common among Glutamine-Rich Human Proteins. Structure. 2020 Jul 7;28(7):733-746.e5.

Appendix

Data availibility

Nuclear Magnetic Resonance data for the Drebrin SAH structural ensemble reported in this article have been deposited at the Biological Magnetic Resonance Data Bank, under deposition ID:52729. The corresponding Small Angle X-ray Scattering data have been deposited to Small Angle Scattering Biological Data Bank with the ID SASDVV6. Fitting data for the ensemble is available in the Protein Ensemble Database under deposition ID: PED00524.The authors declare that the data supporting the findings of this study are available within the dissertation and its appendix. Should any raw data files be needed in another format they are available from the corresponding author upon reasonable request. The modified version of CoNSEnsX+ is available at: https://github.com/PPKE-Bioinf/consensx.itk.ppke.hu (source code) and at https://hub.docker.com/repository/docker/ppkebioinf/consensx/general (dockerized version). The assignments obtained for D233 have been deposited in the BMRB with the access number 52895.

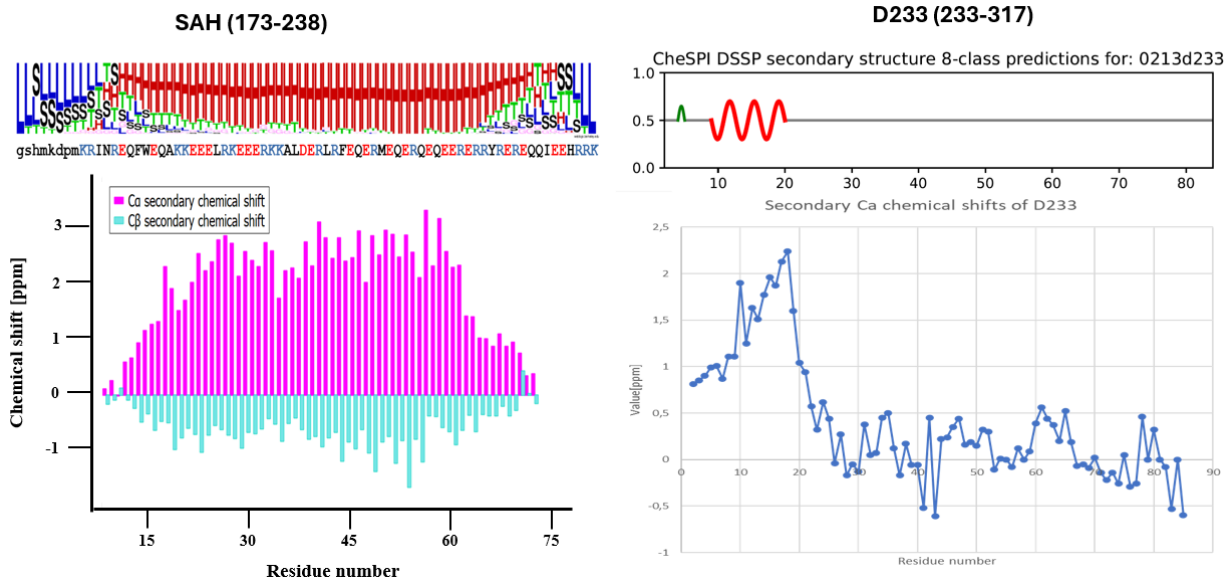

Figure A1: Secondary chemical shifts of the Drebrin-SAH and D233 constructs.
Decrease in helicity values near to the C-terminus of D233 and both C-and N-terminus of SAH is observable.

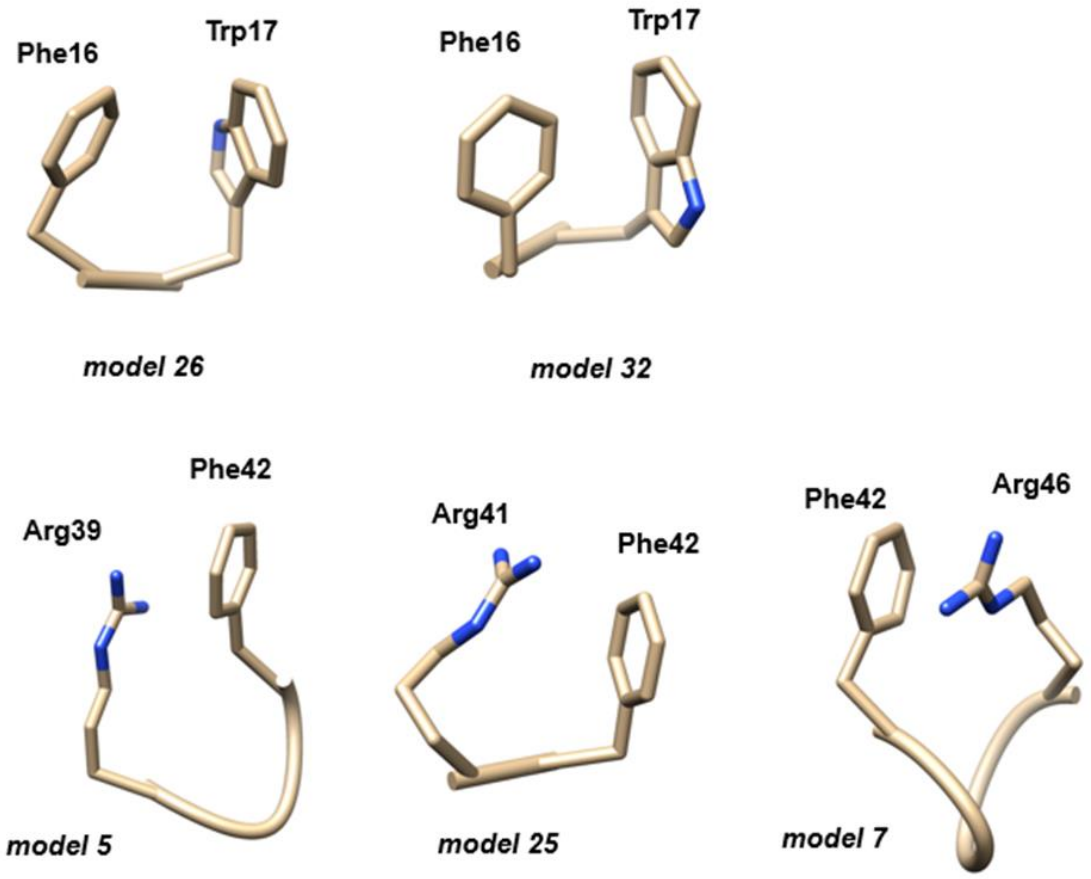

Figure A2. Interactions between the aromatic side chains of Phe16 and Trp17.
A parallel arrangement suggesting the presence of a pi:pi interaction, as well as an edge-to-face interaction. Putative cation:pi interactions formed by Phe42 with Arg39, Arg41 and Arg46.

Table A1: Correspondence of different ensembles to selected experimental data

Ensemble	No. of conformers	RMSD to CA chemical shift	Correlation with CA secondary chemical shift	RMSD to CB chemical shift	Correlation with CB secondary chemical shift	SAXS Chi2	RMSD to HA chemical shift	Correlation with HA secondary chemical shift
Primary pool 1	5000	0,67	0,79	0,62	0,21	3,01	0,08	0,52
Primary pool 2	5000	0,66	0,79	0,62	0,20	2,95	0,08	0,51
Primary pool 3	5000	0,66	0,79	0,62	0,21	3,01	0,08	0,53
Primary pool 4	5000	0,67	0,79	0,62	0,20	3,03	0,08	0,52
Primary pool 5	5000	0,66	0,79	0,63	0,20	2,95	0,08	0,53
Selected from primary 1 (CA+CB chem. shifts+SAXS)	37	0,31	0,95	0,38	0,56	1,07	0,12	0,61
Selected from primary 2 (CA+CB chem. shifts+SAXS)	30	0,31	0,95	0,38	0,55	1,08	0,12	0,63
Selected from primary 3 (CA+CB chem. shifts+SAXS)	22	0,30	0,95	0,40	0,50	1,08	0,12	0,58
Selected from primary 4 (CA+CB chem. shifts+SAXS)	26	0,34	0,94	0,40	0,46	1,05	0,10	0,67
Selected from primary 5 (CA+CB chem. shifts+SAXS)	39	0,31	0,96	0,40	0,52	1,06	0,11	0,63
Selected from primary 1 (CA+CB chem. shifts)	26	0,21	0,98	0,35	0,61	2,22	0,13	0,58
Selected from primary 2 (CA+CB chem. shifts)	56	0,23	0,98	0,35	0,61	2,55	0,12	0,69
Selected from primary 3 (CA+CB chem. shifts)	35	0,21	0,98	0,35	0,62	2,63	0,12	0,64
Selected from primary 4 (CA+CB chem. shifts)	45	0,22	0,98	0,35	0,62	2,31	0,12	0,68
Selected from primary 5 (CA+CB chem. shifts)	41	0,21	0,98	0,37	0,60	2,60	0,11	0,69
Selected from primary 1 (SAXS)	7	0,80	0,68	0,82	0,18	1,00	0,15	0,45
Selected from primary 2 (SAXS)	8	0,89	0,57	0,83	0,11	1,01	0,14	0,31
Selected from primary 3 (SAXS)	4	0,87	0,66	0,83	0,05	1,02	0,13	0,39
Selected from primary 4 (SAXS)	14	0,77	0,70	0,72	0,25	1,00	0,12	0,51
Selected from primary 5 (SAXS)	2	1,15	0,46	0,93	0,13	1,01	0,22	-0,08
Secondary pool	5043	0,36	0,93	0,39	0,53	1,16	0,11	0,65
Final ensemble selected from the secondary pool (CA+CB chem. shifts+SAXS)	*60*	*0,22*	*0,98*	*0,31*	*0,68*	*1,07*	*0,12*	*0,65*

Table A2. Experimental and calculated chemical shifts for the final ensemble

Residue nr.	C secondary		C		CA secondary		CA		CB secondary		CB		H secondary		H		HA secondary		HA		N secondary		N	
	Exp.	Calc	Exp.	Calc	Exp.	Calc	Exp.	Calc	Exp.	Calc	Exp.	Calc	Exp.	Calc	Exp.	Calc	Exp.	Calc	Exp.	Calc	Exp.	Calc	Exp.	Calc
9	-0,12	0,40	176,36	176,88	0,25	0,34	56,43	56,52	0,04	0,10	32,87	32,93	-0,40	-0,24	7,99	8,15	0,07	0,03	4,27	4,23	-1,08	-3,33	121,61	119,37
10	0,13	0,36	176,27	176,50	0,18	0,47	56,33	56,62	0,07	-0,07	30,75	30,61	-0,10	-0,29	8,23	8,04	0,09	-0,06	4,30	4,14	-0,02	-2,67	122,41	119,76
11	0,07	-0,22	175,87	175,58	-0,01	0,33	61,20	61,54	0,34	0,00	38,85	38,51	-0,04	-0,52	8,15	7,67	0,11	-0,03	4,15	4,01	-0,54	-5,63	121,66	116,57
12	0,23	0,50	175,39	175,66	0,88	1,33	53,77	54,22	0,10	0,53	38,83	39,25	-0,10	-0,33	8,48	8,25	0,09	-0,05	4,71	4,57	0,00	-4,34	122,81	118,47
13	0,41	0,55	176,68	176,82	0,78	0,84	57,09	57,15	0,03	0,20	30,58	30,75	0,04	-0,41	8,39	7,94	-0,03	-0,02	4,20	4,21	0,12	-4,12	122,01	117,76
14	1,06	1,20	177,39	177,53	1,30	1,33	57,88	57,91	-0,48	-0,48	29,71	29,71	-0,04	-0,34	8,50	8,20	-0,06	-0,09	4,12	4,09	-1,82	-4,45	120,77	118,14
15	1,16	1,26	176,75	176,85	1,21	1,38	56,97	57,14	-0,35	-0,24	29,06	29,17	-0,06	-0,31	8,24	7,98	0,01	-0,06	4,16	4,09	-1,11	-2,67	119,86	118,29
16	1,14	1,13	176,66	176,65	1,30	1,35	59,16	59,21	-0,73	-0,57	38,93	39,10	-0,22	-0,35	8,14	8,01	-0,01	-0,15	4,47	4,33	-1,11	-2,64	120,46	118,92
17	3,97	3,81	177,34	177,19	1,23	1,56	58,50	58,82	-0,18	0,07	29,32	29,57	0,18	0,25	7,97	8,04	0,03	-0,08	4,55	4,44	-1,40	0,53	121,47	123,40
18	1,83	2,03	177,94	178,14	2,55	2,13	59,12	58,70	-0,33	-0,71	29,85	29,48	0,43	0,52	8,16	8,25	-0,01	0,02	4,01	4,03	-0,22	-2,74	121,26	118,73
19	1,60	1,80	177,26	177,46	2,06	2,10	57,88	57,93	-0,96	-0,44	28,45	28,97	-0,28	-0,33	8,10	8,05	-0,10	-0,15	4,06	4,01	-0,98	-3,88	120,47	117,56
20	2,03	1,26	179,77	179,00	1,67	1,52	54,25	54,11	-0,65	-0,49	18,42	18,57	-0,17	-0,58	8,16	7,75	-0,05	-0,19	4,15	4,02	-2,61	-4,27	123,06	121,41
21	1,48	1,72	178,25	178,49	1,65	1,84	58,08	58,27	-0,39	-0,46	32,42	32,35	-0,27	-0,32	7,99	7,94	-0,04	-0,19	4,14	3,99	-1,08	-3,81	119,70	116,98
22	2,09	1,56	178,69	178,17	1,96	2,18	58,50	58,72	-0,51	-0,36	32,37	32,52	-0,39	-0,49	7,99	7,89	-0,05	-0,12	4,15	4,08	-1,58	-3,44	120,98	119,12
23	2,28	1,72	178,79	178,23	2,52	2,10	59,29	58,87	-0,92	-0,61	29,27	29,57	-0,11	-0,34	8,35	8,13	-0,04	-0,16	4,15	4,03	-2,12	-3,22	119,86	118,76
24	1,93	1,54	178,52	178,13	2,29	1,94	59,04	58,69	-0,50	-0,47	29,67	29,70	-0,29	-0,38	8,17	8,08	-0,02	-0,19	4,15	3,98	-1,40	-3,54	120,50	118,36
25	2,85	1,96	179,33	178,44	2,42	2,12	59,06	58,76	-0,33	-0,31	29,72	29,75	-0,29	-0,31	8,10	8,08	-0,06	-0,13	4,09	4,02	-1,78	-2,81	119,82	118,78
26	2,10	1,61	179,48	178,99	3,02	2,51	58,19	57,68	-0,51	-0,25	41,63	41,89	-0,14	-0,38	8,08	7,84	-0,02	-0,17	4,18	4,03	-1,91	-3,53	121,13	119,50
27	2,83	2,23	179,02	178,42	2,99	2,73	59,02	58,75	-0,58	-0,58	30,00	30,00	-0,19	-0,30	8,09	7,98	-0,04	-0,17	4,15	4,02	-1,74	-4,23	120,45	117,96
28	2,88	1,92	179,35	178,39	2,87	2,75	59,24	59,12	-0,65	-0,76	32,30	32,19	-0,31	-0,41	8,15	8,04	-0,14	-0,22	4,09	4,01	-3,48	-4,61	119,68	118,56
29	2,21	1,70	178,71	178,20	2,11	2,10	58,88	58,87	-0,82	-0,56	29,37	29,63	-0,37	-0,39	8,09	8,07	0,05	-0,17	4,24	4,02	-1,03	-3,03	120,95	118,95
30	2,82	1,84	179,41	178,43	2,54	2,33	59,29	59,08	-0,47	-0,52	29,70	29,65	-0,21	-0,24	8,25	8,23	-0,05	-0,17	4,12	4,00	-1,29	-2,88	120,61	119,01
31	2,73	2,23	179,20	178,70	2,58	2,41	59,14	58,97	-0,51	-0,55	29,64	29,61	-0,21	-0,27	8,23	8,17	-0,10	-0,14	4,06	4,02	-2,15	-3,34	119,78	118,59
32	2,62	2,01	178,89	178,28	2,41	2,56	58,53	58,67	-0,52	-0,34	30,08	30,26	-0,23	-0,44	8,12	7,91	-0,09	-0,18	4,09	4,00	-1,29	-4,67	121,29	117,91
33	1,98	2,37	178,44	178,82	2,88	2,63	59,18	58,93	-0,35	-0,57	32,56	32,34	-0,31	-0,38	8,11	8,04	-0,07	-0,18	4,15	4,04	-3,02	-4,69	120,31	118,64
34	2,18	2,30	178,47	178,59	2,54	2,82	58,96	59,24	-0,26	-0,83	32,58	32,01	-0,31	-0,17	8,03	8,17	0,01	-0,20	4,17	3,97	-2,79	-3,50	119,87	119,16
35	2,47	1,27	180,16	178,96	1,74	1,96	54,35	54,57	-0,62	-0,54	18,33	18,41	-0,37	-0,30	7,88	7,95	0,07	-0,09	4,24	4,08	-3,38	-4,40	121,44	120,42
36	1,26	1,41	178,51	178,66	2,21	2,10	57,54	57,43	-0,30	0,05	41,86	42,20	-0,22	-0,25	7,95	7,92	0,00	-0,09	4,20	4,11	0,12	-3,34	120,98	117,52
37	2,47	1,72	178,84	178,09	2,37	2,59	56,71	56,94	-0,26	-0,12	40,75	40,89	-0,02	-0,16	8,29	8,15	-0,04	-0,09	4,45	4,40	-0,60	-2,49	120,34	118,46
38	1,72	2,20	178,28	178,76	2,42	2,33	59,10	59,02	-0,46	-0,51	29,63	29,58	-0,12	-0,17	8,23	8,17	0,03	-0,17	4,21	4,01	-0,85	-2,02	120,53	119,37
39	2,61	2,07	178,79	178,25	3,06	2,97	59,14	59,04	-0,80	-0,41	29,72	30,11	-0,31	-0,33	8,01	7,99	0,04	-0,16	4,21	4,01	-1,72	-3,80	120,40	118,32
40	2,41	1,64	179,58	178,80	2,64	2,53	57,67	57,56	-0,70	-0,38	41,52	41,84	-0,07	-0,32	8,23	7,98	-0,05	-0,17	4,19	4,07	-3,77	-4,69	119,95	119,03
41	2,69	2,38	178,50	178,20	3,31	3,26	59,23	59,19	-0,71	-0,49	29,86	30,09	-0,19	-0,28	8,01	7,93	-0,02	-0,16	4,12	3,98	-1,44	-3,53	120,20	118,11
42	2,57	1,19	178,19	176,81	2,69	2,85	60,58	60,74	-0,87	-0,51	38,82	39,17	-0,13	0,03	8,21	8,37	-0,12	-0,26	4,44	4,30	-2,07	-2,59	119,88	119,35
43	2,96	2,69	178,86	178,59	2,69	2,70	59,08	59,09	-0,60	-0,86	29,69	29,42	0,01	-0,12	8,38	8,25	-0,02	-0,20	4,12	3,94	-2,98	-4,23	119,94	118,69
44	2,71	2,17	178,68	178,15	2,96	2,85	58,90	58,79	-1,19	-0,64	28,26	28,82	-0,16	-0,32	8,26	8,10	-0,11	-0,19	4,09	4,01	-1,48	-3,11	119,87	118,24
45	2,70	2,44	179,05	178,79	2,81	2,48	59,33	59,00	-0,85	-0,51	29,36	29,69	-0,17	-0,36	8,32	8,13	-0,12	-0,20	4,08	4,00	-1,94	-2,86	120,46	119,54
46	2,18	1,65	178,70	178,17	2,57	2,66	58,77	58,86	-0,64	-0,38	29,73	29,99	-0,22	-0,57	8,12	7,77	-0,11	-0,21	4,06	3,96	-1,52	-4,45	120,85	117,92
47	2,79	1,83	178,99	178,03	3,15	2,79	58,70	58,34	-0,47	-0,67	32,25	32,05	-0,31	-0,38	8,14	8,06	-0,21	-0,36	4,21	4,05	-2,86	-3,38	118,95	118,43
48	2,23	2,26	178,69	178,72	2,30	2,53	58,88	59,11	-0,98	-0,42	29,11	29,67	-0,36	-0,39	8,13	8,10	0,05	-0,17	4,22	3,99	-1,24	-3,16	120,85	118,93
49	2,74	2,09	178,71	178,06	2,96	2,93	58,90	58,87	-1,37	-0,67	28,09	28,78	-0,26	-0,43	8,16	7,98	-0,11	-0,19	4,09	4,01	-0,84	-2,80	120,51	118,55
50	2,76	2,43	179,11	178,78	2,80	2,54	59,32	59,06	-0,84	-0,64	29,37	29,57	-0,18	-0,34	8,31	8,15	-0,10	-0,21	4,10	3,98	-2,55	-2,64	119,85	119,76
51	2,66	2,14	178,90	178,38	3,13	3,11	59,29	59,27	-0,60	-0,59	29,98	29,99	-0,28	-0,43	8,11	7,96	-0,03	-0,20	4,12	3,95	-1,56	-3,91	120,87	118,51
52	3,12	2,21	178,88	177,97	3,15	2,93	58,95	58,73	-1,30	-0,75	28,24	28,79	-0,28	-0,39	8,21	8,11	-0,15	-0,22	4,09	4,03	-2,55	-3,73	119,48	118,31
53	2,82	2,06	179,24	178,48	2,67	2,32	59,35	59,00	-0,81	-0,51	29,35	29,66	-0,20	-0,41	8,31	8,11	-0,06	-0,16	4,11	4,01	-2,03	-2,53	120,35	119,85
54	2,21	2,10	178,18	178,07	2,92	2,78	58,86	58,72	-1,65	-0,61	27,81	28,84	-0,23	-0,36	8,19	8,06	-0,15	-0,15	4,05	4,05	-0,94	-2,70	120,41	118,65
55	2,91	2,00	179,38	178,46	2,63	2,44	59,33	59,14	-0,75	-0,57	29,48	29,66	-0,19	-0,30	8,33	8,22	-0,09	-0,22	4,12	3,99	-2,21	-2,38	120,16	119,99
56	1,97	2,32	178,44	178,78	2,37	2,45	58,93	59,01	-1,09	-0,59	29,06	29,56	-0,33	-0,37	8,11	8,07	0,02	-0,13	4,18	4,03	-1,62	-3,27	120,31	118,66
57	2,87	1,89	179,16	178,17	3,48	2,98	59,67	59,17	-0,31	-0,56	30,33	30,08	-0,32	-0,40	8,07	7,99	-0,21	-0,28	3,98	3,91	-2,26	-4,27	120,15	118,15
58	2,48	2,36	178,73	178,62	2,65	2,49	59,07	58,92	-0,33	-0,52	29,90	29,72	-0,34	-0,40	8,18	8,11	-0,08	-0,11	4,12	4,09	-3,52	-4,51	119,09	118,10
59	2,47	2,24	178,63	178,40	3,40	3,18	59,40	59,18	-0,46	-0,47	30,16	30,15	-0,26	-0,42	8,11	7,95	-0,13	-0,19	4,04	3,98	-1,91	-4,35	120,54	118,10
60	3,01	2,06	178,74	177,79	2,80	2,81	58,77	58,78	-0,58	-0,54	30,09	30,13	-0,25	-0,38	8,14	8,01	-0,09	-0,14	4,10	4,05	-4,23	-5,30	118,58	117,51
61	2,24	1,86	177,65	177,28	2,67	2,43	60,20	59,97	-0,82	-0,16	37,94	38,59	-0,18	-0,33	8,06	7,91	-0,11	-0,20	4,37	4,29	-2,10	-4,19	119,97	117,88
62	2,57	2,05	178,25	177,74	2,58	2,52	58,35	58,29	-0,36	-0,48	30,41	30,29	-0,03	-0,15	8,14	8,02	-0,07	-0,20	4,13	4,00	-4,05	-4,96	119,87	118,95
63	1,66	1,75	177,91	178,00	1,79	1,83	58,21	58,25	-0,36	-0,48	29,87	29,75	-0,35	-0,48	8,17	8,04	-0,06	-0,11	4,14	4,09	-3,18	-4,54	119,43	118,07
64	1,26	0,97	177,55	177,26	1,53	1,57	57,72	57,76	-0,51	-0,21	30,13	30,43	-0,51	-0,69	7,88	7,70	-0,01	-0,06	4,18	4,12	-2,64	-5,07	119,77	117,34
65	1,25	1,47	177,58	177,80	1,25	1,26	57,83	57,84	-0,28	-0,19	29,91	30,00	-0,40	-0,49	8,14	8,05	-0,06	-0,05	4,12	4,13	-2,72	-4,46	119,87	118,13
66	0,77	0,53	176,70	176,46	1,06	1,23	56,97	57,14	-0,30	-0,43	29,09	28,96	-0,29	-0,43	8,13	7,99	0,06	-0,12	4,23	4,05	-1,99	-3,63	119,37	117,74
67	1,02	0,99	176,82	176,79	0,92	1,04	56,76	56,88	-0,47	-0,38	29,07	29,15	-0,26	-0,44	8,15	7,97	0,04	-0,04	4,28	4,20	-1,45	-3,37	120,31	118,38
68	0,81	0,08	177,05	176,32	1,03	1,02	62,33	62,32	0,00	-0,14	38,56	38,42	-0,10	-0,54	8,07	7,63	-0,03	-0,01	4,03	4,05	-0,79	-4,12	121,32	117,99
69	0,66	0,25	177,24	176,83	0,93	0,87	57,42	57,37	-0,19	0,04	29,99	30,22	-0,23	-0,42	8,31	8,12	-0,04	0,03	4,19	4,26	-1,27	-5,84	123,60	119,03
70	0,58	0,07	177,00	176,48	1,06	1,00	57,63	57,57	-0,10	0,11	30,05	30,26	0,01	-0,16	8,35	8,18	0,00	0,12	4,12	4,23	-0,60	-3,62	121,17	118,15
71	0,48	-0,16	175,17	174,53	0,47	0,43	56,35	56,31	0,17	0,46	29,82	30,10	-0,22	-0,36	8,22	8,08	0,12	-0,05	4,64	4,47	-1,75	-2,76	118,34	117,33
72	0,25	0,41	176,20	176,36	0,57	0,53	56,47	56,43	0,17	-0,03	30,81	30,61	-0,25	-0,49	8,08	7,85	0,11	0,01	4,31	4,22	-1,74	-4,30	121,24	118,68
73	-0,67	0,04	175,39	176,09	0,45	0,22	56,42	56,19	0,09	0,20	30,77	30,88	-0,19	-0,43	8,24	8,00	0,10	0,02	4,32	4,24	-0,62	-5,52	122,64	117,75
74	-1,59	-1,07	175,39	175,91									-0,52	-0,33	7,95	8,14					4,85	-1,78	128,11	121,48

Table A3. Radius of gyration and end-to-end distance of the models in the final ensemble

MODEL	Radius of gyration [A]	End-to-end distance (CA1-CA72) [A]
1	26,23	58,38
2	30,90	86,64
3	25,83	77,02
4	32,50	99,29
5	21,75	61,76
6	32,32	96,40
7	24,71	53,63
8	31,56	97,63
9	31,40	91,69
10	31,47	91,82
11	31,88	104,16
12	31,77	104,85
13	30,57	93,69
14	28,60	73,91
15	30,97	102,80
16	30,82	103,13
17	27,59	58,92
18	32,16	104,27
19	32,18	104,01
20	31,21	98,93
21	31,20	98,66
22	28,92	69,83
23	27,14	72,27
24	26,86	72,33
25	31,97	78,56
26	27,21	82,66
27	32,21	95,92
28	29,07	71,45
29	31,07	94,17
30	28,88	65,44
31	28,89	65,15
32	28,31	77,49
33	30,59	91,31
34	28,42	83,62
35	32,01	97,09
36	32,04	97,08
37	24,77	57,48
38	26,11	63,71
39	26,13	63,77
40	32,12	95,85
41	32,10	83,68
42	32,14	83,25
43	27,31	65,33
44	27,10	65,05
45	29,98	86,17
46	31,81	101,25
47	31,80	101,44
48	31,88	105,18
49	29,95	86,94
50	27,72	77,67
51	28,42	73,95
52	25,46	58,88
53	25,49	58,66
54	30,80	95,72
55	30,98	96,14
56	23,93	67,89
57	28,48	69,34
58	28,45	68,86
59	33,01	110,14
60	29,22	93,98

Table A4. Averaged DSSPCont results for the final ensemble

Residue		Secondary structure state probability (DSSP code)							
position	type	G	H	I	T	B	E	S	L
1	G	0	0	0	0	0	0	0	100
2	S	0	0	0	11	0	0	0	89
3	H	0	0	0	13	0	0	47	40
4	M	0	0	0	10	0	0	37	53
5	K	0	0	0	7	0	0	42	51
6	D	0	0	0	1	0	0	31	68
7	P	3	0	0	9	0	0	25	63
8	M	3	0	0	16	0	0	24	57
9	K	5	1	0	14	0	0	23	57
10	R	4	5	0	26	0	0	26	39
11	I	6	14	0	31	0	0	15	34
12	N	6	26	0	26	0	0	24	17
13	R	6	31	0	20	0	0	32	11
14	E	9	41	0	24	0	0	17	9
15	Q	7	46	0	22	0	0	10	15
16	F	5	53	0	12	0	0	10	20
17	W	2	66	0	9	0	0	12	11
18	E	2	70	0	17	0	0	10	2
19	Q	1	69	0	17	0	0	7	5
20	A	3	70	0	17	0	0	3	8
21	K	2	72	0	17	0	0	4	5
22	K	3	80	0	11	0	0	2	5
23	E	4	84	0	10	0	0	3	0
24	E	2	79	0	16	0	0	2	2
25	E	5	81	0	9	0	0	1	3
26	L	4	85	0	9	0	0	2	0
27	R	6	83	0	10	0	0	1	0
28	K	2	89	0	10	0	0	0	0
29	E	2	88	0	8	0	0	0	2
30	E	3	92	0	5	0	0	0	1
31	E	5	93	0	3	0	0	0	0
32	R	7	87	0	5	0	0	1	0
33	K	6	83	0	9	0	0	1	0
34	K	7	85	0	8	0	0	0	0
35	A	6	86	0	9	0	0	0	0
36	L	2	83	0	15	0	0	0	0
37	D	1	92	0	5	0	0	0	2
38	E	3	94	0	3	0	0	0	0
39	R	3	95	0	2	0	0	0	0
40	L	3	91	0	3	0	0	0	3
41	R	0	95	0	4	0	0	0	0
42	F	0	91	0	8	0	0	0	0
43	E	0	93	0	7	0	0	0	0
44	Q	2	97	0	1	0	0	0	0
45	E	2	94	0	4	0	0	0	0
46	R	2	92	0	4	0	0	0	2
47	M	1	95	0	4	0	0	0	0
48	E	1	97	0	3	0	0	0	0
49	Q	0	100	0	0	0	0	0	0
50	E	0	100	0	0	0	0	0	0
51	R	0	100	0	0	0	0	0	0
52	Q	0	100	0	0	0	0	0	0
53	E	0	92	0	8	0	0	0	0
54	Q	0	94	0	5	0	0	0	0
55	E	0	98	0	2	0	0	0	0
56	E	0	98	0	2	0	0	0	0
57	R	0	97	0	3	0	0	0	0
58	E	0	91	0	9	0	0	0	0
59	R	0	92	0	6	0	0	1	1
60	R	1	84	0	6	0	0	3	6
61	Y	3	74	0	14	0	0	5	4
62	R	4	67	0	15	0	0	4	10
63	E	5	58	0	25	0	0	10	2
64	R	9	55	0	25	0	0	7	4
65	E	9	49	0	23	0	0	11	9
66	Q	8	34	0	22	0	0	15	20
67	Q	8	30	0	32	0	0	5	24
68	I	6	28	0	24	0	0	20	22
69	E	7	26	0	21	1	0	19	26
70	E	6	17	0	29	0	0	40	9
71	H	2	3	0	35	0	0	38	21
72	R	1	0	0	27	1	0	19	52
73	R	0	0	0	11	0	0	0	89
74	K	0	0	0	0	0	0	0	100

Table A5. Distances indicating the presence of cation-π interactions in the final ensemble

	Residue 1		Residue 2		distances [A] (PHE|TYR/TRP atom to ARG/LYS atom)				
MODEL	Type	position	type	position	Ring plane to CZ/NZ	Ring plane to NE/CE	CD1 to NZ/CZ	CD2/CH2 to NZ/CZ	CZ/CE2 to NZ/CZ
1	TYR	61	ARG	57	5,03	4,68	5,45	5,17	5,98
1	TYR	61	ARG	64	3,40	3,54	6,00	4,63	4,50
5	TRP	17	LYS	21	2,85	3,19	4,92	3,56	3,84
5	PHE	42	ARG	39	3,70	3,81	4,29	3,82	4,92
6	PHE	42	ARG	41	4,16	4,59	4,63	5,12	4,32
7	PHE	42	ARG	46	3,61	3,38	3,71	4,43	4,08
8	PHE	16	ARG	13	2,06	1,34	5,94	3,74	4,91
8	PHE	42	ARG	39	2,39	2,20	3,73	5,80	4,65
9	PHE	16	ARG	13	4,30	4,41	4,56	5,11	5,60
9	PHE	16	LYS	5	2,59	3,34	5,24	4,24	3,50
10	PHE	42	ARG	46	4,10	4,39	4,85	5,91	4,79
10	TYR	61	ARG	64	3,61	3,76	4,22	5,86	5,53
11	PHE	16	ARG	13	4,33	5,25	4,93	4,41	4,66
11	PHE	42	ARG	46	4,02	4,07	4,76	4,07	4,29
11	TYR	61	ARG	64	4,33	5,28	4,63	4,55	4,43
12	TRP	17	LYS	21	3,65	3,68	5,26	3,73	3,97
12	TYR	61	ARG	64	3,49	4,06	4,17	3,58	3,82
13	PHE	42	ARG	46	5,08	4,99	5,15	5,49	5,26
14	TYR	61	ARG	62	2,85	3,07	3,93	5,23	3,76
15	PHE	42	ARG	46	0,31	0,91	5,89	3,47	5,00
17	PHE	16	ARG	13	3,38	3,57	4,28	3,59	3,70
22	PHE	16	ARG	13	3,87	3,83	4,41	3,91	4,79
23	TRP	17	LYS	21	3,52	3,40	4,48	4,05	3,81
23	PHE	42	ARG	41	3,83	4,47	5,16	5,32	4,08
25	PHE	42	ARG	41	3,50	4,18	4,07	4,64	3,62
26	TYR	61	ARG	64	3,79	4,22	3,81	4,44	4,62
27	TYR	61	ARG	64	3,10	3,39	4,63	3,92	3,29
28	TRP	17	LYS	21	3,11	3,13	5,59	5,97	4,92
29	TRP	17	ARG	13	4,20	4,17	5,68	4,19	4,53
30	PHE	42	ARG	39	2,75	2,69	5,30	3,56	4,25
32	TYR	61	ARG	60	3,14	4,16	5,02	5,69	3,89
33	TRP	17	LYS	21	3,51	3,35	5,89	5,96	5,16
35	PHE	42	ARG	46	3,97	4,51	4,21	4,35	5,01
36	PHE	16	ARG	13	3,28	3,46	3,50	3,48	3,73
37	PHE	42	ARG	41	4,16	5,24	4,47	4,34	4,38
37	PHE	42	ARG	46	3,65	2,86	3,76	4,68	4,99
39	PHE	42	ARG	41	3,81	4,81	4,57	5,80	4,61
40	PHE	42	ARG	39	4,29	4,68	4,79	4,29	5,08
41	PHE	16	ARG	13	2,77	2,99	3,22	4,82	4,24
43	TYR	61	ARG	64	4,42	5,47	4,84	5,86	5,07
45	TRP	17	ARG	13	3,52	3,77	4,01	4,81	3,97
46	PHE	42	ARG	46	4,10	4,51	4,12	4,62	4,43
47	TRP	17	ARG	13	3,63	3,38	4,04	4,67	3,73
47	PHE	42	ARG	46	3,93	3,08	4,35	5,33	4,39
50	PHE	16	LYS	9	3,63	4,83	5,16	4,06	4,30
54	TRP	17	ARG	10	3,22	3,29	4,44	3,54	3,38
54	TYR	61	ARG	57	4,09	5,06	4,36	4,19	4,69
55	TYR	61	ARG	57	3,47	4,29	4,15	3,71	4,83
56	PHE	42	ARG	46	2,53	3,15	4,89	5,33	3,36
58	PHE	42	ARG	39	3,81	4,40	4,10	4,81	5,39
59	TYR	61	ARG	64	3,11	3,49	3,82	4,34	3,24
60	TYR	61	ARG	64	3,85	3,88	4,73	5,00	3,94

Table A6:.Sequences producing significant alignments for NCBI BLASTP on the Drebrin SAH sequence

Protein	Isoform	Scientific name	Taxid	Identical percentage
drebrin	1	*Myotis myotis*	51298	100.00
drebrin	1	*Rhinolophus ferrumequinum*	59479	100.00
drebrin	isoform X7	*Pan troglodytes*	9598	100.00
drebrin	isoform X1	*Odocoileus virginianus texanus*	9880	100.00
drebrin	isoform X6	*Halichoerus grypus*	9711	100.00
drebrin	isoform X4	*Phoca vitulina*	9720	100.00
drebrin	isoform X7	*Phyllostomus discolor*	89673	100.00
drebrin	isoform X8	*Phyllostomus discolor*	89673	100.00
drebrin	isoform X7	*Artibeus jamaicensis*	9417	100.00
drebrin	isoform X2	*Elephas maximus indicus*	99487	100.00
drebrin	1	*Rousettus aegyptiacus*	9407	100.00
drebrin	isoform X3	*Phyllostomus hastatus*	9423	100.00
drebrin	isoform X4	*Oryctolagus cuniculus*	9986	100.00
drebrin	isoform X3	*Oryctolagus cuniculus*	9986	100.00
drebrin	isoform X4	*Sus scrofa*	9823	100.00
drebrin	isoform X3	*Delphinus delphis*	9728	100.00
drebrin		*Pontoporia blainvillei*	48723	100.00
drebrin	isoform X4	*Sturnira hondurensis*	192404	100.00
drebrin	isoform X3	*Canis lupus familiaris*	9615	100.00
unnamed	protein product	*Gulo gulo*	48420	100.00
drebrin	isoform X6	*Saccopteryx bilineata*	59482	100.00
drebrin	isoform X3	*Chlorocebus sabaeus*	60711	100.00
drebrin	isoform X6	*Saccopteryx leptura*	249018	100.00
drebrin	isoform X4	*Trachypithecus francoisi*	54180	100.00
drebrin	isoform X3	*Macaca mulatta*	9544	100.00
drebrin	isoform X3	*Macaca fascicularis*	9541	100.00
drebrin	isoform X3	*Diceros bicornis minor*	77932	100.00
drebrin	isoform X3	*Macaca nemestrina*	9545	100.00
drebrin	1	*Rhinolophus ferrumequinum*	59479	100.00
drebrin	isoform X6	*Oryctolagus cuniculus*	9986	100.00
drebrin		*Neophocaena asiaeorientalis asiaeorientalis*	1706337	100.00
drebrin	isoform X9	*Phyllostomus discolor*	89673	100.00
drebrin	isoform X3	*Pan paniscus*	9597	100.00
drebrin	isoform X3	*Papio anubis*	9555	100.00
drebrin	isoform X3	*Nomascus leucogenys*	61853	100.00
drebrin	isoform X1	*Pan troglodytes*	9598	100.00
drebrin	isoform X3	*Ochotona princeps*	9978	100.00
drebrin	isoform X3	*Hylobates moloch*	81572	100.00
drebrin	isoform X4	*Pan paniscus*	9597	100.00
drebrin	isoform g	*Homo sapiens*	9606	100.00
drebrin	isoform X3	*Kogia breviceps*	27615	100.00
drebrin	isoform X5	*Saimiri boliviensis boliviensis*	39432	100.00
drebrin	isoform X2	*Odocoileus virginianus texanus*	9880	100.00
drebrin	isoform X4	*Nyctereutes procyonoides*	34880	100.00
drebrin	isoform X5	*Pan troglodytes*	9598	100.00
drebrin	isoform X3	*Lagenorhynchus obliquidens*	90247	100.00
Drebrin		*Camelus dromedarius*	9838	100.00
drebrin	isoform X3	*Sapajus apella*	9515	100.00
drebrin		*Felis catus*	9685	100.00
drebrin	isoform X2	*Homo sapiens*	9606	100.00
drebrin	1, isoform CRA_d	*Homo sapiens*	9606	100.00
DBN1		*Cervus elaphus hippelaphus*	46360	100.00
drebrin	isoform X4	*Pongo abelii*	9601	100.00
Drebrin		*Myotis davidii*	225400	100.00
drebrin	isoform X2	*Phocoena sinus*	42100	100.00
drebrin	isoform X2	*Cebus imitator*	2715852	100.00
drebrin	isoform X2	*Diceros bicornis minor*	77932	100.00
drebrin	isoform X2	*Homo sapiens*	9606	100.00
Drebrin		*Eschrichtius robustus*	9764	100.00
drebrin	isoform X4	*Tursiops truncatus*	9739	100.00
drebrin	isoform X5	*Tursiops truncatus*	9739	100.00
drebrin	isoform X3	*Gorilla gorilla gorilla*	9595	100.00
drebrin	isoform X3	*Piliocolobus tephrosceles*	591936	100.00
drebrin		*Vulpes vulpes*	9627	100.00
drebrin	isoform X3	*Rhinopithecus roxellana*	61622	100.00
drebrin	isoform X6	*Pan troglodytes*	9598	100.00
drebrin	isoform X5	*Pongo abelii*	9601	100.00
drebrin	isoform X2	*Rhinopithecus roxellana*	61622	100.00
drebrin	isoform X3	*Ochotona curzoniae*	130825	100.00
drebrin		*Myotis lucifugus*	59463	100.00
drebrin	1, isoform CRA_b	*Homo sapiens*	9606	100.00
drebrin	isoform X2	*Pongo abelii*	9601	100.00
drebrin	isoform X5	*Lagenorhynchus obliquidens*	90247	100.00
drebrin	isoform X5	*Phoca vitulina*	9720	100.00
drebrin	isoform X2	*Trichechus manatus latirostris*	127582	100.00
drebrin	isoform X4	*Macaca fascicularis*	9541	100.00
drebrin	isoform X2	*Piliocolobus tephrosceles*	591936	100.00
drebrin	isoform X8	*Artibeus jamaicensis*	9417	100.00
drebrin	isoform X1	*Ochotona princeps*	9978	100.00
drebrin	isoform X2	*Panthera tigris*	9694	100.00
drebrin	isoform X2	*Panthera leo*	9689	100.00
drebrin	isoform X5	*Gorilla gorilla gorilla*	9595	100.00
drebrin	isoform X5	*Halichoerus grypus*	9711	100.00
drebrin	isoform X3	*Phoca vitulina*	9720	100.00
drebrin	isoform X2	*Ochotona princeps*	9978	100.00
drebrin		*Erinaceus europaeus*	9365	100.00